UNIVERSIDADE DE SÃO PAULO
Escola de Engenharia de São Carlos

A NEURAL NETWORK-AIDED MICROWAVE SENSING APPROACH FOR QUALITATIVE AND QUANTITATIVE ANALYSIS OF ADULTERATION IN EXTRA VIRGIN OLIVE OIL

JÚLIO CESAR PICOLO ALARCON

EESC · USP

JÚLIO CESAR PICOLO ALARCON

A neural network-aided microwave sensing approach for qualitative and quantitative analysis of adulteration in extra virgin olive oil

Dissertation presented to the São Carlos School of Engineering of the University of São Paulo in fulfillment of the requirements for the degree of Master of Science in Electrical Engineering.

Subject area: Telecommunications

Advisor: Prof. Dr. Ben-Hur Viana Borges

Trata-se da versão corrigida da dissertação. A versão original se encontra disponível na EESC/USP que aloja o Programa de Pós-Graduação de Engenharia Elétrica.

São Carlos

2024

Ficha catalográfica elaborada pela Biblioteca Prof. Dr. Sérgio Rodrigues Fontes da EESC/USP com os dados inseridos pelo(a) autor(a).

Alarcon, Júlio Cesar Picolo
A321a A neural network-aided microwave sensing approach for qualitative and quantitative analysis of adulteration in extra virgin olive oil / Júlio Cesar Picolo Alarcon; orientador Ben-Hur Viana Borges; coorientador Vinicius Marrara Pepino. São Carlos, 2024.

Dissertação (Mestrado) - Programa de Pós-Graduação em Engenharia Elétrica e Área de Concentração em Telecomunicações -- Escola de Engenharia de São Carlos da Universidade de São Paulo, 2024.

1. Adulteration. 2. artificial neural network. 3. authenticity. 4. dielectric spectroscopy. 5. extra virgin olive oil. 6. fraud. 7. microwave sensor. 8. resonator. I. Título.

Eduardo Graziosi Silva - CRB - 8/8907

FOLHA DE JULGAMENTO

Candidato: Engenheiro **JÚLIO CESAR PICOLO ALARCON**.

Título da dissertação: "Uma abordagem de sensoriamento em microondas auxiliada por redes neurais para análise qualitativa e quantitativa de adulteração em azeite de oliva extra virgem".

Data da defesa: 12/07/2024.

Comissão Julgadora	**Resultado**
Prof. Associado Emiliano Rezende Martins (Presidente da Banca) (Escola de Engenharia de São Carlos/EESC-USP)	APROVADO
Prof. Associado Daniel Varela Magalhães (Instituto de Física de São Carlos/IFSC-USP)	APROVADO
Prof. Dr. Achiles Fontana da Mota (Universidade de Brasília - UnB)	APROVADO

Coordenador do Programa de Pós-Graduação em Engenharia Elétrica:
Prof Associado **Marcelo Andrade da Costa Vieira**

Presidente da Comissão de Pós-Graduação:
Prof. Titular **Carlos De Marqui Junior**

I dedicate this work to everyone who has supported me throughout this journey. To my family and friends, whose encouragement and belief in me have been a constant source of strength and motivation. To my advisor and colleagues, whose guidance and insights have enriched this research. And to all the researchers and scientists, past and present, whose relentless pursuit of knowledge continues to inspire. This work is for you all.

ACKNOWLEDGMENTS

To begin with, I would like to thank God for my life, health, family, friends and opportunities I have along this journey.

I would like to extend my deepest gratitude to my advisor, Professor Ben-Hur Viana Borges, and my co-advisor, Vinicius Marrara Pepino, for their unwavering support, guidance, and encouragement throughout this research. Their expertise, insightful feedback, and constant motivation have been invaluable to the completion of this research and dissertation. I am truly grateful for the opportunity to learn from and work with such exceptional people.

Thanks to my mother, Florinda A. P. Alarcon, who always gave me support and encouraged me during every step of my life, since my very first second of life. Thanks to my girlfriend, Maria C. R. de Souza, who shared and shares many special moments with me, always making me feel right and comfortable about my decisions. Thanks to my entire family, the basis of my education and source of emotional support. Thanks to my childhood friends, with whom I shared many wonderful and fruitful memories: Arthur, Erick, João, Luciano and Renan

Next, I would like to express my gratitude for having the opportunity to work with my amazing lab colleagues and friends: Gabriel, Patrick, Isabel, Mateus, Guilherme, Vinicius, Ali, and João. Their friendship and partnership encouraged and motivated me during this journey.

Finally, I would like to thank the funding agencies that made this research possible: Coordination for the Improvement of Higher Education Personnel (CAPES, finance code 001), the National Council of Scientific and Technological Development (CNPq) under Grant 304208/2021-3, and the São Paulo Research Foundation (FAPESP) under Grant 2013/07276-1.

ABSTRACT

ALARCON, J. C. P. **A neural network-aided microwave sensing approach for qualitative and quantitative analysis of adulteration in extra virgin olive oil**. 2024. Dissertation (Master in Science) - São Carlos School of Engineering, University of São Paulo, São Carlos, 2024.

In this work, we develop a spoof localized surface plasmon resonator-based planar microwave sensor that, together with simple architectures of feedforward artificial neural networks (ANNs), is capable of detecting and quantizing adulterants in extra virgin olive oil (EVOO). We investigate four common adulterants of EVOO, namely soybean oil, corn oil, sunflower oil, and canola oil. The sensor incorporates a four-spiral resonator electromagnetically coupled to microstrip transmission lines operating at 546.8 MHz to detect changes in the complex permittivity of EVOO samples, caused by adulteration. A vector network analyzer (VNA) is used to measure the sensor's complex scattering parameters S_{11} and S_{21}, that serves as inputs for two different multilayer Perceptron (MLP) ANNs. The first model, using only the real and imaginary components of S_{21} achieves an overall accuracy of 91.4% in detecting which adulterant oil is being applied to the EVOO test samples. In contrast, the second model, incorporating the real and imaginary components of both S_{11} and S_{21}, attains an overall accuracy of 99.2% in predicting the adulterant used in the test samples. Additionally, we leverage the linear behavior found between the measured $|S_{21}|$ (in dB) and the adulteration levels, expressed as the percentile value of the volume of adulterant per volume of the sample (mL/mL), to develop first order polynomials using partial least squares regression (PLSR) to predict adulteration levels up to 50%. The maximum obtained root mean square error (RMSE) is 2.1% for canola oil adulteration prediction. PLSR yields RMSE values of 0.9% for soybean oil, 1.1% for corn oil, and 1.0% for sunflower oil adulteration. Additionally, in contrast to recent works involving EVOO adulteration that utilize multiple spectral components of EVOO's spectra at optical frequencies, we experimentally demonstrate that a single frequency component of the proposed microwave sensor's reflected and transmitted signals can provide us enough information to identify and quantify adulterated EVOO samples. This methodology offers both qualitative and quantitative analyses of EVOO, allowing the detection of adulterations as low as 5% with a simple, portable, and practical system.

Keywords: Adulteration, artificial neural network, authenticity, dielectric spectroscopy, extra virgin olive oil, fraud, machine learning, microwave sensor, resonator.

RESUMO

ALARCON, J. C. P. **Uma abordagem de sensoriamento em microondas auxiliada por redes neurais para análise qualitativa e quantitativa de adulteração em azeite de oliva extra virgem**. 2024. Dissertação (Mestrado) – Escola de Engenharia de São Carlos, Universidade de São Paulo, São Carlos, 2024.

Neste trabalho, nós desenvolvemos um sensor planar em microondas baseado no fenômeno de ressonância *spoof localized surface plasmons* que, em conjunto com arquiteturas *feedforward* simples de redes neurais artificiais (RNAs), é capaz de detectar e quantizar adulterantes em azeite de oliva extra virgem (AOEV). Nós investigamos quadro adulterantes comuns de AOEV, nomeadamente óleo de soja, óleo de milho, óleo de girassol e óleo de canola. O sensor incorpora um ressoador de quatro espirais acoplado eletromagneticamente à linhas de transmissão de microfita operando em 546.8 MHz para detectar mudanças na permissividade complexa de amostras de AOEV, causadas por adulteração. Um analisador de redes vetoriais (ARV) é usado para medir os parâmetros complexos de espalhamento S_{11} e S_{21} do sensor, que servem como entradas para duas diferentes RNAs Perceptron multicamadas (PMC). O primeiro modelo, usando apenas as componentes reais e imaginárias do S_{21} obtém uma precisão geral de 91.4% em detectar qual óleo adulterante está sendo aplicado às amostras de AOEV. Em contraste, o segundo modelo, incorporando as componentes reais e imaginárias do S_{11} e S_{21}, obtém uma precisão geral de 99.2% em prever o adulterante usado nas amostras de teste. Além disso, nós aproveitamos o comportamento linear observado entre o $|S_{21}|$ medido (em dB) e os níveis de adulteração, expressados como o valor percentual de volume de adulterante por volume de amostra, para desenvolver polinômios de primeira ordem utilizando a regressão por mínimos quadrados parciais (PLSR) para prever os níveis de adulteração em até 50%. A raiz do erro médio quadrático máxima (RMSE) obtida é 2,1% para previsões com óleo de canola como adulterante. O método PLSR resulta em valores de RMSE de 0,9% para óleo de soja; 1,1% para óleo de milho e 1,0% para óleo de girassol. Ademais, em contraste com os trabalhos recentes envolvendo adulteração de AOEV que utilizam múltiplos componentes espectrais do espectro de AOEV em frequências ópticas, nós demonstramos experimentalmente que uma única componente de frequência dos sinais refletidos e transmitidos do sensor proposto em microondas nos fornece informação suficiente para identificar e quantificar amostras

adulteradas de AOEV. Esta metodologia oferece tanto uma análise qualitativa quanto quantitativa de AOEV, permitindo a detecção de adulterações tão baixas quanto 5% com um sistema simples, portátil e prático.

Palavras-chave: Adulteração, redes neurais artificiais, autenticidade, espectroscopia dielétrica, azeite de oliva extra virgem, fraude, aprendizagem de máquinas, sensor em microondas, ressoador.

LIST OF FIGURES

LIST OF TABLES

LIST OF ABBREVIATIONS

FAO	Food and Agriculture Organization
EVOO	Extra Virgin Olive Oil
IOC	International Olive Council
NMR	Nuclear Magnetic Resonance
HPLC	High-performance Liquid Chromatography
UHPLC	Ultra-high-performance Liquid Chromatography
PCA	Principal Component Analysis
PC	Principal Component
MRI	Magnetic Resonance Imaging
PLS-DA	Partial Least Squares Discriminant Analysis
PLS	Partial List Squares
SVM	Support Vector Machine
NIR	Near Infrared
SIMCA	Soft Independent Modelling Class Analogy
LOD	Limit Of Detection
CSRR	Complementary Split Ring Resonator
ANN	Artificial Neural Network
KNN	K-Nearest Neighbor
SVM	Support Vector Machine
SRR	Split-ring Resonator
MUT	Material Under Test
PCB	Printed Circuit Board
LOD	Limit of Detection
LSP	Localized Surface Plasmon
PEC	Perfect Electric Conductor
CPW	Coplanar Waveguide
VNA	Vector Network Analyzer
ANN	Artificial Neural Network
MLP	Multilayer Perceptron

DNN	Deep Neural Network
ReLU	Rectified linear Unit
PLSR	Partial Least Squares Regression
RMSE	Root Mean Squared Error
MSE	Mean Squared Error

LIST OF SYMBOLS

S_n	Nuclear spin
l_n	Nuclear spin quantum number
μ_n	Nuclear magnetic moment
γ_n	Gyromagnetic ratio
T_1	Spin-lattice relation time
T_2	Spin-spin relation time
E	Electric field vector
H	Magnetic field vector
D	Electric flux density vector
B	Magnetic flux density vector
J	Current density vector
ε	Electric permittivity
ε_0	Electric permittivity of the free space
ε_r	Relative permittivity
ε'	Real component of the complex permittivity
ε''	Imaginary component of the complex permittivity
ε_{eff}	Effective electric permittivity
ε_∞	Electric permittivity at very high frequencies
ε_s	Static electric permittivity
τ	Relaxation time
$\tan\delta$	Dielectric loss tangent
μ	Magnetic permeability
μ_0	Magnetic permeability of the free space
μ'	Real component of the magnetic permeability
μ''	Imaginary component of the magnetic permeability
σ	Electric conductivity
$\mathbf{P_e}$	Electric polarization vector
x_e	Electric susceptibility
x_m	Magnetic susceptibility
λ	Wavelength
S_{11}	Reflection coefficient
S_{21}	Transmission coefficient
ω	Angular frequency

C	Capacitance
L	Inductance
C_{pul}	Capacitance per unit length
λ	Wavelength
β	Phase constant
Z	Characteristic impedance
I	Current intensity
f_r	Resonance frequency
$\Delta f_{3\mathrm{dB}}$	Half-power bandwidth
Q	Quality factor
S	Sensitivity
U	Energy
P_{loss}	Dissipated power
u	Net input of a system
y	Output of a system
w	Weight of a connection between two neurons
w_0	Bias of a neuron
x	Numerical value of a sample's feature
$\mathbf{x}$	Numerical values of a sample or multiple samples' features
$\mathbf{w}$	Weight of the connections between two or more neurons
$\mathbf{u}$	Output vector of a system
$\mathbf{y}$	Input vector of a system
η	Learning rate
$E(k)$	Prediction error of a sample
d	Ground truth label of a sample
E_m	Mean squared error
$\delta_i(L)$	Local gradient of the *i*-th neuron of layer *L*

TABLE OF CONTENTS

1. INTRODUCTION

1.1 POPULATION GROWTH AND THE ROLE OF THE FOOD MARKET

In recent decades, global population growth has emerged as a significant concern, with projections indicating shortage of drinkable water and food, wars, diseases and poverty. The world's population reached 1 billion in 1800 with the second billion being reached 130 years later, in 1930. The third billion was reached in 1960, the fourth billion in 1974, the fifth billion in 1987, the sixth billion in 1999, the seventh billion in 2011 [1] and, finally, the eight billion in November 2022 [2].

Mankind growing trend is expected to continue throughout the century, with an uncertainty about future trends that gets wider over time [3], however the global human population is projected to reach 10 billion by 2060 [2]. Population growth along with urbanization, economic challenges, volatile markets, lack of agricultural resources and climate unpredictability are the most popular causes of food insecurity around the world [4]. Food security is a concept with several definitions in literature, commonly being supported by four pillars: availability, access, utilization and stability [5]. The concept is formally defined as the consistent physical, social and economic access to sufficient and safe food that meets nutritional needs and food preferences [6].

According to the Food and Agriculture Organization (FAO), almost 3.1 billion people could not afford a healthy diet in 2020 due to increased costs, while around 2.3 billion people were classified as moderately or severely food insecure in 2021 and 923.7 million people faced severe food insecurity [7]. This data, provided by FAO, combined with the projections of population growth, paints a concerning picture of resource scarcity in the near future. It is imperative to address this issue to safeguard human life on Earth. There are international policies focusing on food security, such as the United Nation's initiative to eradicate extreme poverty and hunger. This global commitment reinforces the need to address basic physiological needs [8].

The agricultural sector plays a pivotal role in improving the availability and quality of food, contributing directly to food security. However, there is uncertainty about the agriculture's

capacity to efficiently supply the growing demand for food [9]. The sector is greatly impacted by the unpredictable nature of weather and the challenges involving agriculture were considerably increased due to COVID-19 pandemic, causing the reduction in agricultural production and increase in products costs [10].

In a post-pandemic scenario, smart farming offers a promising opportunity of revitalizing and enhancing the agricultural sector. Technologies such as robotics, unmanned aerial vehicles, machine learning and artificial intelligence are emerging as the foundation of the third green revolution, with the capabilities to increase both crop yield and quality [11]. Recent research has primarily focused on predicting soil parameters such as organic carbon and moisture content, crop yield, disease identification, and species detection [12], particularly focusing on properties associated with the pre-harvest stage. While monitoring the health status of soil and plants is crucial for enhancing production, ensuring the quality of agricultural products is equally essential for supplying the food market.

Ensuring food quality in the food market is one of the key areas of focus in public health, as it can impact people worldwide. The most common public health risks are associated with poor food quality and poor food handling, including microbial contamination of foods, chemical contamination, adulteration, misuse of additives, mislabeling, genetically modified foods and outdated foods [13]. In particular, adulteration stands out as a significant concern within the realm of food safety. Adulteration involves the intentional addition of inferior or harmful substances to food products, primarily motivated by economic gain. This deceptive practice not only compromises the nutritional value and integrity of food, but also poses serious health risks to consumers [14]. Instances of adulteration have been reported across various food categories, ranging from spices and condiments [15], [16], [17] to dairy and meat products [18], [19], [20], [21].

1.2 EXTRA VIRGIN OLIVE OIL

Extra virgin olive oil (EVOO) is a product obtained exclusively through mechanical and physical processes, including collecting, washing and crushing of olives, followed by malaxation of olive paste, centrifugation, storage, and filtration [22]. EVOO distinguishes itself among the wide variety of food products available in the food market due to its rich nutritional

profile and unique health benefits derived from its chemical composition [23]. However, the high economic value of EVOO and the increasing demand for the product have makes it susceptible to fraudulent activities, posing potential risks to consumers [24].

The increased global demand for olive oil is reported by the International Olive Council (IOC) and depicted in **Figure 1.1** along with the global production. IOC is also responsible for classifying and defining trade standards for olive oil. According to the council, virgin olive oils deemed suitable for consumption should have a free acidity, expressed as oleic acid, of not more than 3.3 grams per 100 grams. The IOC classifies olive oils suitable for consumption based on their oleic acid content, resulting in categories such as extra virgin olive oil (up to 0.8 g/100g), virgin olive oil (up to 2 g/100g), and ordinary virgin olive oil (up to 3.3 g/100g) [25].

Figure 1.1 – Global production and consumption of olive oil from 1990 to 2020.

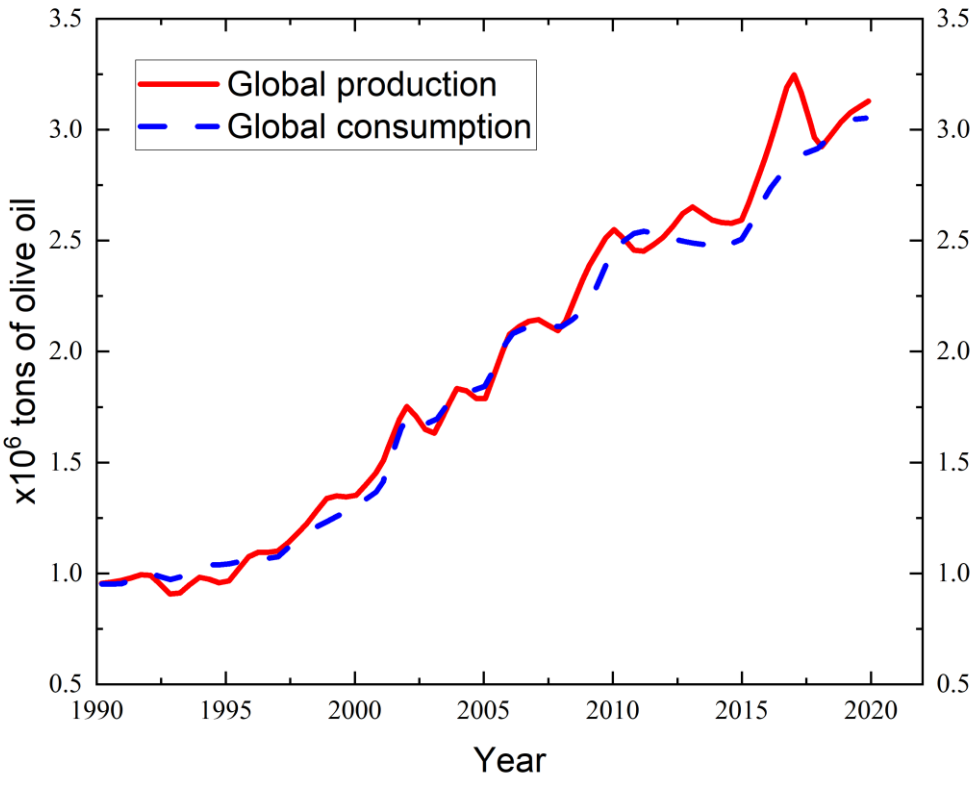

Source: IOC. Available online at https://www.internationaloliveoil.org/wp-content/uploads/2021/02/IOC-Import-profiles-table-olive-2019-20-rev0.html#import-trends-of-table-olive-in-the-world.

EVOOs are mainly composed of triacylglycerols (98%) and minor fat compounds, such as phenolic compounds, aliphatic alcohols, phytosterols and tocopherols (vitamin E). The health benefits attributed to EVOO stem from its fat composition, which includes oleic and linoleic acids, as well as bioactive compounds like β-carotenes, volatile compounds, and sterols [26]. The abundance of antioxidant and anti-inflammatory phenolic compounds in EVOO, along with its favorable fatty acid profile, contributes to numerous health benefits, including prevention of cardiovascular diseases, cancer, neurodegenerative disorders, and diabetes [24]. According to the European Regulation EU 432/2012, olive oil phenols protect blood lipids from oxidative stress. This claim is associated with a minimum intake of 5 mg of these phenols with a recommended daily consumption of 20 g of product [27]. EVOO has also been shown to have anti-atherosclerotic properties and beneficial effects on endothelial function and blood pressure control. Additionally, the reduced risk of cancer and cardiovascular diseases has been specifically associated with the consumption of virgin olive oils rather than ordinary olive oils [28].

Despite stringent regulatory measures governing EVOO quality, susceptibility to fraudulent activities still persists within the food industry, primarily motivated by economic incentives. Given the high economic value, limited production, and significant demand for EVOO, fraudsters frequently adulterate the product with lower quality olive oils or vegetable oils, which do not offer the same benefits associated with virgin olive oils. Common adulterants of EVOO include olive pomace oil, sunflower oil, rapeseed oil, hazelnut oil, corn oil, walnut oil, soybean oil and canola oil [29].

1.3 DETECTING ADULTERATION IN EXTRA VIRGIN OLIVE OIL

In light of the increasing problem of adulteration affecting the production and commercialization of EVOO, the field of food science has witnessed remarkable strides in laboratory analysis and techniques. These advancements serve as a robust response aimed at safeguarding the quality, purity, and authenticity of EVOO in the food market. With increasing concerns about fraudulent practices undermining consumer trust and jeopardizing public health, researchers and industry experts have dedicated significant resources to developing and refining sophisticated analytical methods. These cutting-edge techniques encompass a wide array of

approaches, including chromatography, nuclear magnetic resonance (NMR) and spectroscopy [30]. Moreover, advancements in data analytics and machine learning have further enhanced the accuracy and efficiency of these analyses, enabling rapid and reliable identification of fraudulent EVOO products. Machine learning tools are capable of extracting complex features from the measured data and handling multiple pieces of information; therefore, they have been widely explored in the food market [31]. As a result, consumers can have greater confidence in the authenticity and quality of the products they purchase, while producers and regulatory authorities are equipped with the technology to effectively combat fraudulent activities and uphold industry standards.

In this section, we explore the various methods used to detect adulterations in EVOO, ranging from traditional industry standards to innovative approaches. We'll begin by examining the established industry methods, such as chromatography and spectroscopy, designed to assess the purity and authenticity of EVOO. Then, we'll shift our focus to emerging technologies including machine learning and data fusion, which offer promising ways to detect subtle adulterations.

1.3.1 Chromatographic approach

Chromatography is a qualitative and quantitative technique widely used in laboratories to separate different components in a mixture. [32]. The chromatographic methods available to detect adulterations in EVOO are based on the quantification of specific marker compounds. The marker compounds such as triglycerides, tocopherols, tocotrienols, phenolic compounds and pyropheophytins are determined with high-performance liquid chromatography (HPLC). While marker compounds such as fatty acid methyl esters, campesterol, stigmasterol, triacylglycerol, stigmastadiene and volatile compounds are determined with gas chromatography [29].

The quality assessment of olive oil is governed by the IOC together with the European Community and the Codex Alimentarius Commission [24]. The IOC has released detailed industry standards for determining marker compounds in EVOO, providing chemical analyses of EVOO samples. To establish a quality parameter for EVOOs, the IOC has proposed a method for determining the content of waxes and fatty acid ethyl esters using capillary gas

chromatography [33]. This method involves adding suitable internal standards to the oil and fractionating by chromatography on a hydrated silica gel column, followed by the recovery of the fraction eluted and direct analysis by capillary gas chromatography.

Quantification of biophenolic minor polar compounds in olive oils are carried out with the aid of HPLC. The method described in [34] is based on the direct extraction of phenolic compounds from olive oil by means of a methanol solution and subsequent quantification by HPLC with the aid of a UV detector at 280 nm. Other pure HPLC chromatography grade reagents such as orthophosphoric acid, acetonitrile, water, tyrosol and syringic acid are needed.

The adulteration of EVOO with soft-deodorized virgin olive oil has been studied in [35]. The authors analyzed chemical changes in virgin olive oils after soft-deodorization, targeting specifically the concentration of volatiles, fatty acid ethyl esters and pyropheophytins. To accomplish this, HPLC and gas chromatography were used. Samples with sensory defects such as vinegary, muddy sediment, fusty, and intense rancid, went through a deodorization process carried out by a deodorization system. The deodorization process involved agitating the oil sample while keeping it at high temperature (130 ºC maximum), under vacuum, for a fixed time (60 min maximum). These conditions allowed removing volatiles responsible for sensory defects, with low losses of total phenols, pyropheophytins and fatty acid ethyl esters. The authors claim that soft-deodorized virgin olive oils could be added to EVOOs in proportions of up to 50% without being detected by the current standard methods.

Applying chromatographic techniques to analyze olive oil samples, in particular its fatty acid and sterol profiling, is very time consuming and tedious, often requiring specialized personnel, sample preparation and the manipulation of dangerous chemical reagents [24], [29], [36]. In [37], an approach combining ultra-high-performance liquid chromatography (UHPLC) and principal component analysis (PCA) statistical method is proposed to identify adulterant oils in EVOO based on their triacylglycerol profiles. The authors claim that the proposed method, when compared to traditional methods, involves minimal sample preparation, offering a fast analysis and not requiring specialized trained chemists. However, HPLC grade solvents such as acetonitrile, chloroform, hexane, isopropanol, methanol and toluene, are still needed, which does not totally remove the complexity of the method.

Given the complexity and high costs associated with chromatographic methods used to verify the authenticity of EVOOs, researchers have increasingly turned their attention towards exploring alternative approaches. These alternative methods are sought to identify adulterations

with lower quality oils in EVOOs quickly and accurately, all while being more cost-effective. The overarching aim is to develop methods that don't require expensive equipment or specialized technicians to operate them, thus democratizing adulteration detection in the EVOO industry. Unlike chromatography, which involves extensive sample preparation and can only be performed in a laboratory setting, these new methods are designed to be portable and adaptable for use in various environments. This means that samples don't need to be transported to a centralized laboratory, which not only saves time and resources but also makes the process more accessible to a wider range of stakeholders across the supply chain. In summary, the ongoing efforts to explore alternative methods for adulteration detection in EVOOs represent a significant step towards ensuring higher quality standards and greater transparency in the industry.

1.3.2 Nuclear magnetic resonance approach

Nuclear magnetic resonance spectroscopy is an analytical technique that exploits the magnetic properties of atomic nuclei with either an odd mass number or an even mass number combined with an odd atomic number. These nuclei possess a type of angular momentum known as nuclear spin S_n and are characterized by a nuclear spin quantum number l_n. For nuclei with an odd mass number, $l_n = \frac{1}{2}$, while for nuclei with an even mass number and an odd atomic number, $l_n = 1$. All nuclei with $l_n \neq 0$ exhibit a small magnetic field and have a nuclear magnetic moment μ_n. Another intrinsic property of nuclei, known as gyromagnetic ratio γ_n, determines the magnetic strength and its relationship with the nuclear spin through $\mu_n = \gamma_n S_n$. The presence of a nuclear magnetic moment allows nuclei to interact with an external magnetic field generated by the NMR instrument [38].

Protons relaxation times, namely spin-lattice relation time (T_1) and spin-spin relation time (T_2), in a food system can be studied specifically through the measurement of radio frequency absorption resonance by non-zero nuclear spins from protons exposed to an external static magnetic field. On the other hand, magnetic resonance imaging (MRI) is a non-ionizing and non-invasive technology that involves atomic particles interacting with an external magnetic field to emit energy at a particular frequency [39]. With continuous improvement and innovation of NMR technology, analysis expanded from the initial one-dimensional nature to

two-dimensional and multi-dimensional natures of data. In a short time period, the application scope of NMR was gradually expanded from physics and chemistry to biology, medicine, food industry, petroleum industry and other fields [40]. In the food industry, for example, NMR spectroscopy was used to characterize food allergens [41], ensure the quality and authenticity of milk and dairy products [42], detect addition of admixtures of peanut powder in various food products [43], detect Salmonella in milk samples [44], ensure quality and authenticity of coffee [45], and much more.

In [46], low-field NMR (0.53 T) is employed to identify adulterations in olive oil with soybean oil and corn oil. Different adulteration levels are studied, and gas chromatography is performed to analyze the fatty acid composition of oil samples and compare it to the data obtained from low-field NMR. The authors make use of pattern recognition models such as PCA and partial least squares discriminant analysis (PLS-DA) to treat the data obtained from NMR and are capable of identifying an adulteration in olive oil of at least 20% for both soybean and corn oils. The study demonstrates how promising low-field NMR technology can be to identify EVOO adulteration.

In [47], low-resolution NMR systems working at 2 and 100 MHz are used to analyze EVOOs produced in different locations and other vegetable oils produced from macadamia nuts, linseeds, sunflower seeds and soybeans. Analyzing the proton NMR relaxation times T_1 and T_2, the authors show that the relaxation behavior of macadamia oil is very similar to that of EVOOs, while the relaxation behavior of linseed oil differs the most. Moreover, the authors show a linear relationship between NMR relaxation times T_1 and T_2 at 2 MHz and the concentration of linseed oil in a reference EVOO. Additional proton NMR diffusion analysis is performed on EVOO samples adulterated with different concentrations of linseed oil. However, the relationship between the measured diffusion coefficient and the adulteration level is not linear and has poor resolution for lower concentrations. Results indicate that relaxation times T_1 and T_2, mainly T_1, are suitable for detecting a potential adulteration with linseed oil.

A different approach is presented in [48], where the authors make use of low-field NMR (0.467 T) to measure the relaxation time T_2 of different brands of EVOO samples and blends of olive oil with corn, soybean and sunflower oil. Furthermore, the machine learning technique known as Support Vector Machine (SVM) is employed to distinguish pure EVOO samples from blended ones. The SVM model acquired a classification accuracy of 84.92% when classifying adulteration levels above 10%. The study suggests again the potential of NMR technology in

ensuring the quality of EVOO products, introducing a new approach to detect adulteration based on a machine learning technique.

The chromatographic method, used to detect adulteration in EVOO, is known for its drawbacks: it is destructive, time-consuming, and involves intensive sample preparation and the handling of toxic chemicals. In contrast, the nuclear magnetic resonance (NMR) approach offers a non-destructive alternative that provides comprehensive information about the chemical composition of samples without the limitations of chromatography. This technique has proven effective in acquiring detailed insights into the composition of EVOO samples under investigation, offering a safer and more efficient alternative to chromatography [29].

1.3.3 Vibrational spectroscopy approach

Vibrational spectroscopy techniques involve taking advantage of the interaction between oscillating charged particles in a molecule and electromagnetic energy. If the frequency of the electromagnetic field is close to the frequency of the vibrational or electronic oscillations, a resonance condition is established, and the molecule exhibits a high transition probability between two vibrational states. The vibrational states and vibrational energy of a molecule is highly dependent on the chemical bonds between the atoms of the molecule, which makes vibrational spectroscopy a suitable technique for chemical characterizations. The most common techniques in the vibrational spectroscopy field are infrared (near, mid or far) and Raman spectroscopy. Infrared spectroscopy is based on the interaction between infrared radiation and a sample, causing bond vibrations and absorption of infrared radiation. Raman spectroscopy, on the other hand, deals with the inelastic scattering of light by a sample [29], [49], [50]. Due to its low running costs, high speed of analysis and non-destructive nature, vibrational spectroscopy has a wide range of applications, including clinical analysis [51], soil and water analysis [52], [53] and food analysis for adulteration detection [54].

Spectroscopy is a widely explored technique in the food market and is constantly studied for ensuring food authenticity, especially in EVOOs. In [55], a study using Raman spectroscopy is conducted using 15 varieties of edible oils, EVOO included. In total, 286 Raman spectra are measured, filtered and corrected. The authors utilize PCA to analyze the Raman spectra and reduce the high dimensional nature of the data. Subsequently, a Genetic Algorithm is used for

identifying the wavelengths that optimize the separation of the edible oils and reduce the data dimension for 2 principal frequency components of the Raman Spectra. With only 2 frequency points, the authors could separate all 15 varieties of edible oils into 5 groups with similar properties. In the group of EVOO, also were included oils with similar spectra, such as extra light olive oil, pure olive oil, avocado oil, peanut oil, safflower oil and hazelnut oil. Moreover, the study concludes that oils within the same group share a similar fatty acid profile. Other studies [56], [57], [58] also suggest the potential use of Raman spectroscopy for quality control of EVOO.

The use of spectroscopy is a suitable alternative to the chromatography method because it provides a non-invasive approach with minimal sample preparation, which can be performed *in-situ*, with the newest portable spectrometers. In [59], a portable near-infrared (NIR) spectrometer is used to analyze binary blends of EVOO with soybean, sunflower, corn and canola oil, through both transmittance and reflectance spectra. The acquired spectra of samples are then preprocessed using the first derivative of Savitzky-Golay algorithm with a second order polynomial and seven-point window. Subsequently, partial least squares (PLS) models are built to quantify adulterations based on the transmittance and reflectance spectra. The PLS model based on transmittance presents more accurate results, being capable of identifying adulterations as low as 1.8% (w/w). Additionally, the authors use PCA and soft independent modelling class analogy (SIMCA) to distinguish olive oil samples from the binary blends. The study obtains excellent results in identifying four of the most common adulterants of EVOO.

The relative simplicity of the spectroscopic method makes it an attractive alternative to chromatography and NMR for detecting EVOO adulteration. The wide range of the infrared electromagnetic spectrum offers valuable insights into the composition of a sample, making it a popular choice in studies involving vibrational spectroscopy [60], [61], [62], [63]. However, conducting *in-situ* analysis can sometimes be challenging due to potential interference from natural or artificial light sources. Moreover, high-quality spectrometers are sensitive and rather expensive devices that require careful handling and maintenance.

1.3.4 Dielectric spectroscopy approach

Dielectric spectroscopy is a non-destructive, rapid and straightforward technique that makes use of the interaction of a material with an external electric field. The behavior of a material under an electric field is dictated by its dielectric constant and dielectric loss factor. Both the dielectric constant and dielectric loss factor are dependent on the composition of the material; therefore, different materials interact differently with an external electric field [64]. The use of dielectric spectroscopy became very popular in studies involving food analysis due to its simplicity, covering a wide range of applications, including beverage analysis [65], sesame oil adulteration detection [66], [67], cow milk analysis [68] and salt analysis [69].

In the context of EVOO adulteration, dielectric spectroscopy offers the possibility of rapidly assessing the authenticity of EVOO, given that both the dielectric constant and dielectric loss tangent of olive oils differ slightly from those of other edible oils, as pointed in [70]. Additionally, the dielectric parameters of edible oils were shown to be subtly sensitive to temperature changes at microwave frequencies over a wide temperature range (25 to 180 °C)[71]. Modern microwave engineering tools allow the design and fabrication of complex structures that are sensitive to the environment around them and can track changes in the dielectric constant, making it possible to detect adulterants in EVOO without even directly measuring the dielectric constant of the sample. These complex structures are known as resonators and metamaterials. More details about microwave resonators are provided in chapter 2.

In [72], a microwave resonator-based sensor operating at 5.25 GHz (resonance frequency) is developed to detect adulteration in pure olive oil with castor, mustard and argemone oils. The sensor operates based on shifts in the resonance frequency caused by changes in the dielectric constant of oil samples. The sensor has a rectangular shape with relatively small dimensions (35 x 30 x 16 mm), which makes it portable. The authors claim that the limit of detection (LOD) is 10%, meaning that the sensor can detect adulteration levels as low as 10%, which is similar to that reported in [48] using NMR technique. The structure proposed in [72] is easy to fabricate and use and has very low fabrication costs, making this a very attractive alternative to the conventional methods of identifying adulterations in EVOO.

A submersible microwave sensor based on complementary split ring resonator (CSRR) operating at 11.56 GHz is presented in [73] to distinguish edible oils with close dielectric constants. Additionally, adulteration of edible oils (mustard, sunflower, sesame and olive oil) with mineral oil is probed with the developed sensor. The authors suggest the suitability of the sensor to analyze other liquid products and to replace costly commercially available coaxial probes. Another submersible sensor that could be potentially used for EVOO adulteration is presented in [74]; however, the study did no target specifically adulteration. Instead, authors focus on the dielectric characterization of liquid materials with the sensor and compare the results with an expensive widely accepted commercial dielectric measurement kit. Submersible sensors are non-destructive and usually have great sensibility, but the materials used in their structure may absorb a small volume of sample and change the region of operation of the sensor over time.

An interesting approach combining microwave dielectric spectroscopy, NIR spectroscopy and machine learning is presented in [75]. The developed sensor consists of a transparent cuvette with sample, surrounded by a microwave CSRR, a broadband NIR light source to illuminate the cuvette and a NIR spectrometer to measure the transmission over the cuvette with sample. Different machine learning algorithms are tested to classify the samples between EVOO and not EVOO: artificial neural network (ANN), naïve Bayes gaussian, K-nearest neighbor (KNN) and support vector machine (SVM). All machine learning algorithms achieved 100% accuracy in detecting adulterated samples by using both the data obtained from the resonance of the CSRR and the NIR transmission spectra. The study proves once more how powerful are machine learning algorithms in dealing with high dimensional data.

The modelling of microwave sensors and circuits becomes relatively simple with the available computational tools. However, as the frequency of operation of a system increases, sourcing components at affordable prices becomes more challenging. Therefore, some studies focus on working in lower frequencies. In [76], for instance, a sensor is developed to measure electrical properties (mainly the complex impedance) of 13 different edible oils (EVOO included) from 20 Hz to 1 MHz by applying 400 mV_{RMS} at the sensor's electrodes. In contrast to the impedimetric approach described, in [77] two rectangular electrodes spaced 27 mm apart are excited with a 5 MHz sinusoidal signal with a peak-to-peak voltage of 1.8 V_{p-p} to measure the capacitance of different edible oil samples.

Recent studies have uncovered the potential of dielectric spectroscopy as an alternative method for detecting adulteration in extra virgin olive oil (EVOO). Compared to traditional

techniques like chromatography, NMR, and vibrational spectroscopy, dielectric spectroscopy offers several key advantages. Firstly, it is simple to use, making it accessible to a wider range of users without specialized training. Secondly, its portability allows for *in-situ* analysis, eliminating the need for sample transportation and reducing analysis time. Additionally, dielectric spectroscopy is relatively cost-effective, making it an appealing option for both researchers and industries. Moreover, recent advancements have shown that machine learning algorithms can effectively handle complex spectral data from dielectric spectroscopy. By leveraging machine learning techniques, researchers can develop accurate classification models to identify adulteration in EVOO samples. The integration of dielectric spectroscopy and machine learning presents an exciting opportunity for future research, offering a combined approach that takes advantage of the simplicity and effectiveness of both methods. As such, further exploration and experimentation in this area hold significant promise for improving the detection and prevention of EVOO adulteration in the future.

1.4 ORGANIZATION OF THIS DISSERTATION

An overview of the available techniques to detect adulteration in EVOO is presented to contextualize this dissertation. In this work, a microwave resonator-based sensor excited with transmission lines is developed to detect different adulterants in EVOO, providing both qualitative and quantitative analysis of oil samples. The sensor data is analyzed and processed by artificial neural networks in order to detect adulterated EVOO samples. For this purpose, Chapter 2 provides a comprehensive overview of the microwave theory applied to sensors, discussing about resonators, figures-of-merit, excitation approaches and their use as sensing elements of the environment.

Chapter 3 provides an introduction to artificial neural networks, a powerful machine learning approach to analyze complex data. In this chapter, it is presented the basic mathematic model of an artificial neuron, activation functions, how multiple artificial neurons are interconnected to produce the desired results, training methodology based on gradient descent, data preparation and best practices.

Chapter 2 and 3 are the foundations of the approach presented in this work. The approach itself is explained in detail in Chapter 4. In this chapter, details about the design

procedure of the microwave resonator-based sensor is presented along with the experimental characterization setup of oil samples and the design and training procedures of the neural networks used to detect the adulterant.

Chapter 5 presents the results obtained with the experimental methodology described in Chapter 4, discussing about the accuracy of the neural networks in classifying adulterated samples, the impacts of data preprocessing on the neural network training and the accuracy of the regression models developed to quantify the adulteration level of oil samples. Finally, Chapter 6 concludes this work validating the methodological approach and reinforcing the potential of integrating dielectric spectroscopy and machine learning algorithms to detect adulterants in EVOO. Some texts, figures and tables from Chapters 4 and 5 are reused from [78], with the corresponding permissions of reuse attached in **Appendix B**.

2. MICROWAVE THEORY APPLIED TO RESONANT SENSORS

Electromagnetic field theory is very solid and sophisticated nowadays, once its basic laws have been formulated primarily through experiments conducted since the nineteenth century by many scientists (Faraday, Ampère, Gauss, Lenz, Coulomb, Volta, and others). The main work of James Clerk Maxwell, a Scottish physicist and mathematician, consisted in combining all the laws and principles in a set of four vectorial equations known as Maxwell's equations, capable of describing the electromagnetic field propagation in matter. These four fundamental equations describe how electric and magnetic fields interact and evolve over time in response to various sources and boundary conditions. By applying Maxwell's equations, engineers and scientists can tackle a wide array of electromagnetic problems, from designing antennas and circuits to analyzing electromagnetic interference and radiation patterns.

2.1 CONSTITUTIVE RELATIONS

Materials have some electromagnetic properties that dictate how they interact with external electromagnetic fields. A wave that propagates in free space exhibits a different behavior when propagating in a silicon material, for example. These electromagnetic properties define how the electric and magnetic fields are related to their respective flux densities in different materials through the constitutive relations:

$$\mathbf{D} = \varepsilon \mathbf{E}, \tag{2-1}$$

$$\mathbf{B} = \mu \mathbf{H}, \tag{2-2}$$

$$\mathbf{J} = \sigma \mathbf{E}, \tag{2-3}$$

where **D** is the electric flux density vector, **E** is the electric field vector, **B** is the magnetic flux density vector, **H** is the magnetic field vector, **J** is the current density vector, ε is the electric permittivity of the material, μ is the magnetic permeability and σ is the conductivity of the material [79].

For some materials, applying an electric field **E** will cause the polarization of atoms, creating electric dipole moments that contribute to the total electric flux density **D**. The total contribution is known as dielectric polarization $\mathbf{P_e}$ and it is a function of the applied electric field. For isotropic dielectric materials [79]:

$$\mathbf{D} = \varepsilon_0 \mathbf{E} + \mathbf{P_e}, \quad 2\text{-}4$$

$$\mathbf{P_e} = \varepsilon_0 x_e \mathbf{E}, \quad 2\text{-}5$$

where $\varepsilon_0 = 8.85 \times 10^{-12}$ F/m is the free space permittivity and x_e is the electric susceptibility, which may be a complex value. By replacing equation 2-5 in equation 2-4, we obtain:

$$\mathbf{D} = \varepsilon_0 (1 + x_e)\mathbf{E} = \varepsilon \mathbf{E}. \quad 2\text{-}6$$

Since the electric susceptibility may assume complex values, the permittivity can also be complex:

$$\varepsilon_0 (1 + x_e) = \varepsilon = \varepsilon' - j\varepsilon''. \quad 2\text{-}7$$

Equation 2-7 models the behavior of dielectric materials under oscillating electric fields. The imaginary component of ε accounts for dielectric losses caused by vibrating dipole moments. The dielectric loss tangent ($\tan \delta$) is a measure to characterize the loss of a material, defined by:

$$\tan \delta = \frac{\varepsilon''}{\varepsilon'}. \quad 2\text{-}8$$

Microwave dielectric materials are usually characterized by specifying both the real relative permittivity ε_r and dielectric loss tangent $\tan \delta$ in such a way that the complex permittivity can be written as [79]:

$$\varepsilon = \varepsilon_r \varepsilon_0 [1 - j \tan \delta]. \quad 2\text{-}9$$

A similar modelling approach is found for the magnetic permeability, which also may be complex:

$$\mathbf{B} = \mu_0 (1 + x_m)\mathbf{H} = (\mu' - j\mu'')\mathbf{H} = \mu \mathbf{H}, \quad 2\text{-}10$$

where $\mu_0 = 4\pi \times 10^{-7}$ H/m is the free space permeability and x_m is the magnetic susceptibility. Modern electromagnetic problems often involve the interaction of electromagnetic fields with multiple materials and interfaces, a scenario that cannot be adequately addressed by Maxwell's equations alone. In such cases, it is essential to consider the electromagnetic properties of materials, such as permittivity (ε) and permeability (μ), alongside with boundary conditions and Maxwell's equations. By integrating these factors, it becomes possible to construct solutions for complex structures comprising different materials and interfaces, enabling a comprehensive understanding of electromagnetic phenomena in diverse contexts. The electromagnetic properties of a material, especially the relative permittivity and loss tangent, are of utmost importance for microwave resonant sensors, as these sensors can detect changes in the electromagnetic properties of the measurand. The following section explains the working principle of these sensors.

2.2 PLANAR MICROWAVE RESONANT SENSORS

As seen from transmission line theory, circuits operating at higher frequencies (such as microwaves) can't be described by conventional circuit theory because its electrical size is at the order of wavelength and the phase is not considered constant along circuit elements. Field analysis through Maxwell's equations and boundary conditions can be very cumbersome and usually provides much more information than we actually need for a microwave circuit. When dealing with circuits, we are interested in voltages and currents at specific terminals of circuits instead of knowing the fields quantities for each point in space. Therefore, planar microwave sensors are usually modeled as a 2-port microwave network through the scattering parameters

S, where the quantities of interest are the voltage reflection coefficient on port 1 (S_{11}) and the voltage transmission coefficient from port 1 to port 2 (S_{21}). A brief conceptual review of the scattering parameters of a 2-port microwave network is provided in **Appendix A.1**.

2.2.1 Basic geometries of planar microwave resonant sensors

The typical configuration of planar microwave resonant sensors consists of a microstrip transmission line electrically connected to a resonant element or electromagnetically coupled to it [80]. Both the transmission line and resonant element are usually placed on top of a dielectric substrate with a ground plane, a thickness t_s, dielectric permittivity ε_s and dielectric loss tangent $\tan\delta_s$. The resonant element, however, does not necessarily need to be placed on top of the substrate, along with the transmission line. Instead, it can be etched on the ground plane. **Figure 2.1** presents some possible placements of a very popular resonant element found in literature, known as split ring resonator (SRR), and how these placements interfere on the scattering parameters S_{11} and S_{21} of the structure. In (a), only a microstrip transmission line along with its reflection and transmission coefficients is depicted. In (b), the resonant element is etched on the ground plane and the frequency response of the structure changes due to coupling between the transmission line and resonator, creating a notch (lack of resonance) on S_{21}. This arrangement of (b) is known as complementary SRR, frequently referred as CSRR. In (c), the microstrip transmission line is interrupted preventing energy to flow from port 1 to port 2, and a SRR is inserted in between. However, due to the excitation of the SRR, some energy still flows to port 2 at around 7 GHz, which can be observed by the peak on S_{21}. The frequency response curves of the structures in **Figure 2.1** are obtained by means of simulation, using the finite element software ANSYS HFSS v2022 R2 [81]. It is noteworthy that **Figure 2.1** only presents two possible placements of resonators on a board, however, there are infinite possible rotations and positions of the resonant element. When choosing the position of the resonator, it is important to account for the desired effect on the frequency response, i.e., presence of notches or resonance peaks.

Figure 2.1 – Possible placements of a resonant element on a substrate. (a) depicts a microstrip transmission line electrically connecting two ports with the associated transmission coefficient (S_{21}) and reflection coefficient (S_{11}) as functions of the frequency. (b) presents a case where the resonant element is etched on the ground plane and the effects of this placement in the frequency response. (c) presents a case where the transmission line is interrupted, and the resonant element is inserted in between.

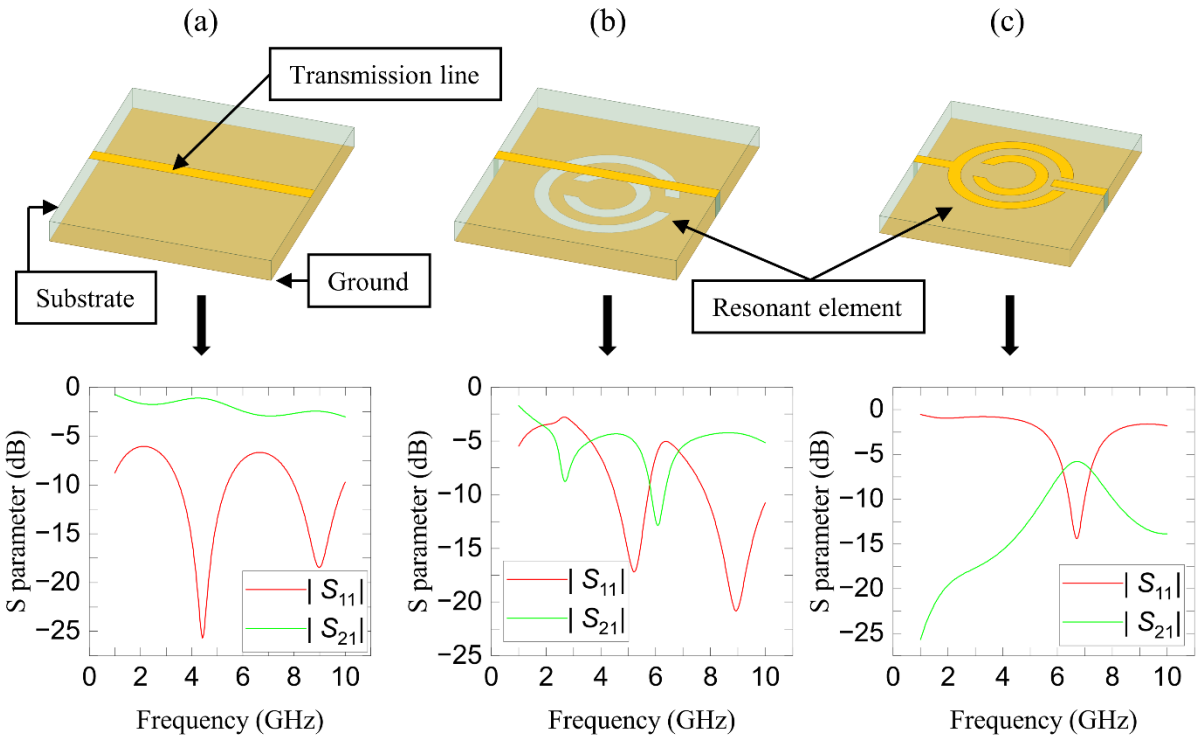

Source: Numerical simulations conducted by the author using Ansys HFSS.

Planar microwave resonant sensors operate based on the variation of the resonance frequency of a resonant element, which occurs due to the interaction of the resonator's field with a material in its vicinity [80], [82]. Such variation of the resonance frequency is explained and modelled by the cavity material perturbation theory [79], through the equation:

$$\Delta\omega \approx \omega_0 \frac{-\int_v (\Delta\varepsilon|\mathbf{E_0}|^2 + \Delta\mu|\mathbf{H_0}|^2)\, dv}{\int_v (\varepsilon|\mathbf{E_0}|^2 + \mu|\mathbf{H_0}|^2)\, dv}, \qquad 2\text{-}11$$

where $\Delta\omega = \omega_r - \omega_0$ is the angular resonance frequency shift, ω_0 is the angular resonance frequency of the unperturbed cavity (which in this case is assumed to be the planar resonator), $\Delta\varepsilon$ and $\Delta\mu$ are respectively the changes in permittivity and permeability due to the introduction of a material in the vicinity of the cavity, $\mathbf{E_0}$ and $\mathbf{H_0}$ are respectively the electric and magnetic

field vectors of the unperturbed cavity, and finally ε and μ are respectively the permittivity and permeability of the medium around the cavity. A better explanation of the cavity material perturbation and the derivation of Equation 2-11 is included in **Appendix A.2**.

2.2.2 The split ring resonator as resonant element

The SRR depicted in **Figure 2.1**(c) is a widely used electrically small planar resonator found in numerous studies, often with many variations, including a squared version of it. A simple SRR model is depicted in **Figure 2.2** along with its equivalent circuit model. When the SRR is excited by an external magnetic field, the interruption in each ring forces the electric current to flow from one ring to another across the slot between them, taking the form of a strong displacement current. The slot and the ring behave as a distributed capacitance, as modeled by the equivalent circuit, where $\frac{C_o}{2}$ is the capacitance associated with each SRR half and L_s is the SRR self-inductance. This capacitance is modeled as [83]

$$C_o = 2\pi r_m C_{pul}, \tag{2-12}$$

where r_m is the mean radius of the SRR and C_{pul} is the capacitance per unit length along the slot between the rings. The resonance angular frequency is therefore defined as [83]:

$$\omega_o = \frac{2}{\sqrt{L_s C_o}} = \sqrt{\frac{2}{\pi r_m L_s C_{pul}}}. \tag{2-13}$$

Figure 2.2 – Simple model of a circular SRR and its equivalent circuit.

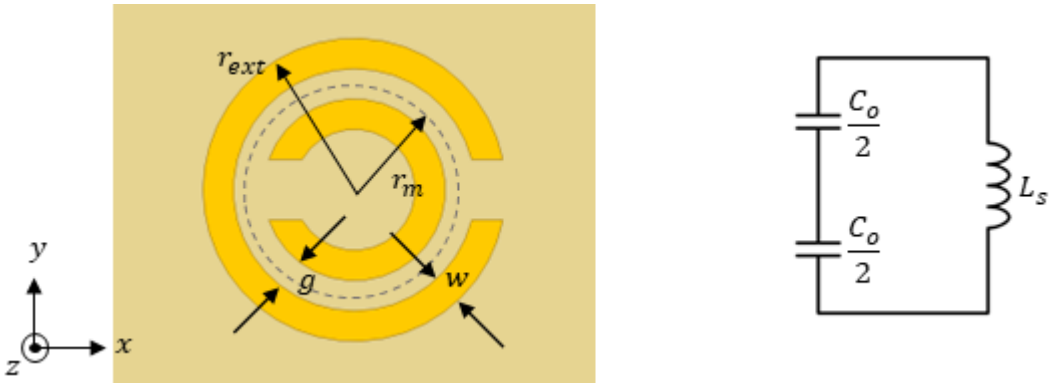

Source: Adapted from [83].

The circuit model of **Figure 2.2** is a reasonable approximation to obtain the resonance frequency of the SRR element, it is valid if the perimeter of the ring is considered small when compared to $\lambda/2$ [83]. The capacitance per unit length C_{pul} is computed in a straightforward way [84]:

$$C_{pul} = \frac{\beta}{\omega Z}, \qquad 2\text{-}14$$

where β and Z are the phase constant and impedance of a pair of coupled metallic strips on a dielectric substrate, respectively, excited at an angular frequency ω. On the other hand, the self-inductance L_s computation is not so straightforward, but it can be assumed to be the inductance of a single equivalent ring with average radius r_m and width w. In this way, L_s is defined as [84]

$$L_s = \frac{\mu_0 \pi^2}{I^2} \int_0^\infty [I(k)]^2 \, k^2 \, dk, \qquad 2\text{-}15$$

where I is the total current intensity supported by the ring and $I(k)$ is the Fourier-Bessel transform of the current $I(r)$ on the ring, defined by

$$I(r) = \int_{r}^{\infty} J_{s,\phi}(r')\ dr', \qquad 2\text{-}16$$

and $J_{s,\phi}$ is the azimuthal surface current density on the ring, defined as:

$$J_{s,\phi}(\mathrm{r}) = \begin{cases} \dfrac{I}{c}, & r_m - \dfrac{w}{2} < r < r_m + \dfrac{w}{2} \\ 0, & \text{otherwise.} \end{cases} \qquad 2\text{-}17$$

Equations **2-12** through **2-17** are the results of many research efforts to obtain approximate expressions for modelling the SRR, and they are capable of modeling the resonant element with reasonable accuracy [83]. However, there are an infinite number of possible resonant elements available. For instance, a simple rectangular, circular or triangular patch can act as a resonator when placed near or connected to planar transmission lines [85], [86], [87].

2.2.3 Sample positioning on a microwave planar sensor

When designing microwave resonant sensors, engineers have numerous options for selecting the resonant element, determining its position and orientation, and choosing the excitation method. The choice will depend on the desired frequency response and the nature of the measurand, henceforth referred to as the material under test (MUT). Microwave resonant sensors are suitable for performing non-destructive measurements of solid, liquid and gaseous MUTs, with the former two being the most typical cases of application of these sensors. If the dimensions of the MUT are relatively small compared to those of the resonant element, then the positioning of the MUT must be carefully chosen to improve sensitivity. **Figure 2.3** illustrates the importance of positioning a relatively small MUT on the planar sensor's surface. As seen in (a), the electric field is more intense in the external ring at the resonance frequency of the SRR (6.69 GHz). In (b), a MUT is positioned at the center of the SRR, where the field intensity is low. As a result, the interaction between the field and MUT is minimal and no changes are observed in the frequency response. However, in (c), the MUT is positioned in a region with an intense electric field, on the SRR, leading to a shift of 140 MHz in the resonance

frequency due to the strong interaction between the field and MUT. Finally, in (d), the MUT is positioned on top of the transmission line connected to port 1, and due to the interaction between the field and the material, a shift of 50 MHz is observed in the resonance frequency.

Figure 2.3 – Effects of different MUT positioning on the frequency response. (a) Shows the normalized E field intensity right above the resonator, at 6.69 GHz. (b) the frequency response when the MUT is at a position with low field intensity. (c) the frequency response when the MUT is at high field intensity position. (d) the frequency response when the MUT is positioned on top of the transmission line.

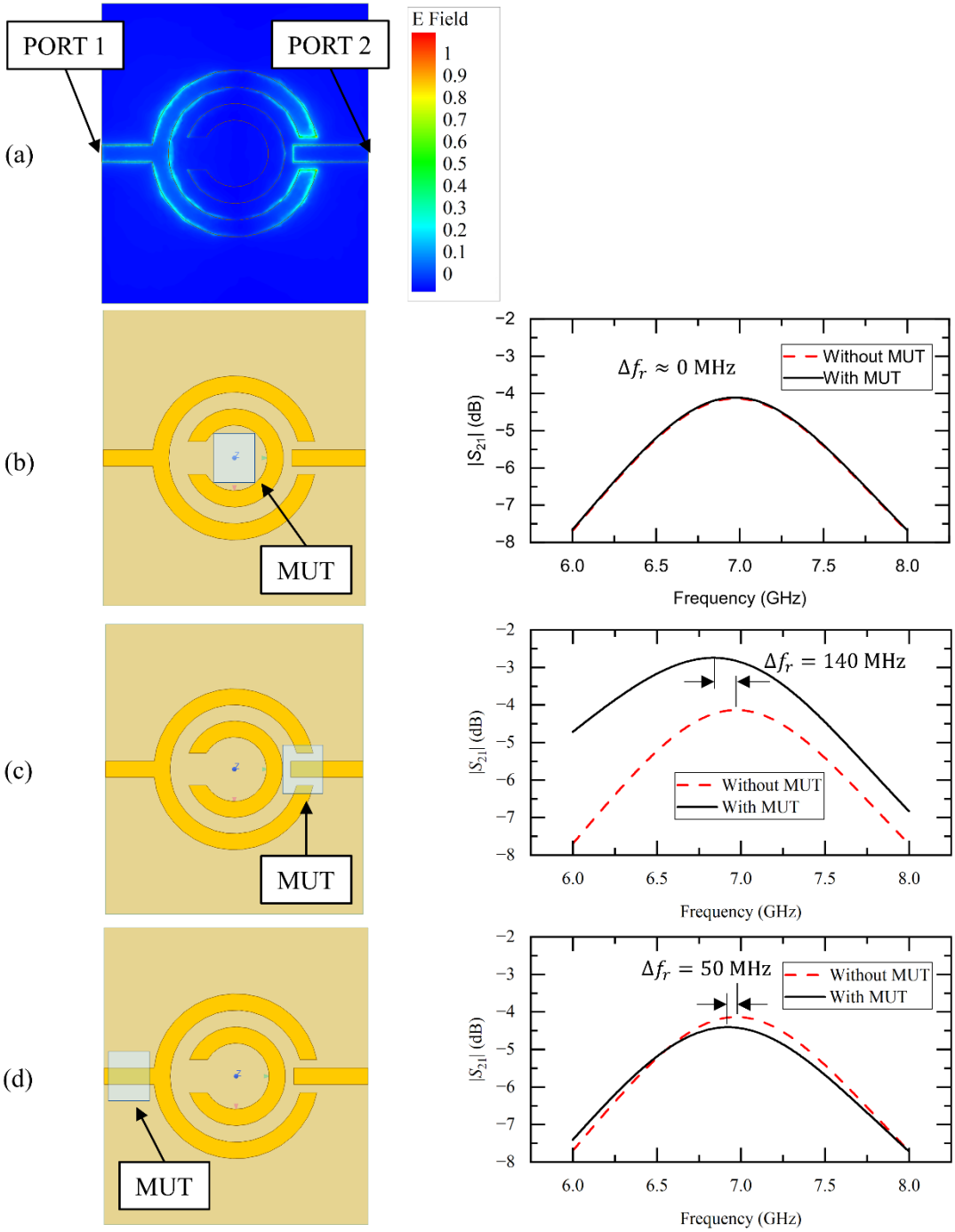

Source: Numerical simulations conducted by the author using Ansys HFSS.

A fundamental observation from **Figure 2.3** is evident: The MUT must be positioned in a region where the electric field is intense in order to obtain improved sensitivity. Therefore, when developing a planar microwave resonant sensor, engineers must have a clear picture of how the material is going to be positioned, the extent to which it covers the resonator, and the expected range of permittivity of the MUT. Additionally, **Figure 2.3** also demonstrates why tracking changes in the permittivity of MUTs is preferable using resonators rather than transmission lines alone. Resonators exhibits greater sensitivity to material perturbations compared to transmission lines, making them valuable in scenarios where sensitivity is crucial. When the MUT is positioned as in (c), it increases the coupling between the external ring and the transmission line directly connected to port 2, resulting in an increase in the transmission coefficient. This positioning not only causes a higher resonance frequency shift, but also increases the transmission coefficient.

2.2.4 Typical sensor response to variations of relative permittivity

So far, we have discussed how resonant elements work and their usage in microwave planar sensors. Now, let's turn our attention to understanding the relationship between the frequency response of the sensor and the dielectric properties of the MUT. Planar microwave resonant sensors are essentially sensitive to changes in the permittivity of dielectric materials [88]. Moreover, the complex permittivity of materials is strongly dependent on their atomic organization [89]. Therefore, changes of chemical or physical nature on the atomic organization of materials will directly impact on the complex permittivity of these materials.

In order to understand how the frequency response of a sensor behaves as the permittivity of the MUT changes, we consider the same arrangement of **Figure 2.3(c)**. Instead of varying the position of the same MUT as in **Figure 2.3**, we now keep the MUT at a fixed position and change its relative permittivity ε_{MUT}. **Figure 2.4** depicts what happens when materials with different values of relative permittivity, but with same dimensions and positioning, interact with the SRR. In (a), it is evident that increasing the relative permittivity causes not only a shift in the resonance frequency to lower frequencies, but also an increase in the transmission coefficient. On the other hand, (b) illustrates how much the resonance frequency shifts from the unloaded resonance frequency f_0 in terms of $\Delta f_r = f_r - f_0$. The

values of Δf_r become more negative as the permittivity increases because the resonance frequency decreases (shifts left). This behavior is explained by **Equation 2-11**, which states that a change on either the permittivity $\Delta\varepsilon$ or permeability $\Delta\mu$ will make the relation $\Delta\omega = \omega_r - \omega_0$ even more negative, thus indicating that the resonance frequency of the sensor decreases. Moreover, the curve in (b) suggests that there is a limitation of the sensor in differentiating materials with high relative permittivity due to the apparent monotonic decreasing exponential behavior. Additionally, this curve suggests that the sensor is more sensitive to lower values of permittivity.

Figure 2.4 – Effects of varying the relative permittivity of the MUT on top of a SRR. (a) Changes on the transmission coefficient for different values of relative permittivity and (b) the resonance frequency shift $\Delta f_r = f_r - f_0$.

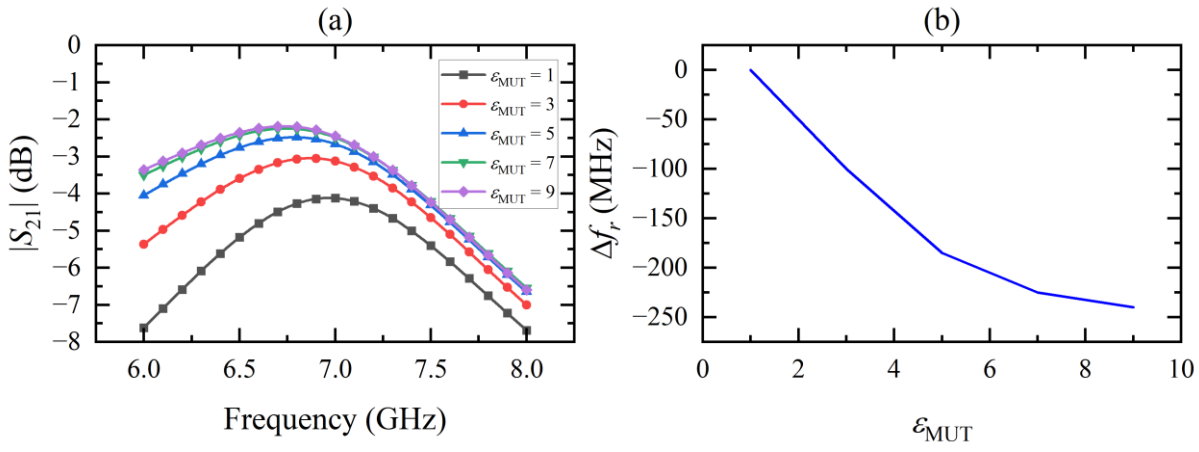

Source: Numerical simulations conducted by the author using Ansys HFSS.

2.2.5 Effects of the substrate on the sensor operation

Choosing a suitable substrate for the sensor design is important because it directly impacts on the sensor dimensions and sensitivity. Dielectric substrates come with different typical values of permittivity (ε_s), loss tangent ($\tan\delta_s$) and thickness. It is important to know the way these properties influence on the resonance frequency and operating conditions of the sensor. **Table 2.1** presents common dielectric substrates and their respective relative permittivity and loss tangent [90], [91], [92], [93]. From this table, FR4 and Rogers RT5880

are commonly found in literature of planar microwave sensors. Additionally, thin polyimide films are the preferred substrate option for flexible printed circuit board (PCB) designs.

Table 2.1 – Values of relative permittivity ε_s and dielectric loss tangent $\tan\delta_s$ for different dielectric substrates.

Substrate	$\boldsymbol{\varepsilon_s}$	$\boldsymbol{\tan\delta_s}$
Rogers RT5880	2.2	0.0009
Arlon AD250	2.5	0.0018
Arlon AD300	3	0.0030
Arlon AR450	4.5	0.0035
Arlon AR600	6	0.0035
Teflon	2.1	0.0002
Rogers RO3010	10.2	0.0022
FR4 epoxy	4.4	0.0200
Polyimide HD-4110	3.3	0.0200
Alumina TMM 10i	9.8	0.0020

Source: [90], [91], [92], [93].

Similarly to how the permittivity of a MUT impacts the resonance frequency of the resonant element, the permittivity of the substrate ε_s also impacts the frequency response. This condition is illustrated in **Figure 2.5**, where the dielectric loss tangent of the substrate is set to zero and the substrate thickness is 1.6 mm. Just like with a MUT, for dielectric substrates, higher values of permittivity are also associated with lower resonance frequencies. This behavior directly impacts the sensor's dimensions, as smaller resonant elements are typically associated with higher resonance frequencies (and smaller wavelengths) [94], engineers can choose a higher permittivity substrate to decrease the operating frequency of the structure, consequently decreasing the cost of circuitry involved. Therefore, the substrate permittivity is an extremely important parameter for size critical applications.

Dielectric loss tangent ($\tan\delta_s$) is another parameter that influences the sensor's behavior, particularly its sensitivity. The relationship between the transmission coefficient and the loss tangent is illustrated in **Figure 2.6**. In (a), it is evident that the transmission coefficient decreases as the loss tangent increases. This outcome is expected because in planar sensors, most of the electromagnetic energy is typically confined inside the substrate [82]. Therefore, a

higher loss tangent increases the dissipation of this energy, resulting in less power being delivered to port 2. As we will explore in the next section, this property directly impacts a figure of merit of the sensor, known as quality factor. In (b) it is possible to observe how the intensity of the signal at the resonance frequency f_r (6.71 GHz) linearly decreases with the increase in $\tan\delta_s$. It is noteworthy that the loss tangent does not impact the resonance frequency of the sensor.

Figure 2.5 – Effects of the substrate relative permittivity ε_s on the transmission coefficient of the sensor when the dielectric loss tangent is set to $\tan\delta_s = 0$ and the substrate thickness is $t_s = 1.6$ mm. The same behavior is observed when varying the relative permittivity of a MUT. Higher values of permittivity are associated with lower resonance frequencies.

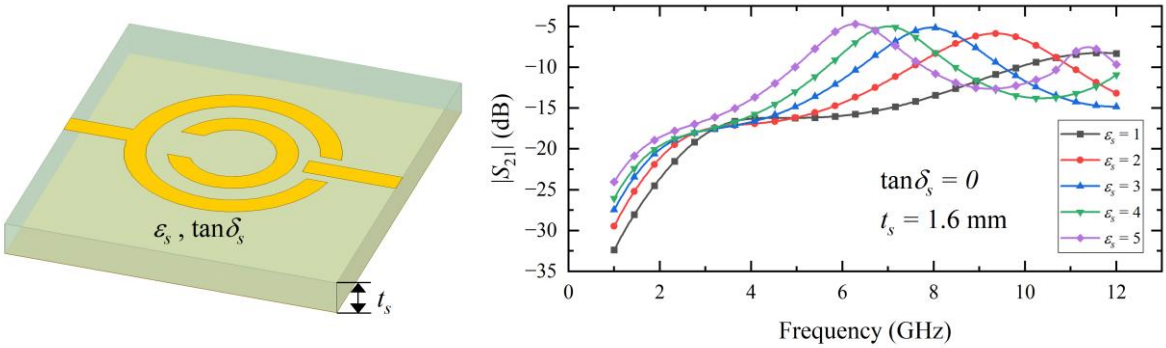

Source: Numerical simulations conducted by the author using Ansys HFSS.

Figure 2.6 – Effects of the substrate dielectric loss tangent on the transmission coefficient of the sensor when the substrate relative permittivity is set to $\varepsilon_s = 4.4$ and the substrate thickness is $t_s = 1.6$ mm. (a) depicts the behavior of $|S_{21}|$ for different values of $\tan\delta_s$, and only the amplitude of the signal is affected, mainly at the resonance frequency f_r. (b) presents the variations of amplitude in $|S_{21}|$ at the resonance frequency f_r (6.71 GHz) as the dielectric loss tangent increases.

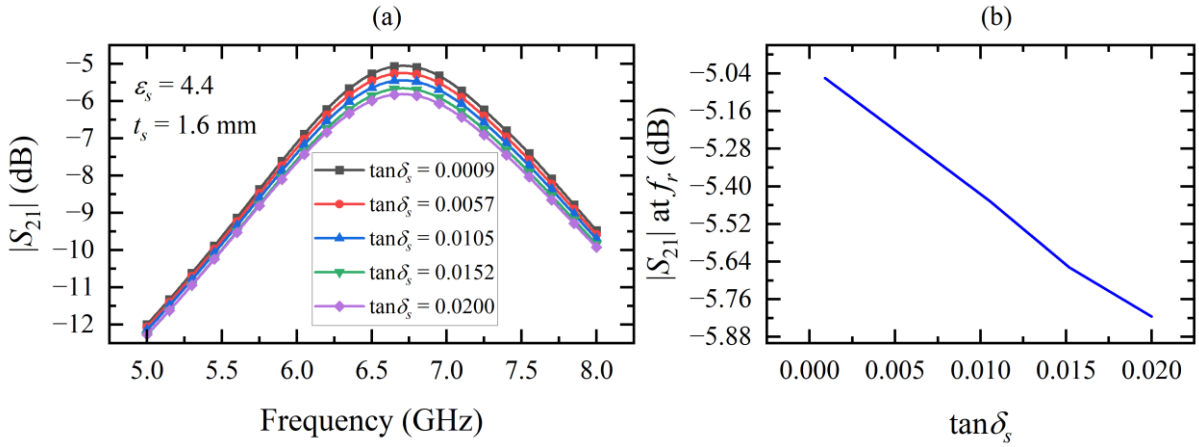

Source: Numerical simulations conducted by the author using Ansys HFSS.

The thickness of the substrate in microwave planar sensors significantly influences their performance and characteristics. A key effect of substrate thickness is on the propagation delay of electromagnetic waves; thicker substrates increase the delay because the signal travels a longer path through the material. This increased delay can affect the timing and phase of the signals, which is critical in high-frequency applications. Additionally, the characteristic impedance of the sensor's microstrip lines is affected by substrate thickness [95], which may require careful impedance matching to avoid power reflection. Another important aspect is dispersion, where thicker substrates cause greater separation of frequency components due to different propagation velocities, potentially distorting the signal and limiting bandwidth. Furthermore, substrate thickness impacts attenuation, with thicker substrates typically providing better isolation and lower losses due to reduced coupling to the ground plane. This situation is illustrated in **Figure 2.7**. However, this also means that the sensor can become less sensitive to small changes in the material under test, as the electromagnetic energy may be mostly confined in the substrate. As seen from **Figure 2.7**, the transmission stop increasing for substrate thicknesses higher than 1.9 mm. In fact, after this point, the transmission may start decreasing due to increased dielectric losses. Therefore, the choice of substrate thickness is also a crucial design consideration, balancing factors such as propagation delay, impedance, dispersion, and attenuation to achieve an optimal sensor performance.

Figure 2.7 – Effects of the substrate thickness on the transmission coefficient of the planar sensor when the substrate is FR4 ($\varepsilon_s = 4.4$ and $\tan \delta_s = 0.02$). Thicker substrates reduce the conductivity losses caused by the ground plane; however, they concurrently increase the dielectric losses.

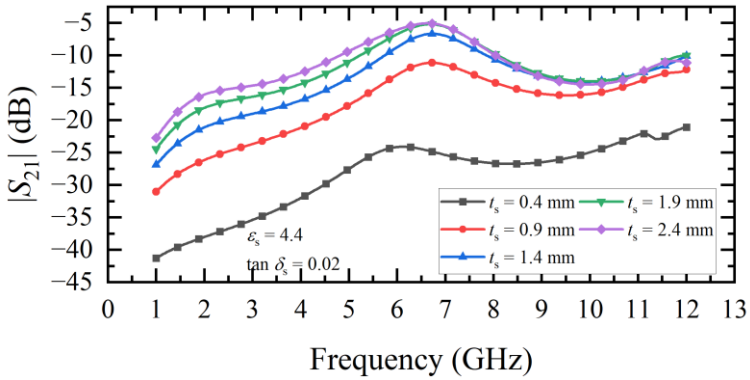

Source: Numerical simulations conducted by the author using Ansys HFSS.

2.3 FIGURES OF MERIT OF MICROWAVE SENSORS

In this section, we will delve into the most common figures of merit of microwave sensors found in literature, focusing particularly on the Quality factor (Q factor) and Sensitivity. These parameters are crucial for evaluating and optimizing the performance of microwave sensors, as they directly influence the sensor's ability to accurately detect and measure changes in the MUT. The Quality factor quantifies the sharpness of the resonance, while the Sensitivity measures the sensor's response to variations in the material's properties. Additionally, we will explore other important figures of merit, including Selectivity, which assesses the sensor's ability to distinguish between different substances, and Repeatability, which evaluates the consistency of the sensor's measurements over multiple trials. Understanding these metrics, along with others such as Linearity, will provide a comprehensive understanding of the various factors that contribute to the overall efficacy and reliability of planar microwave sensors.

2.3.1 Quality factor (Q)

The physical meaning of quality factor is actually related with the losses of a resonant structure. These losses may be due to conductor losses, dielectric losses or radiation losses. The formal definition of Q is the ratio of the average energy stored in a resonant cavity U to the energy loss per second P_{loss} (dissipated power) [79]:

$$Q = \omega \frac{U}{P_{loss}}, \qquad 2\text{-}18$$

where ω is the angular frequency of excitation. From this equation, it is evident that a resonant structure with higher losses will exhibit a lower Q. In fact, the substrate dielectric losses on planar microwave sensors are a major concern for high-Q applications.

Although efficient for the computation of the quality factor of RLC resonant circuits, **Equation 2-18** is not in a very friendly form to compute the quality factor of resonant

microwave structures. This is because the equation requires information regarding the **E** and **H** fields distribution in the structure to compute the energy stored, which in most cases can only be obtained by means of numerical simulation. Directly measuring this energy is not possible, as any measuring system will cause a loading effect on the resonant cavity. Therefore, another alternative approach extensively used in literature to measure the quality factor uses the $|S_{21}|$ curves. Let us consider two different frequency responses of arbitrary resonant structures, as illustrated in **Figure 2.8**. In (a), the arbitrary structure behaves like a band-pass filter, while the structure in (b) behaves like a band-stop filter. The first quantity of interest to compute the quality factor of both structures is the frequency of resonance f_r. The second quantity of interest refers to the half-power bandwidth $\Delta f_{3\text{dB}}$. For both cases, the quality factor Q can be determined as [88], [96]:

$$Q = \frac{f_r}{\Delta f_{3dB}}. \qquad 2\text{-}19$$

Figure 2.8 – Arbitrary resonant structure's $|S_{21}|$ curves and the parameters required to compute the structure's Q factor for the cases when the curves behave like (a) band-pass filters and (b) band-stop filters.

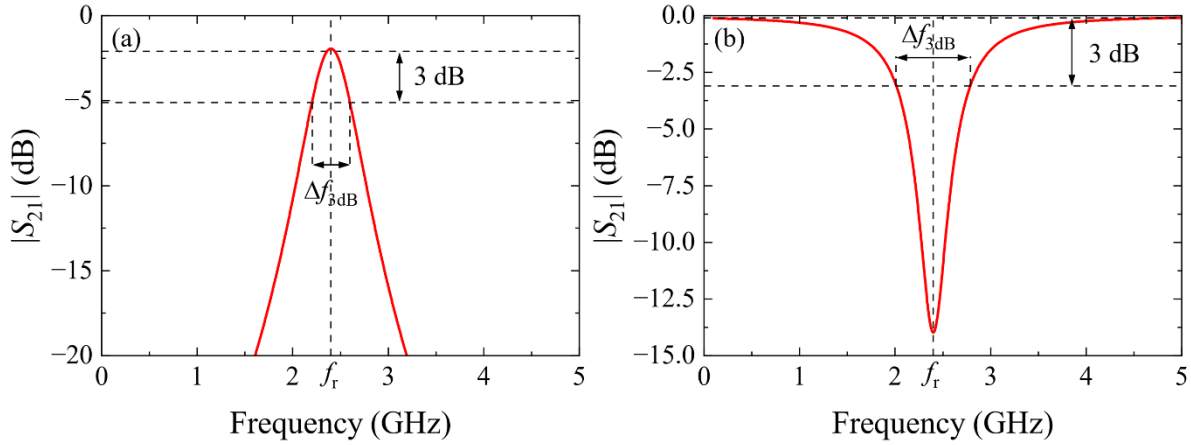

Source: Adapted from [88].

The previous statement that the Quality factor is a metric of the sharpness of a resonance becomes more evident with **Equation 2-19**. Sharper resonances result in lower $\Delta f_{3\text{dB}}$, which result in higher values of Q. Moreover, substrates and MUTs with higher losses will dissipate more power, causing Q to decrease in **Equation 2-18**, which can only lead to an increase in Δf_{3dB} in **Equation 2-19**, as the resonance frequency f_r is not affected by dielectric losses (see

Figure 2.6). In summary, resonant sensors developed on low-loss substrates are capable of achieving higher values of Q. Obviously, changing from a cheap lossy substrate to a high-cost low-loss substrate is not the only option to increase the quality factor of a structure. In fact, optimization approaches seek for obtaining higher values of Q by changing the geometry of the resonator and/or transmission line, consequently changing the field profile and coupling of energy. Additionally, loading multiple resonant elements to the transmission line to exploit the coupling between them can improve the results [82].

Some possible application scenarios of microwave planar resonant sensors usually require high sensitivity, and consequently, higher quality factors. To further illustrate the importance of a high Q and sharp resonance, we consider two arbitrary resonant structures whose resonance frequency are the same, but with different values of Q, as illustrated in **Figure 2.9(a)**. The red curve corresponds to a structure with $Q = 11.5$, while the blue curve corresponds to a structure with $Q = 22.7$. It is clear that the resonance peak of the blue curve is sharper. If we measure the transmission coefficient only at 3 GHz every time both structures experience shifts in resonance frequency due to changes in the relative permittivity of the surrounding environment, the results of **Figure 2.9(b)** are obtained. The structure with higher Q exhibits greater variations in $|S_{21}|$, which, depending on the electronics used for reading the sensor output, may allow us to measure more levels of the desired MUT's property without the error signal significantly interfering with the results.

Figure 2.9 – The frequency response for two different arbitrary sensors. (a) the resonance frequency is the same for both structures, while the Q factor is different. (b) the value of $|S_{21}|$ measured at the resonance frequency when both structures experience the same shifts in resonance frequency Δf_r.

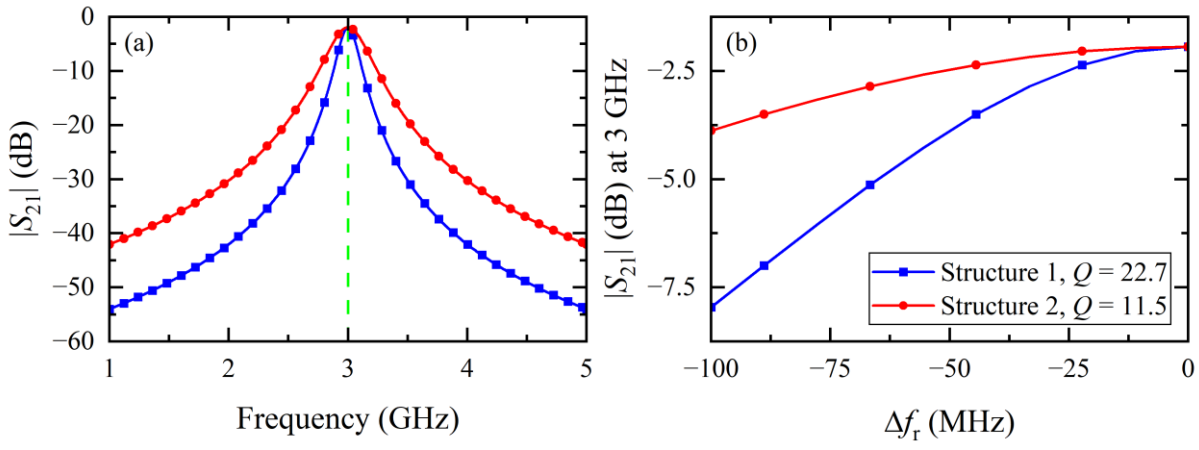

Source: Numerical tests conducted by the author.

2.3.2 Sensitivity

Sensitivity (S) is a crucial parameter for microwave sensors, defining the sensor's ability to detect small changes in the MUT. Sensitivity in the context of microwave sensors is often quantified as the rate of change in a measurable parameter (such as resonance frequency or transmission coefficient) relative to a change in the property of the MUT (e.g., permittivity or dielectric constant). Mathematically, its most general definition found in the literature is [97]:

$$S = \frac{\Delta f_r}{\Delta \varepsilon_{MUT}}, \tag{2-20}$$

where Δf_r is the sensor's resonance frequency shift observed when the MUT's permittivity changes by $\Delta \varepsilon_{MUT}$. However, the equation above may give a false understanding that the relationship between Δf_r and $\Delta \varepsilon_{MUT}$ is linear, which in fact, usually is not. A more coherent definition takes the derivative form [82]:

$$S = \frac{df_r}{d\varepsilon_{MUT}}. \tag{2-21}$$

Referring once more to **Figure 2.4**, which illustrates Δf_r as the relative permittivity of the MUT changes, it is clear that the sensitivity is variable. For instance, in the referred figure, the sensitivity is higher when the relative permittivity of the MUT is lower. This is verified by the slope of the curve in **Figure 2.4(b)**, which is higher for smaller values of ε_{MUT}. The figure also suggests the importance of knowing in advance the expected relative permittivity range the MUT may assume, otherwise the sensor may not be sensitive enough for the desired application. In the literature of microwave sensors, when provided, the authors usually provide the maximum sensitivity obtained during the experimental step of their work. Additionally, comparing the sensitivity of two different sensors with the results derived from **Equation 2-21** may result in an unfair comparison if one of the sensors operates at a much higher frequency than the other. This is because sensors operating at gigahertz frequencies may produce resonance frequency shifts on the order of hundreds of megahertz, while sensors operating at megahertz frequencies may produce resonance frequency shifts on the order of

kilohertz. Therefore, it is a common practice to normalize the sensitivity of the sensor by the resonance frequency f_r [82]:

$$S = \frac{1}{f_r}\frac{df_r}{d\varepsilon_{MUT}}. \quad 2\text{-}22$$

A higher sensitivity means that the sensor can detect smaller changes in the MUT's properties, which is crucial for precision-critical applications. It is evident that the sensitivity has a relationship with the quality factor. This is explained by the fact that higher values of Q allows the resonator to store more energy, and the more this energy interacts with the MUT, the higher the variations in the sensor's output. However, the quality factor is not the only variable that impacts on the sensitivity. Referring to **Figure 2.3**, it is evident that the MUT's positioning on the sensor drastically impacts the sensitivity. High quality factors are useless if the positioning of the MUT is not suitable, and the opposite is also true.

2.3.3 Other application-specific figures of merit

The limit of detection (LOD) of microwave sensors refers to the smallest measurable change in the MUT that can be reliably detected by the sensor. This is a critical parameter as it determines the sensor's ability to detect low concentrations or minimal changes in the properties of the MUT. The LOD is influenced by several factors, including the quality factor of the resonator, the noise level of the measurement system, and the sensitivity of the sensor. Higher Q factors and lower noise levels generally contribute to a lower (better) limit of detection [98]. Additionally, the frequency at which the sensor operates can also affect the LOD, therefore it is important to have a clear picture of the dielectric properties of the MUT at the operating frequency. Understanding and optimizing the LOD is essential for applications where detecting minute changes is crucial, such as in biochemical sensing or detecting trace contaminants.

Selectivity is another important figure of merit for microwave sensors, defining the sensor's ability to distinguish between different analytes or to selectively detect a particular analyte in the presence of other substances. High selectivity ensures that the sensor can accurately identify and measure the target material under test (MUT) without interference from

other materials or environmental factors [99]. To achieve selectivity, again it is important to have an idea of the frequency behavior of the MUT's complex permittivity to design the sensor to resonate at specific frequencies that correspond to unique electromagnetic properties of the MUT or a specific substance in the analyte. Additional signal processing techniques and multivariate analysis also plays an important role in improving the sensor's selectivity. High selectivity is crucial in applications where accurate identification and measurement of specific substances are required, such as in environmental monitoring, biomedical diagnostics, and food quality control. Improving selectivity reduces false positives and enhances the reliability of the sensor's readings, making it more effective and efficient for its intended application.

Repeatability is a vital performance characteristic of microwave sensors, referring to the sensor's ability to produce consistent and reliable measurements when the MUT is measured multiple times under the same conditions [100]. High repeatability ensures that the sensor's outputs are stable and reproducible, which is essential for accurate monitoring and analysis. Environmental parameters, such as temperature and humidity, often impacts the substrate's dielectric properties, which makes it important to consider the sensor's operating temperature range when using substrates more susceptible to environmental changes. Additionally, planar resonant sensors are highly sensitive to MUT's placement, often requiring specific measurement setups to ensure consistent placement and alignment of the MUT relative to the sensor. Finally, both the sensor and measurement circuit are susceptible to noise, which in some application may require additional signal processing tools, such as filtering. Recently developed sensors have more credibility if the work that introduce them conducts a study on the sensor's repeatability. This can be accomplished by measuring the MUT under the same conditions multiple times and providing the reader with simple metrics of dispersion, such as the standard deviation of the measurements [100]. Ensuring repeatability improves the reliability of the sensor's data, making it a dependable tool for monitoring and analysis.

Linearity is a desired characteristic of microwave sensors, referring to the proportional relationship between the input (changes in the permittivity of MUTs) and the output response (such as shifts in resonance frequency or variations in the transmission/reflection coefficient). High linearity ensures that the sensor's output proportionally reflects the changes in the measured parameter, which simplifies data interpretation and facilitates to develop calibration equations to predict the MUT's properties from the sensor's response [101].

Finally, the dynamic range is a fundamental parameter of sensors, indicating the range of input values or conditions over which the sensor can provide accurate and reliable

measurements. A wide dynamic range is desirable in microwave sensors as it allows for the detection and measurement of both small and large variations in the properties of the MUT. The quality factor and sensitivity have great impact on the LOD and dynamic range metrics of a sensor. In literature, planar microwave sensors developed for specific applications usually have their quality factor, sensitivity and dynamic range specified for the study completeness.

2.4 MICROWAVE SPOOF LOCALIZED SURFACE PLASMONS

Localized surface plasmons (LSPs) are localized oscillations of free electrons in metal nanoparticles at optical frequencies. When dealing with LSPs modes, the confined mode profile and near-field enhancement make LSPs very sensitive to dielectric changes of the environment, thus localized surface plasmons have very good sensing capabilities. Structures that comport LSP modes usually have subwavelength dimensions, a desirable property for miniaturization of sensors. However, natural plasmons exist only in visible and near-infrared frequencies because metals behave like perfect electric conductors (PECs) at lower frequencies such as terahertz and microwaves, allowing just a small fraction of the electric field to penetrate into the metal and consequently blocking confinement [96].

Although Localized Surface Plasmons are typically observed at optical frequencies, similar behaviors have been demonstrated at microwave and terahertz frequencies. These phenomena are referred to as "Spoof Localized Surface Plasmons" [102]. Spoof LSPs are spoof achieved using corrugated PEC metamaterials, which are engineered to artificially exhibit negative permittivity behavior at these lower frequencies [96]. Initially, Spoof LSPs were realized in two dimensions for both infinitely and finitely thick corrugated metal cylinders (such as the one illustrated in **Figure 2.10**) in [102], where the authors also provided an approximation of the corrugated cylinder to an effective inhomogeneous anisotropic medium, as illustrated in **Figure 2.10 (b)**. Later, the existence of spoof LSP modes was numerically and experimentally demonstrated for ultrathin textured metallic disks [103] and ultrathin spiral arms [104], which paved the path for the development of planar resonant structures that take fully advantage of the outstanding environmental sensitivity of spoof LSP modes [105].

Figure 2.10 – (a) Geometry of the corrugated PEC cylinder that supports spoof LSP modes, where the grooves are filled with a dielectric of permittivity ε_g, the inner radius is r and the outer radius is R. (b) The groove region can be approximated to a metamaterial with effective permittivity ε_{eff}.

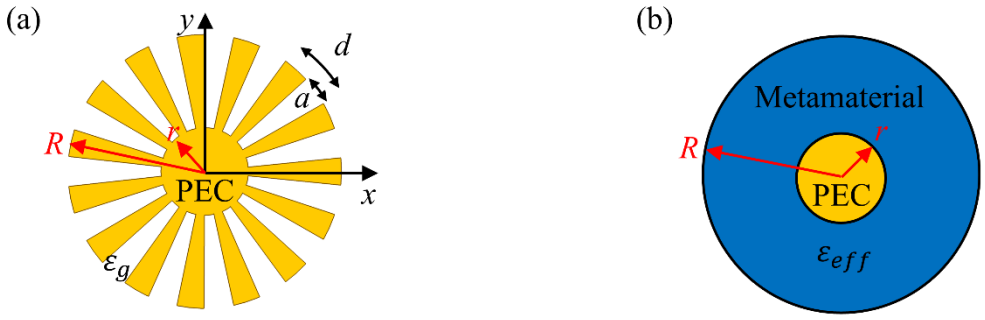

Source: Adapted from [102].

Planar spoof LSP resonant structures offer several significant benefits in the realm of microwave and terahertz technologies. One of the primary advantages is their ability to achieve strong electromagnetic field confinement and enhancement at subwavelength scales [96]. This enhanced field localization leads to increased interaction with materials placed in the vicinity of the resonant structure, making these devices particularly useful for sensing applications. The sensitivity of sensors based on spoof LSPs is markedly higher compared to traditional microwave sensors, allowing for the detection of minute changes in the material properties of the test samples. This high sensitivity is crucial in applications ranging from biomedical diagnostics [106] to environmental monitoring [107], where detecting small amounts of substances can be vital.

Another notable benefit of planar spoof LSP resonant structures is their compatibility with existing planar fabrication techniques, which are widely used in the semiconductor industry. This compatibility allows for the integration of spoof LSP structures into compact, planar devices that can be easily fabricated at a relatively low cost. The planar nature of these structures also enables them to be incorporated into flexible and wearable electronics, expanding their potential applications to include advanced communication systems, flexible sensors, and even smart textiles. Moreover, the ability to tailor the resonant frequency through the design of the geometric features of the metamaterial provides a high degree of tunability and adaptability, making spoof LSP resonant structures versatile components in the design of next-generation microwave and terahertz devices.

Typical ultrathin spoof LSP resonators that are incorporated into planar sensors are composed of straight or spiral metallic arms, positioned on top of a dielectric layer to produce a negative effective permittivity behavior. The basic geometries along with their first order mode profile are illustrated in **Figure 2.11**. Resonance frequencies are generally governed by the effective length of the arms, therefore curved arm patterns may compact the resonator into subwavelength scale. The electromagnetic field, and consequently the electromagnetic energy, is highly confined in these relatively small structures, a desirable condition for sensing MUT's dielectric properties.

Figure 2.11 – Base geometries of planar resonators supporting spoof LSP modes. (a) the grooved circular patch and (c) its first order mode profile simulated in HFSS. (b) the spiral arms and (d) its first order mode profile.

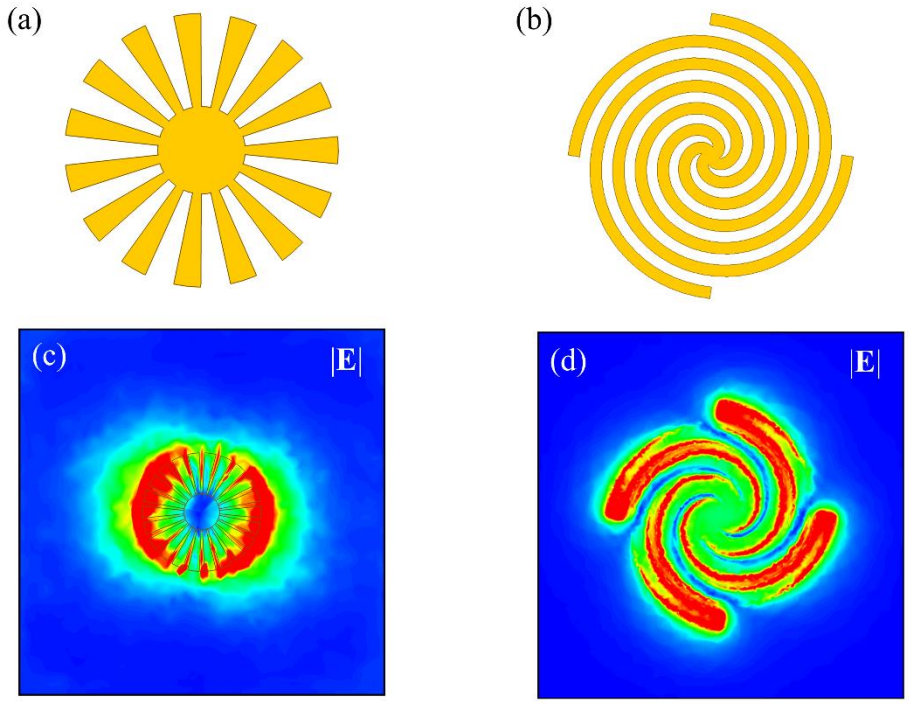

Source: Numerical simulations conducted by the author using Ansys HFSS.

Excitation of spoof LSP modes can be accomplished by different methods such as probe excitation, free-space excitation, microstrip transmission lines and coplanar waveguide (CPW) transmission lines [108], as illustrated in **Figure 2.12**. By placing a spoof LSP resonator near a microstrip transmission line, as shown in **Figure 2.12(c)**, it is possible to transfer energy from the transmission line to the resonator to excite the LSP mode. Connecting each end of the transmission line to a port on a vector network analyzer (VNA) allows the measuring of

scattering parameters of the formed microwave network. The distance between the resonator and transmission line as well as the propagation constant of the line will be the key factors to ensure good coupling between the localized mode of the resonator and the propagating mode of the line. The coupling can be verified by noticing the presence of resonances in the $|S_{11}|$ and $|S_{21}|$ parameters of the network. The addition of a MUT on the vicinity of the resonator will disturb the coupling, thus altering the measured scattering parameters.

Figure 2.12 – Different spoof LSP mode excitation approaches. (a) free space excitation by an incident wave irradiated from an antenna. (b) monopole antenna excitation and probing. (c) microstrip transmission line coupling. (d) CPW transmission line coupling.

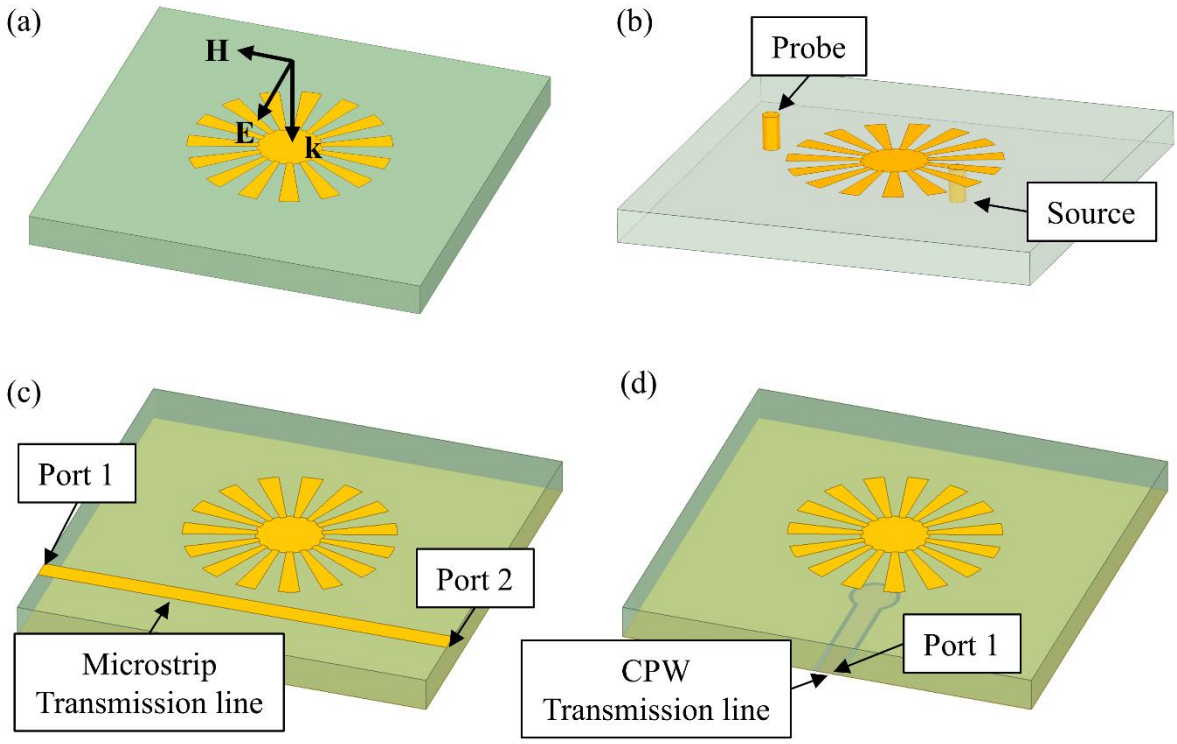

Source: Adapted from [108].

It has been reported that spoof LSP resonators, when excited properly, exhibit high quality factors. Due to the near field enhancement, their capabilities of sensing minute changes in the surroundings of the resonator are very good, making them an attractive option as sensing elements. Furthermore, due to its subwavelength dimensions, miniaturization of sensors and integration in microwave networks can be accomplished quite easily [96], [108].

3. ARTIFICIAL NEURAL NETWORKS

Artificial Neural Networks (ANNs) are computational models inspired by the human brain's neural architecture, designed to recognize patterns, learn from data, and make decisions. Composed of interconnected artificial neurons that mimic biological neurons, ANNs process information through layers that transform inputs into meaningful outputs. Each connection between neurons carries a weight, which is adjusted as the network learns, optimizing the model's ability to perform specific tasks. Widely used in various fields such as image and speech recognition, natural language processing, and autonomous systems, ANNs have revolutionized the approach to complex problem-solving, offering robust solutions where traditional algorithms fall short. Their ability to learn and generalize from vast amounts of data makes them the foundation of modern artificial intelligence and machine learning applications. In this chapter, some basic key concepts are introduced for the reader's understanding, as these concepts will be important for subsequent discussions in Chapter 4.

3.1 PERCEPTRON: THE ARTIFICIAL NEURON MODEL

The Perceptron is the simplest form of an artificial neural network, serving as a fundamental building block for more complex structures. The Perceptron is a type of linear classifier model that can solve simple multivariate classification problems. A simple representation of this model is illustrated in **Figure 3.1** [109]. The Perceptron is typically applied to classification problems where the user wants to categorize a sample based on the features $x_1, x_2, \ldots, x_n$ observed for this sample. Mathematically, the perceptron of **Figure 3.1** will output a result:

$$u = -w_0 + \sum_{i=1}^{n} w_i \, x_i, \tag{3-1}$$

$$y = f(u). \tag{3-2}$$

Figure 3.1 – Representation of the Perceptron as a system with multiple inputs and a single output. The input variables x_1, x_2, …, x_n, also commonly referred to as "features" are characteristics of a collected sample that is to be analyzed and categorized by the model. The output variable y corresponds to the decision of the model.

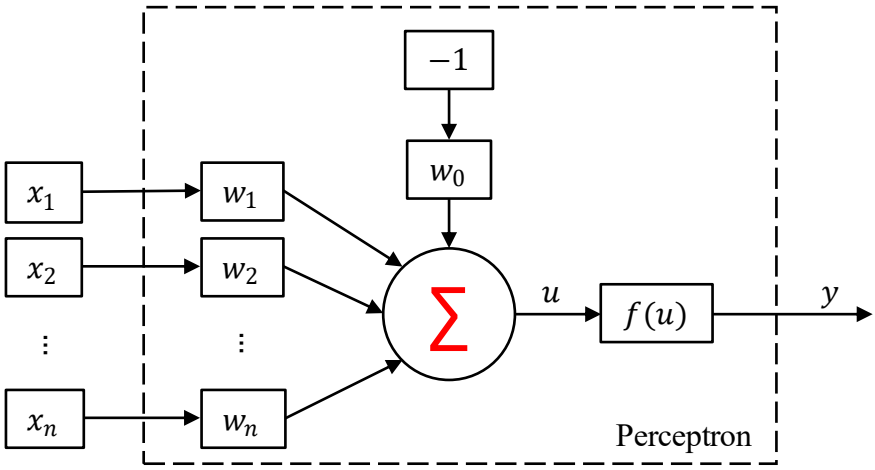

Source: Adapted from [109].

Although **Equation 3-1** may look like a simple linear combination, its significance for the comprehension of the Perceptron is considerable. First, the term w_0 that do not multiply any feature x is often referred to as bias. Its importance will be clear soon. Second, the terms w_1, w_2, …, w_n are known as weights. The weight can be understood as the level of significance the feature associated with it has in the response of the Perceptron. In fact, the so-called process of "training" or "learning" consists of basically adjusting the weights and bias, so the model produces the expected output [109]. Finally, the only element left to define is the function $f(u)$ in **Equation 3-2**, known as "activation function" in the context of artificial neural networks. Given the architecture of the Perceptron, it can only produce a binary output and typically the activation function $f(u)$ can either be the Sign function:

$$y = \begin{cases} -1, & u < 0 \\ 1, & u \geq 0' \end{cases} \qquad 3\text{-}3$$

or the Heaviside step function:

$$y = \begin{cases} 0, & u < 0 \\ 1, & u \geq 0 \end{cases}. \qquad 3\text{-}4$$

Let us consider two different groups (or classes) A and B, with features x_1 and x_2. The Perceptron can be applied to analyze the inputs x_1 and x_2 and decide whether the sample it is analyzing belongs to class A or B. For instance, the output can be -1 if the sample belongs to class A, and 1 if the sample belongs to class B. For this purpose, the sum operation in **Equation 3-1** becomes critical in the decision:

$$u = -w_0 + w_1 x_1 + w_2 x_2. \qquad 3\text{-}5$$

If $u \geq 0$, then the output is 1, else if $u < 0$, then the output is -1. Therefore, u is the decision boundary. This is graphically illustrated in the group scatter plot of **Figure 3.2(a)**, where the straight line $w_1 x_1 + w_2 x_2 - w_0 = 0$ is the decision boundary that separates class A from class B. Additionally, note that the bias term w_0 has the function of vertically adjusting the boundary decision, while the weights are responsible for adjusting the slope of the line. The Perceptron can be trained to "learn" this linear decision boundary, thereby establishing itself as a linear classifier. However, it has been demonstrated that the Perceptron can't solve nonlinear problems, such as the simple exclusive or (XOR) gate problem or a more complex problem requiring the abstraction of a nonlinear decision boundary, as illustrated in **Figure 3.2(b)** [110].

Figure 3.2 – Illustration of the decision boundary for two classes that are (a) linearly separable and (b) not linearly separable. The Perceptron, as a linear classifier, is only capable of classifying classes that are linearly separable.

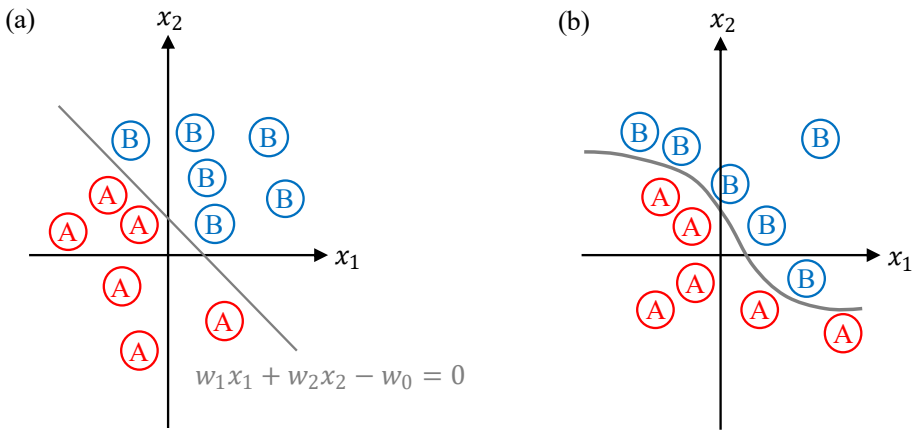

Source: Adapted from [109].

Before we proceed, it is important to define a more computational efficient way to perform the calculations in **Equation 3-1.** Consider we want to analyze k samples with n features. It is more convenient to define a matrix of features $x_{n+1\times k}$:

$$\mathbf{x} = \begin{bmatrix} -1 & -1 & \cdots & -1 \\ x_{2,1} & x_{2,2} & \cdots & x_{2,k} \\ x_{3,1} & x_{3,2} & \cdots & x_{3,k} \\ \vdots & \vdots & \ddots & \vdots \\ x_{n+1,1} & x_{n+1,2} & \cdots & x_{n+1,k} \end{bmatrix}, \tag{3-6}$$

where the element $x_{i+1,j}$ refers to the i-th feature of the j-th sample, and the first row is simply for the bias signaling. Similarly, we define a weight vector $w_{1\times \mathrm{n}+1}$:

$$\mathbf{w} = [w_0 \quad w_1 \quad w_2 \quad \cdots \quad w_n], \tag{3-7}$$

where the element w_0 is the bias and the element w_{i+1} is the i-th weight. Consequently, Equations **3-1** and **3-2** become a simple operation with matrices:

$$\mathbf{u} = \mathbf{wx}, \tag{3-8}$$

$$\mathbf{y} = f(\mathbf{u}), \tag{3-9}$$

where the output is now the vector $\mathbf{y}_{1\times k}$ with the element y_j being the predicted class for the j-th sample.

As discussed earlier, the training is performed by adjusting the weights and bias (vector **w**). However, this is not a trial-and-error process, the weights and bias are adjusted to minimize the errors in the model's predictions on the training data through an iterative optimization algorithm. The training consists in reading each one of the k training samples, predicting their class, comparing to their actual class, and then adjusting the vector **w** proportionally to the input features of that sample if the predicted and real class don't match. In summary, the training requires previous knowledge about the class of the samples, thereby the training of the

Perception is a supervised learning process. The algorithm sequentially predicts each one of the k training samples and adjusts the $\mathbf{w}$ vector at each of these iterations as follows [109]:

$$\mathbf{w} \leftarrow \mathbf{w} + \eta\left(d_j - y_j\right)\mathbf{x}_j^{\mathrm{T}}, \qquad 3\text{-}10$$

where $\mathbf{w}$ is the weight vector, d_j is the value assigned to the actual class of the j-th sample, y_j is value assigned to the predicted class of the j-th sample by the Perceptron, $\mathbf{x}_j^{\mathrm{T}}$ is the feature vector transposed for the j-th sample, and η is the learning rate. The parameter η is associated with how fast the Perceptron can learn, however, its value must be carefully chosen, as excessive high values may lead to training instability. Typical values of learning rate fall within the range $0 < \eta < 1$. In fact, **Equation 3-10** can be used even when the predicted class equals the real class of the sample, as in this condition $d_{\mathrm{j}} - \mathrm{y_j} = 0$ and the weight vector $\mathbf{w}$ will be updated with its own value, thus, not requiring to check whether $d_{\mathrm{j}} = \mathrm{y_j}$ is true or false. Once every test sample has been presented to the network and all the weights have been adjusted following **Equation 3-10**, a training "epoch" has elapsed.

The number of training epochs and learning rate is user-defined prior the training procedure. Additionally, it is a common practice to initialize the vector $\mathbf{w}$ with random small values instead of null values, letting the algorithm automatically adjust the values during training. Furthermore, it is highly recommended splitting the samples into two subsets, where the first subset is used exclusively to train the Perceptron, and the second subset is used to test and evaluate the performance of the trained model in predicting samples it has never seen before. Typical data split proportions are around 70% of the samples used for training and 30% used for testing.

3.2 THE MULTILAYER PERCEPTRON

The Multilayer Perceptron (MLP) is a network composed of multiple simple Perceptron units connected to each other, as illustrated in **Figure 3.3**. In this configuration, every circle illustrates a Perceptron model, where the weights block and activation function block have been

omitted to maintain visual clarity. Note that this architecture must have at least one hidden layer and an output layer, where the number of neurons may coincide or not. In this configuration the output of each neuron of a layer is connected to the input of each neuron of the subsequent layer. The MLP belongs to the feedforward architecture of neural networks because the information flow from the input layer to the output layer, without feedback [109]. In contrast to the simple Perceptron, the MLP offers the possibility of multiple outputs for multiple inputs, which makes the architecture rather versatile.

Figure 3.3 – The multilayer Perceptron architecture, where each circle represents a Perceptron. In this architecture, each output of a layer is connected to each input of the subsequent layer, making the information flow from the input layer to the output layer, a typical configuration of the feedforward network architecture.

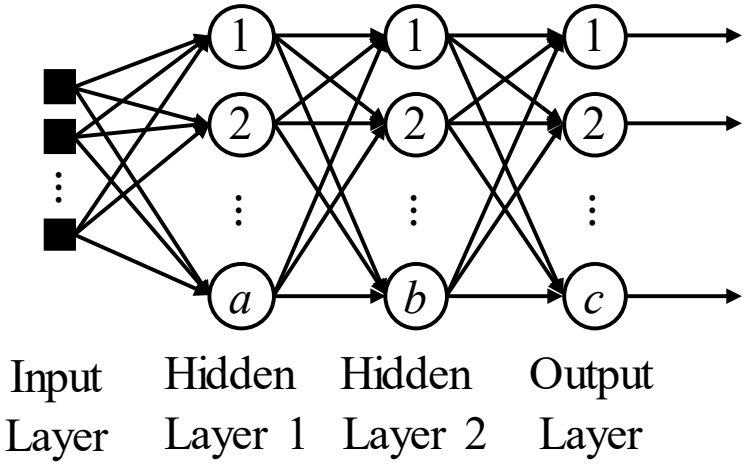

Source: Adapted from [109].

Before thinking about how to compute the output of the network based on the input, it is important to develop an expression that relates the output of a layer to its input. For that purpose, we consider two arbitrary fully connected layers of a MLP network, as illustrated in **Figure 3.4**. The goal is to compute the output vector $\mathbf{y}(L)$ of the layer L. The weight of the connection between the i-th neuron of the layer L and the j-th neuron of the layer $L-1$ is denoted $w_{i,j}(L)$. For the case of a MLP, $\mathbf{w}(L)$ is now a matrix holding the connection weights of every neuron of layer L, defined as:

$$\mathbf{w}(L) = \begin{bmatrix} w_{1,0}(L) & w_{1,1}(L) & w_{1,2}(L) & \dots & w_{1,n}(L) \\ w_{2,0}(L) & w_{2,1}(L) & w_{2,2}(L) & \dots & w_{2,n}(L) \\ \vdots & \vdots & \vdots & \ddots & \vdots \\ w_{m,0}(L) & w_{m,1}(L) & w_{m,2}(L) & \cdots & w_{m,n}(L) \end{bmatrix}, \quad \text{3-11}$$

where $w_{i,0}(L)$ is the bias of the i-th neuron of the layer L. We then define the net input of the layer L as $\mathbf{u}(L)$, where:

$$\mathbf{u}(L) = \mathbf{w}(L)\mathbf{y}(L-1), \quad \text{3-12}$$

Finally, the output vector of the layer L is computed by:

$$\mathbf{y}(L) = f\big(\mathbf{u}(L)\big), \quad \text{3-13}$$

where $f(.)$ is the activation function used for the neurons in the layer L. To compute the outputs of the network, it is necessary to begin applying the **Equation 3-13** from the first hidden layer, moving then to the subsequent layers until the output is reached. This is why this architecture is classified as a feedforward network.

Figure 3.4 – Connection between two arbitrary layers of a MLP network. The weight of each connection is illustrated near the connection line.

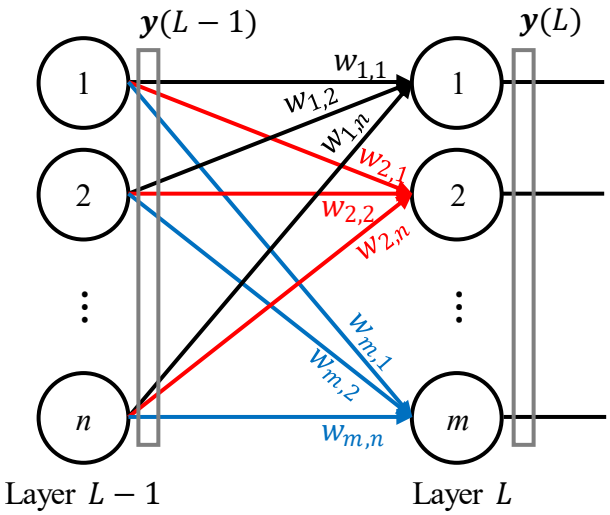

Source: Adapted from [109].

3.2.1 Activation functions

In contrast to the simple Perceptron, a MLP network have a broader range of possible activation functions to introduce non-linearities in the model, thus making it suitable for nonlinear problems. The most typical activation functions of a MLP network include the sigmoid function, hyperbolic tangent function, rectified linear unit (ReLU) and softmax function [111].

The sigmoid function maps the input values to a value between 0 and 1, making it suitable for tasks requiring probability information. It is defined as follows:

$$f(x) = \frac{1}{1 + e^{-x}}. \tag{3-14}$$

Furthermore, this function is differentiable and has a smooth gradient, which makes it suitable for network training based on gradient descent optimization algorithms, such as the backpropagation. However, the sigmoid function has a problem known as “vanishing gradient”, which can affect considerably the performance of deep neural networks (DNN - network with multiple hidden layers). In contrast, the hyperbolic tangent function maps the input values to a range between -1 and 1. The zero-centered behavior of the hyperbolic tangent function also improves the convergence of the network during training.

The ReLU activation function is widely used in many neural network architectures due to its simplicity and effectiveness. It is defined as:

$$\mathrm{ReLU}(x) = \max(0, x), \tag{3-15}$$

where $\max(0, x)$ returns the maximum value between 0 and x. In fact, the output of the function equals the input if $x > 0$, otherwise the output equals 0, thus rendering the “Rectified Linear” terminology. In contrast to the sigmoid and hyperbolic tangent, the ReLU function is not bounded to a range, being capable of outputting any positive number.

The softmax activation function is typically used in the output layer of multi-class artificial neural network classifiers. The number of output neurons of classifier models using softmax activation function is the same of the number of classes. The function converts a vector of raw scores (logits) into a vector of probabilities that represents the likelihood of the sample in belonging to each class. Mathematically, for an output layer O with n softmax neurons, every element y_i of the output vector $y(O)$ is computed based on every element u_j of the input vector $u(O)$ as follows:

$$softmax(y_i) = \frac{e^{u_i}}{\sum_{j=1}^{n} e^{u_j}}. \quad 3\text{-}16$$

As a result, the softmax layer outputs a probability distribution vector, and the classification is performed based on the class assigned to the neuron that exhibits the highest output.

3.2.2 Training of the MLP

The backpropagation is a training algorithm that utilizes the concept of gradient to find an adjustment in $w(L)$ that minimizes the output error. Before more details, it is important to define a metric of prediction error. Consider that a MLP network with m neurons in the output layer O is predicting the k-th sample of n training samples. The prediction error for the k-th sample is given by:

$$E(k) = \frac{1}{2}\sum_{i=1}^{m}\left[d_{i,k} - y_{i,k}(O)\right]^2, \quad 3\text{-}17$$

where $d_{i,k}$ is the desired value of the i-th output neuron for the k-th training sample, and $y_{i,k}(O)$ is the predicted value. The global performance is the mean value of the squared error obtained for each training sample, or simply mean squared error:

$$E_m = \frac{1}{n}\sum_{k=1}^{n} E(k). \qquad 3\text{-}18$$

The backpropagation algorithm begins adjusting the weights of the output layer, then the intermediate layers, and finally the first layer. Considering the output layer O, the algorithm finds the gradient of the error using the chain rule to adjust each element $w_{i,j}(O)$ of the output layer weights' vector $w(O)$, minimizing the output error. The gradient of the error is defined as [109]:

$$\nabla E = \frac{\partial E}{\partial w_{i,j}(O)} = \frac{\partial E}{\partial y_i(O)} \cdot \frac{\partial \mathrm{y_i(0)}}{\partial \mathrm{u}_i(0)} \cdot \frac{\partial u_i(O)}{\partial w_{i,j}(O)}, \qquad 3\text{-}19$$

where $y_i(O)$ is the output value of the i-th neuron and $\mathrm{u_j(0)}$ is the net input value of the i-th neuron. Additionally, from Equations **3-12** and **3-19**:

$$\frac{\partial u_i(O)}{\partial w_{i,j}(O)} = y_j(O-1). \qquad 3\text{-}20$$

And, from Equations **3-13** and **3-19**:

$$\frac{\partial \mathrm{y_i(0)}}{\partial \mathrm{u}_i(0)} = f'\big(u_i(L)\big). \qquad 3\text{-}21$$

Note that $f'\big(u_i(L)\big)$ is the derivative of the activation function, evaluated at $u_i(L)$. Furthermore, from Equations **3-17** and **3-19**:

$$\frac{\partial E}{\partial y_i(O)} = -[d_i - y_i(O)]. \quad \text{3-22}$$

Finally, replacing Equations **3-20**, **3-21** and **3-22** in Equation **3-19**:

$$\nabla E = \frac{\partial E}{\partial w_{i,j}(O)} = -[d_i - y_i(O)] \cdot f'\big(u_i(O)\big) \cdot y_j(O-1). \quad \text{3-23}$$

Then, we define the local gradient $\delta_i(O)$ related to the i-th neuron of layer O as:

$$\delta_{\mathrm{i}}(O) = [d_i - y_i(O)] \cdot f'\big(u_i(O)\big). \quad \text{3-24}$$

The adjustment of the element $w_{i,j}(O)$ needs to be in the opposite direction of the gradient to minimize the error:

$$\Delta w_{i,j}(O) = -\eta \nabla E, \quad \text{3-25}$$

where η is the parameter introduced to adjust the learning rate. Finally, the update in the value of $w_{i,j}(O)$ is performed by:

$$w_{i,j}(O) \leftarrow w_{i,j}(O) + \eta \cdot \delta_i(O) \cdot y_j(O-1). \quad \text{3-26}$$

Equation 3-26 shows how the weight $w_{i,j}(O)$ should be updated to minimize the error. Note that if the output of this neuron is in accordance with the expected output, then $d_i - y_i(O) = 0$ and the weight $w_{i,j}(O)$ will receive its own value (will not be updated).

It is important to highlight that **Equation 3-26** is only valid for updating the weights of the output layer, as it requires information regarding the expected output value. An inner layer L, however, do not have direct access to the network output. Therefore, the adjustment of their

weights is performed based on estimates of the output error produced in the subsequent layer $L+1$, whose weights have already been adjusted. A procedure similar to that used to derive **Equation 3-26** can be followed to find for the inner layers the following algorithmic weight update equation [109]:

$$w_{i,j}(L) \leftarrow w_{i,j}(L) + \eta \cdot \delta_i(L) \cdot y_j(L-1), \tag{3-27}$$

where the local gradient related to the *i*-th neuron of layer *L,* $\delta_i(L)$, is now defined by:

$$\delta_i(L) = -\left(\sum_{k=1}^{n_{L+1}} \delta_k(L+1) \cdot w_{k,i}(L+1) \right) \cdot f'\big(u_i(L)\big), \tag{3-28}$$

where n_{L+1} is the number of neurons of the layer $L+1$, $\delta_k(L+1)$ is the local gradient related to the *k*-th neuron of layer $L+1$, and $w_{k,i}(L+1)$ is the weight of the connection between the *i*-th neuron of the layer *L* and the *k*-th neuron of the layer $L+1$. Note that to compute the local gradient of one layer, it is necessary to have computed the local gradient of the subsequent layer. Finally, the algorithmic update equation for the weights of the first hidden layer can be derived similarly, resulting in [109]:

$$w_{i,j}(1) \leftarrow w_{i,j}(1) + \eta \cdot \delta_i(1) \cdot x_j, \tag{3-29}$$

where x_j is the *j*-th feature of the training sample and $\delta_i(1)$ can be computed by letting $L = 1$ in **Equation 3-28**.

In summary, for one training iteration of the network, first the network's response to the training sample needs to be computed. Subsequently, **Equation 3-26** needs to be applied for the output layer. Then, **Equation 3-27** needs to be applied for all the intermediate hidden layers, sequentially from the layer before the output to the second layer. Finally, **Equation 3-29** is applied to the first hidden layer. Due to its architectural complexity, the MLP requires a more

sophisticated training process, in contrast to the simple Perceptron. However, when performed correctly, the MLP is capable of executing complex tasks, such as image and speech recognition, function approximation and complex pattern abstraction.

3.3 PERFORMANCE METRICS OF MLP-BASED CLASSIFIERS

Artificial neural networks have a highly undesirable problem known as overfitting. The overfitting is a condition where the network is capable of accurately predicting the training samples but generates erroneous responses for samples it has never seen before. The capability of generalization is where lies the strength of the network. This capability is seriously compromised by an overfit condition, where the network can’t predict new information correctly. However, during training there are several ways of analyzing the performance of the network to identify possible overfitting conditions. This section explores two of the main performance metrics of MLP-based classifiers.

3.3.1 Accuracy and Confusion Matrix

The accuracy of an Artificial Neural Network (ANN) classifier is a performance metric that indicates the proportion of correctly predicted instances out of the total instances in the dataset. It provides an overall measure of the classifier's effectiveness. The dataset is typically divided into a training subset and a testing subset, often at proportions around 70-30. Consequently, there is an accuracy metric for the training subset and an accuracy metric for the testing subset. High accuracy in both subsets indicates a model with good generalization ability. Conversely, high accuracy in the training subset but poor accuracy in the testing subset usually suggests overfitting.

When the accuracy of both the training and testing subsets is not satisfactory, several measures can be taken to improve the model's performance. The most straightforward approach is to increase the number of training epochs. Additionally, testing different activation functions may yield better results. Experimenting with different numbers of neurons and varying the

number of hidden layers (i.e., changing the network architecture) is also a viable option. In fact, many parameters of the network can be adjusted to enhance accuracy. However, if these adjustments do not yield improvements, it may be necessary to carefully analyze the dataset for inconsistencies. Often, datasets require some level of preprocessing prior to training, depending on the nature of the data. For instance, if the dataset contains spectral data, performing spectral baseline correction with filters to remove background noise and distortions is a common practice [55], [112].

Although accuracy is a useful metric for assessing the performance of an MLP classifier, it is only a single number and may lack important information. For instance, in a multi-class problem, it is desirable to track how many correct predictions the network is making for each class and how many are incorrect. This detailed information is not adequately represented by a single accuracy value. The confusion matrix, as its name suggests, is a matrix that precisely represents the number of samples the network correctly predicts for each class. A graphical illustration of this matrix is presented in **Figure 3.5**. In this matrix, the rows represent the actual classes of the samples, while the columns represent the predicted classes. The numbers in a row show the distribution of predictions made by the network for the class assigned to that row. For instance, row 2 of the matrix refers to Class 2. In this row, column 1 shows how many samples of Class 2 were classified as Class 5. Similarly, columns 2, 3, 4, and 5 of row 2 represent the number of samples belonging to Class 2 that were classified by the model as Class 4, Class 3, Class 2, and Class 1, respectively.

From the confusion matrix presented in **Figure 3.5**, it is evident that the diagonal elements represent the correct predictions, while the off-diagonal elements correspond to misclassified samples. An effective model will exhibit values approaching 1 along the diagonal of its confusion matrix. The overall accuracy of the model can be computed by averaging the values on the diagonal. It is crucial to pay attention to the labels, as some authors may reverse the order of the classes or the rows and columns; however, the interpretation remains consistent for any confusion matrix. Unlike a simple accuracy metric, the confusion matrix is typically constructed based on test accuracy, as it provides significant insights into the classifier's overall performance.

Figure 3.5 – Graphical representation of a confusion matrix for a five-classes MLP classifier. The rows correspond to the actual classes and the columns represent the predicted classes. The numbers represent the percentage of classified samples.

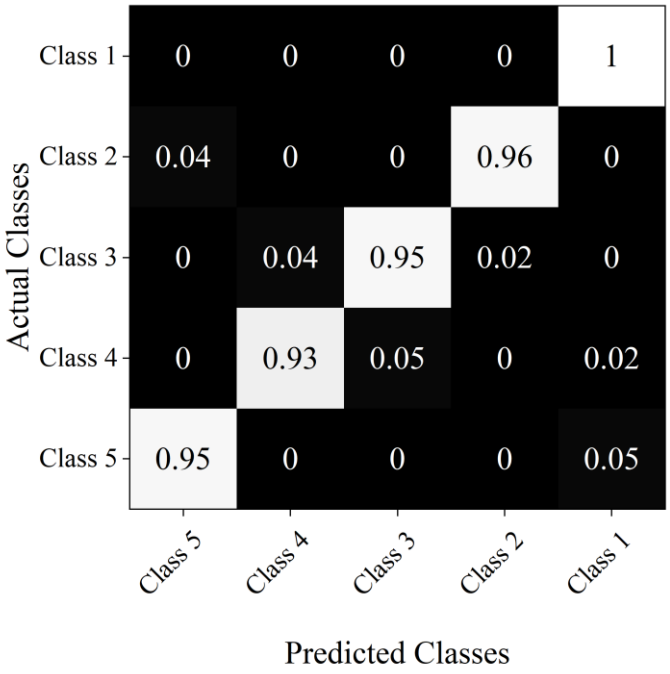

Source: Generated by the author.

3.3.2 Loss

The concept of loss is fundamental to understanding how effectively a model is performing a given task. Loss, also referred to as cost or error, quantifies the disparity between the predictions generated by the model and the actual ground truth values. It serves as a measure of how well the model is approximating the desired outcome. In essence, the goal of training a neural network is to minimize this loss function, thereby improving the model's ability to make accurate predictions.

Loss functions come in various forms, depending on the nature of the task. In regression tasks, where the objective is to predict continuous numeric values, mean squared error (which has already been introduced in **Equation 3-18**) is a common choice for the loss function. The mean squared error computes the average squared difference between the predicted values and

the actual ground truth values across all samples in the dataset. Minimizing MSE results in predictions that closely align with the true target values.

For classification tasks, where the goal is to assign input samples to predefined categories or classes, common loss functions include cross-entropy-based measures such as binary cross-entropy and categorical cross-entropy. These functions, in combination with a softmax output layer, compare the predicted class probabilities output by the model with the true class labels and penalize deviations from the correct predictions. In sparse categorical cross-entropy, the true class labels are integers, each indicating the index of the correct class for a given sample. The predicted probabilities generated by the softmax output layer of the model are compared to these integer labels, and the loss is computed based on the deviation between the predicted probabilities and the true class indices. Consider n training samples to be classified in c classes, where each class is represented by an integer j. The sparse categorical cross-entropy loss for the training samples is given by [113]:

$$scce = -\frac{1}{n}\sum_{i=1}^{n} log(y_{j,i}), \qquad 3\text{-}30$$

where log(.) is the natural logarithm and $y_{j,i}$ is the predicted probability that the sample i belongs to the class j.

3.4 IMPROVING THE PERFORMANCE OF A NEURAL NETWORK

Improving the performance of neural networks is important to achieve accurate and reliable predictions. Overfitting can significantly impact performance by reducing generalization to unseen data. Thus, ensuring a balance between model complexity and generalization capacity is crucial for preventing overfitting and enhancing accuracy. Higher accuracy not only enhances the credibility of predictions but also increases the practical utility of neural networks. Some techniques aimed at improving the models' accuracy and generalization capabilities can be employed for enhanced results.

3.4.1 Data normalization

Data normalization is a preprocessing technique used to rescale the features of a dataset to a similar scale without distorting differences in the range of values. The primary goal is to standardize the data distribution, making it easier for machine learning algorithms, particularly those sensitive to the scale of input features, to converge faster and perform better. Normalization ensures that features with larger scales do not dominate those with smaller scales during model training, thereby preventing biased results and improving the overall stability and efficiency of the learning process. The Z-score method is a process that normalizes all the observations of a feature in the dataset in such a way that the mean value becomes 0 and the standard deviation becomes 1. This is accomplished through the equation [114]:

$$v_i' = \frac{v_i - \overline{x}}{\sigma_x}, \tag{3-31}$$

where v_i' is the normalized value of the feature x the i-th sample, v_i is the actual value of the i-th sample, $\overline{x}$ is the mean value of feature x, and σ_x is the standard deviation of feature x.

3.4.2 Dropout

Dropout is a regularization technique commonly employed in neural networks to prevent overfitting and improve generalization performance. During training, dropout randomly deactivates a fraction of neurons in the network, effectively "dropping out" these neurons along with their corresponding connections. The neurons of each layer where dropout is being applied have a probability p (known as dropout rate) of being deactivated during a training iteration. By randomly removing neurons, dropout introduces noise and redundancy into the network, forcing it to learn more robust features and reducing excessive reliance on any specific set of neurons. This process encourages the network to learn multiple independent representations of the input data, making it more resilient to overfitting. During inference or testing, dropout is

typically turned off, and the full network with all neurons activated is used to make predictions. Overall, dropout is a powerful regularization technique that helps neural networks learn more robust and generalized representations of data, ultimately improving their performance on unseen examples [115].

3.4.3 K-fold cross-validation

K-fold cross-validation is a widely used technique for evaluating the performance of the models. The basic idea behind k-fold cross-validation is to partition the available dataset into k equally sized subsets or folds. Then, the model is trained k times, each time using k-1 folds for training and the remaining fold for validation. This process ensures that each data point is used for validation exactly once across all k training iterations. By averaging the performance metrics obtained from each k validation set, such as accuracy, confusion matrix or loss, k-fold cross-validation provides a more reliable estimate of the model's generalization performance compared to a single train-test split. It helps to mitigate issues related to dataset variability and ensures that the model's performance is consistent across different subsets of the data. K-fold cross-validation is particularly useful for assessing how well a model generalizes to unseen data. Overall, it is a robust and widely adopted technique for evaluating and improving the performance of artificial neural networks [116].

4. ADULTERANT DETECTION AND QUANTIFICATION APPROACH

In this work, we introduce a planar microwave resonator-based sensor to sense changes in the complex permittivity of extra virgin olive oil caused by adulteration, which in combination with a feedforward multilayer perceptron classifier and a set of first order polynomials is capable of identifying specific adulterants in EVOO and predict the proportion of the adulteration. With the proposed methodology, we investigate the adulteration of EVOO with soybean oil (EVOO-SO), corn oil (EVOO-CO), sunflower oil (EVOO-SU) and canola oil (EVOO-CA), the four most common adulterants of EVOO. An overview of the methodology presented in this work is illustrated in **Figure 4.1**.

Figure 4.1 – Overview of the proposed system for identifying and quantifying adulteration of EVOO with soybean oil, corn oil, sunflower oil or canola oil.

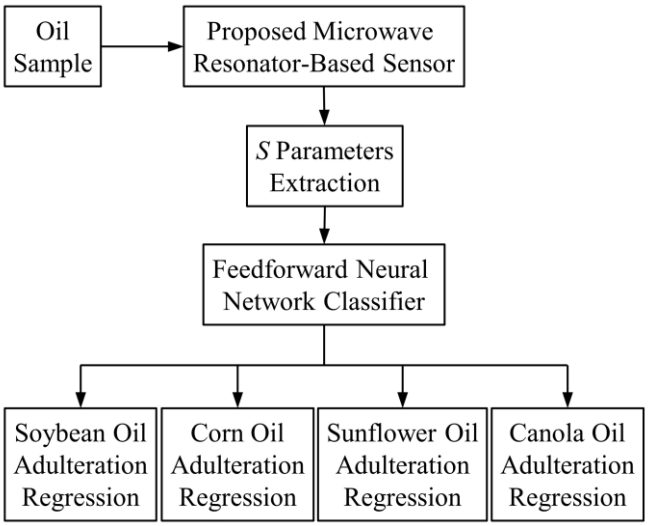

Source: [78]

4.1 PERMITTIVITY PROFILE OF EDIBLE OILS

Before delving into the details of our approach to identify and quantify adulterations in EVOO, we begin by conducting a study on the complex permittivity behavior of edible oils.

The complex permittivity of the five pure edible oils studied in this work (soybean, corn, sunflower, canola and EVOO) is extracted with an open-ended coaxial probe calibrated for the frequency range of 0.1 to 10 GHz, following the high-frequency alternative calibration method described in [117]. The probe simply consists of a 1 cm long coaxial transmission line attached to a SMA connector. The method requires measuring the complex reflection coefficient (S_{11}) of the probe, which we achieve by using a VNA (Rohde&Schwarz, ZVA 40). A picture of the experimental setup and probe is presented in **Figure 4.2**. To perform the calibration of the coaxial probe using the VNA, we first measure the complex reflection coefficient with the probe terminated in a short-circuit $\Gamma_{SC}(f)$. Subsequently, we measure the complex reflection coefficient of the open-ended coaxial probe $\Gamma_{OE}(f)$. Finally, we measure the complex reflection coefficient when the probe is submerged into distilled water $\Gamma_w(f)$. Then, we use these three curves to solve for the calibration constants $A_1(f)$, $A_2(f)$ and $A_3(f)$:

$$A_1(f) = \frac{\Gamma_{OE}(f) - \Gamma_{SC}(f) + [\Gamma_{SC}(f) - \Gamma_w(f)]\left[\varepsilon_w(f) - j\frac{\sigma_w}{2\pi f \varepsilon_0}\right]}{\Gamma_w(f) - \Gamma_{OE}(f)}, \tag{4-1}$$

$$A_2(f) = \frac{\Gamma_w(f)[\Gamma_{OE}(f) - \Gamma_{SC}(f)] + \Gamma_{OE}(f)[\Gamma_{SC}(f) - \Gamma_w(f)]\left[\varepsilon_w(f) - j\frac{\sigma_w}{2\pi f \varepsilon_0}\right]}{\Gamma_w(f) - \Gamma_{OE}(f)}, \tag{4-2}$$

$$A_3(f) = \Gamma_{SC}(f), \tag{4-3}$$

where $\varepsilon_0 = 8.85 \times 10^{-12}$ F/m is the free space electric permittivity, $\varepsilon_w(f)$ and σ_w are respectively the frequency dependent relative permittivity and DC conductivity of the distilled water. For the case of pure water, $\sigma_w = 0$. The value of $\varepsilon_w(f)$ is obtained through the superposition of two Debye calibration equations, provided in [117] as follows:

$$\varepsilon_w(f) = \frac{\varepsilon - \varepsilon_2}{1 + j2\pi f \tau_1} + \frac{\varepsilon_2 - \varepsilon_\infty}{1 + j2\pi f \tau_2} + \varepsilon_\infty, \tag{4-4}$$

where $\varepsilon = 78.32$, $\varepsilon_2 = 6.32$, $\varepsilon_\infty = 4.57$, $\tau_1 = 8.38$ ps and $\tau_2 = 1.1$ ps for a temperature of 25 ºC.

Figure 4.2 – (a) The experimental setup used to measure the complex $|S_{11}|$ when the probe is submerged into an oil sample for subsequent computation of the oil complex permittivity. Inset shows the probe in detail.

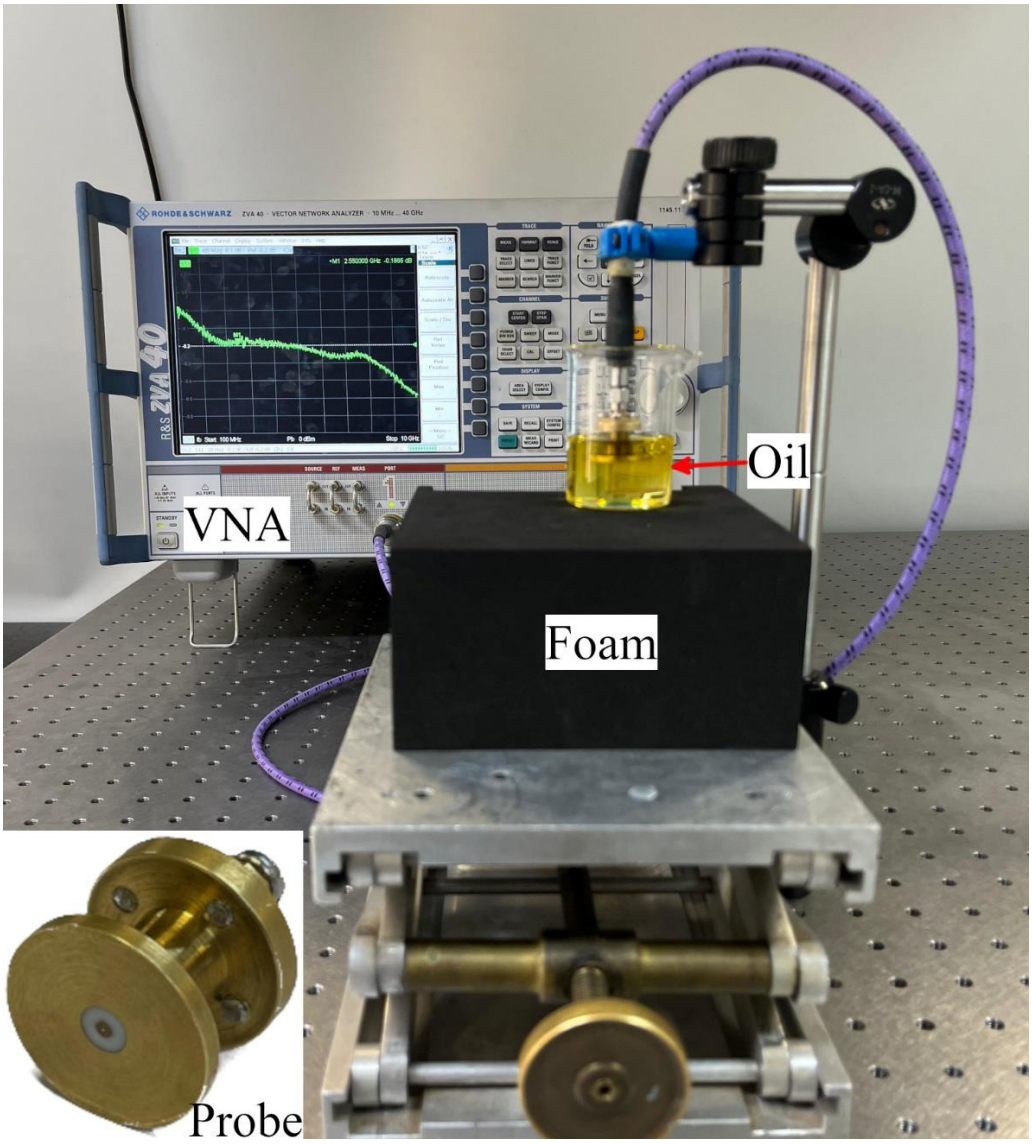

Source: [78].

Finally, we measure the complex reflection coefficient when the probe is submerged into each pure edible oil sample inside a beaker and compute the complex permittivity of the samples through:

$$\Gamma_n(f) = \frac{A_2(f) + A_3(f)\left[\varepsilon_n(f) - j\frac{\sigma_n}{2\pi f \varepsilon_0}\right]}{A_1(f) + \left[\varepsilon_n(f) - j\frac{\sigma_n}{2\pi f \varepsilon_0}\right]}, \qquad 4\text{-}5$$

where $\Gamma_n(f)$ is the reflection coefficient measured when the probe is submerged into the n-th pure oil sample, $\varepsilon_n(f) = \varepsilon'_n(f) - j\varepsilon''_n(f)$ is the frequency dependent relative permittivity and σ_n is the DC conductivity of the n-th oil sample. All measurements are conducted at a room temperature of 25.3 ºC. **Equation 4-5** must be solved for $\varepsilon_n(f) - j\frac{\sigma_n}{2\pi f\varepsilon_0}$. Note that it is not possible to separate the dielectric losses (ε''_n) and conductivity losses ($\frac{\sigma_n}{2\pi f\varepsilon_0}$), therefore we characterize the losses of edible oils in terms of their loss tangent $\tan\delta_n$ as follows:

$$\tan\delta_n = \frac{2\pi f\varepsilon_0\varepsilon''_n(f) + \sigma_n}{2\pi f\varepsilon_0\varepsilon'_n(f)} = \frac{\Im\mathfrak{m}\left[\varepsilon_n(f) - j\frac{\sigma_n}{2\pi f\varepsilon_0}\right]}{\Re\mathfrak{e}\left[\varepsilon_n(f) - j\frac{\sigma_n}{2\pi f\varepsilon_0}\right]}. \quad 4\text{-}6$$

In addition to the complex permittivity measurements, a Cole-Cole relaxation model is fit for each edible oil to describe the frequency dependency of the oil's complex permittivity through the equation [118]:

$$\varepsilon^*_{fit}(f) = \varepsilon_\infty + \frac{\varepsilon_s - \varepsilon_\infty}{1 + (j2\pi f\tau)^{1-\alpha}} + \frac{\sigma_s}{j2\pi f\varepsilon_0}, \quad 4\text{-}7$$

where ε_∞ is the permittivity at very high frequencies, ε_s is the static permittivity, τ is the relaxation time, α is the exponent parameter and σ_s is the static (DC) conductivity. In Matlab R2022b (MathWorks®) [119], the function *fminsearch* is used to find a combination of the parameters ε_∞, ε_s, τ, α and σ_s that minimizes the following error function, starting from an initial guess and achieving a local minimum:

$$err(f) = \sqrt{\Re\mathfrak{e}\left(\varepsilon^*_{fit}(f) - \varepsilon^*_{exp}(f)\right)^2 + \Im\mathfrak{m}\left(\varepsilon^*_{fit}(f) - \varepsilon^*_{exp}(f)\right)^2}, \quad 4\text{-}8$$

where $\varepsilon^*_{exp}(f)$ is the complex permittivity experimentally measured. The R^2 metric is used to evaluate the fitting for the real and imaginary components separately. The obtained parameters and R^2 are summarized in **Table 4.1** for each edible oil.

The results of measuring the reflection coefficients $\Gamma_{SC}(f)$, $\Gamma_{OE}(f)$ and $\Gamma_{w}(f)$ used for the calibration of the probe are illustrated in **Figure 4.3**. The experimentally measured complex permittivities of oils are illustrated in **Figure 4.4** along with their Cole-Cole model fittings. In **Figure 4.4(a)** are the calculated relative permittivity of the oils used in this study. Note that the relative permittivity of the EVOO is slightly lower than that of the other oils, which means that as we adulterate the EVOO with any of these oils, the resonance frequency of our sensor is expected to shift towards lower frequencies. This is exactly the result observed when measuring different adulteration levels with the proposed sensor. The experimentally measured $\tan\delta$ that incorporates both dielectric and conductive losses is illustrated in **Figure 4.4(c)**. The relative permittivity and the $\tan\delta$ obtained from fitting the Cole-Cole models are shown respectively in **Figure 4.4(b)** and **Figure 4.4(d)**.

Table 4.1 – Cole-Cole relaxation model fitting results for each edible oil.

	EVOO	**Soybean**	**Corn**	**Sunflower**	**Canola**
$\boldsymbol{\varepsilon_\infty}$	2.60	2.62	2.63	2.64	2.65
$\boldsymbol{\varepsilon_s}$	3.08	3.21	3.08	3.17	3.07
$\boldsymbol{\tau\ (\times 10^{-11}\ s)}$	7.00	8.98	7.03	7.98	6.15
$\boldsymbol{\alpha}$	0.26	0.29	0.16	0.25	0.16
$\boldsymbol{\sigma_s\ (\times 10^{-3} S/m)}$	2.65	1.74	2.56	2.13	2.50
R² real	0.965	0.962	0.956	0.956	0.956
R² imag	0.941	0.911	0.912	0.932	0.911

Source: [78].

Figure 4.3 – Measured $\Gamma_{SC}(f)$, $\Gamma_{OE}(f)$ and $\Gamma_{W}(f)$ used for the calibration of the probe from 0.1 to 10 GHz.

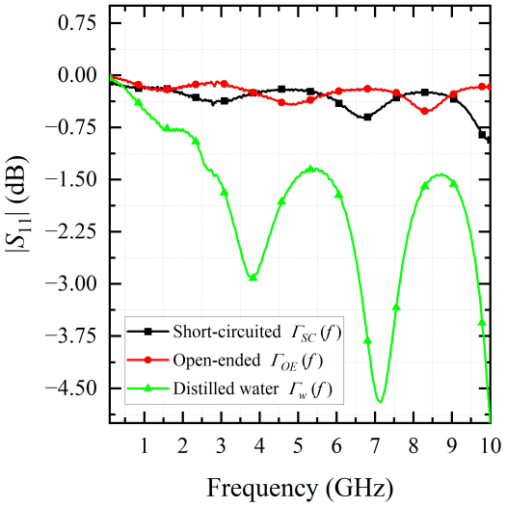

Source: [78].

Figure 4.4 – Results of applying the coaxial probe method to measure the complex permittivity of the five oils used in this study. (a) the experimentally measured frequency dependent relative permittivity of the edible oils and (b) the fitted relative permittivity using the Cole-Cole model. (c) the experimentally measured frequency dependent loss tangent and (d) the fitted loss tangent using the Cole-Cole model.

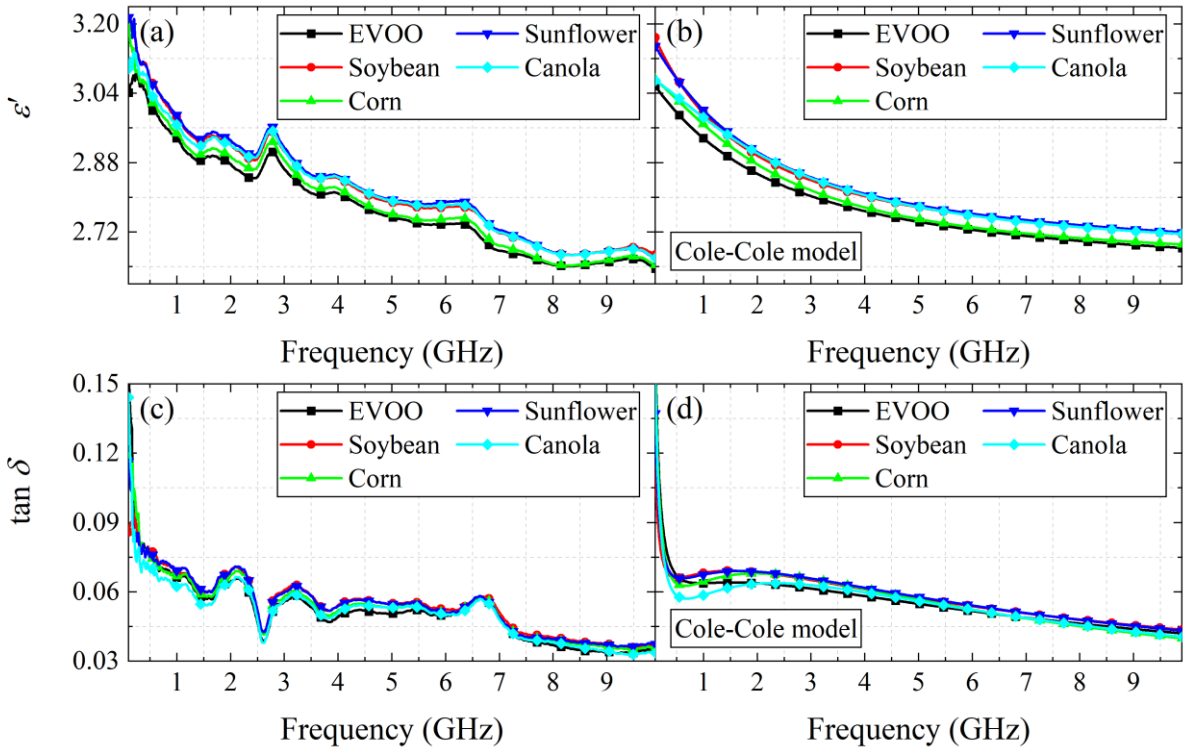

Source: [78].

There are some important observations to ensure the accuracy of this method of measuring the permittivity. First, the method is most suitable for liquid samples. Second, the coaxial probe must be cleaned immediately after each measurement to avoid changes in the dielectric material of the probe, which could compromise the calibration and next measurement. Third, the VNA cables need to be as static as possible, and if the probe is made of flexible material, it is important to avoid bending it as much as possible. Fourth, before each measurement, it is important to make sure that the current open-ended response of the probe is the same as that used for calibration. Fifth, every measurement should be performed with the probe as centered as possible, relative to the beaker, to avoid interference due to field interaction with the beaker's walls. Sixth, there is no need to submerge the probe completely. After some point, submerging more the probe will not cause the curve to change anymore. Finally, the measurements should be performed in an environment temperature as close as possible to 25 ºC for **Equation 4-4** to be valid.

4.2 SENSOR DESIGN AND FABRICATION

The proposed planar microwave resonator-based sensor comprises a spiral Spoof LSP resonator excited by microstrip transmission lines through electromagnetic coupling, as illustrated in **Figure 4.5**. The sensor is fabricated with a 35 µm thickness copper layer on top of a 1.6 mm thick FR4 substrate ($\varepsilon = 4.4 - j0.08$) with a 35 µm thick copper ground plane. We choose to adopt a planar geometry to enable convenient placement and measurement of oil samples inside a beaker, facilitating manipulation during experimentation. Moreover, these planar resonant structures based on spoof LSP exhibit high sensitivity to the complex permittivity of the surrounding media, while maintaining a subwavelength size and low-cost fabrication [96].

The design of the spiral resonator is shown in **Figure 4.6** along with the parametric equations used to create the spiral curve. It comprises four spirals rotated relative to each other by 90 degrees and electrically connected at the center of the resonator. The line width of the spirals is modeled by the parameter *slw*, while the parameters α, β and n adjust the effective length, number of turns, and maximum radius relative to the origin. The resonator is intentionally not electrically connected to the transmission lines in order to produce a band-pass frequency response in $|S_{21}|$.

Figure 4.5 – Proposed planar microwave resonator-base sensor featuring a spiral spoof LSP resonator electromagnetically coupled to microstrip transmission lines.

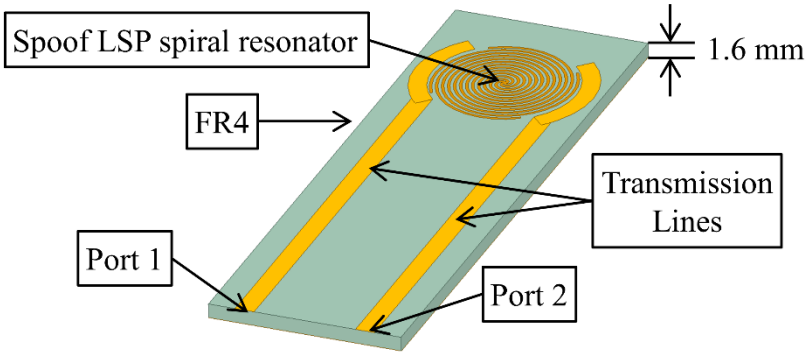

Source: Adapted from [78].

Figure 4.6 – The parametric design of the spiral used to build the resonator. Four of these single spirals are electrically connected at the center and rotated 90º relative to each other.

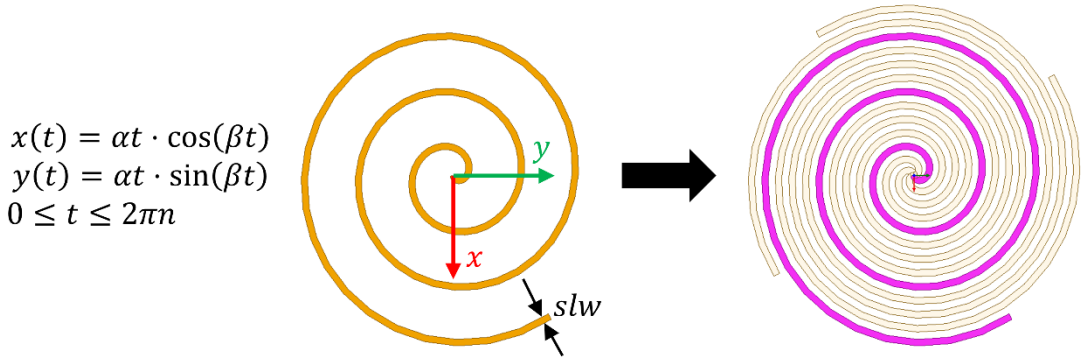

Source: [78].

The board and transmission line parametric variables are shown in **Figure 4.7**, where the board length *L* and width *W* are adjusted to accommodate the positioning of the sensor inside a beaker with inner diameter of 38.5 mm and a height of 60 mm containing 30 mL of oil sample. The parameters *tl_W*, θ and *r* are optimized to obtain strong coupling between the resonator and the transmission lines. The sensor is fabricated using the printed circuit board prototyping machine ProtoMat S103 (LPKF Laser & Electronics). **Figure 4.8** provides a picture of the sensor after it was fabricated, already with one SMA connector soldered in each transmission line. After fabricating and soldering the SMA connectors, a protective coating is applied to the board surface to prevent copper oxidation and changes in the dielectric properties of the FR4 substrate over time due to direct contact with the tested vegetable oils.

Figure 4.7 – Sensor board and transmission line parametric variables. Although very close, there is no electrical connection between the transmission lines and the resonator, which creates a band-pass frequency response in $|S_{21}|$.

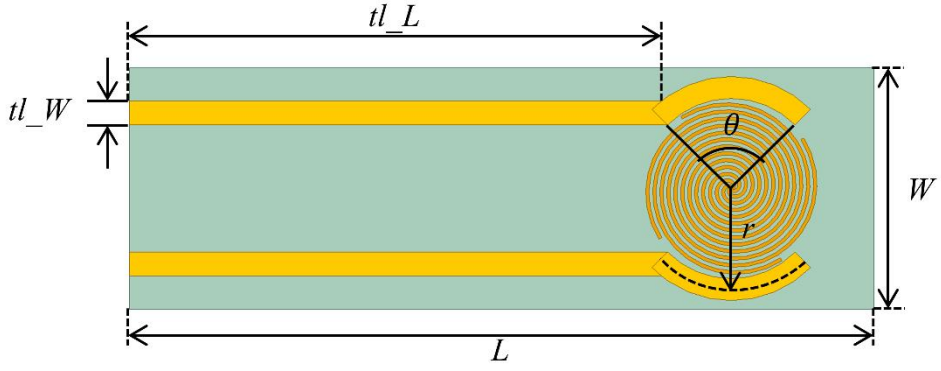

Source: [78].

Figure 4.8 – Proposed sensor fabricated using the board prototyping machine ProtoMat S103. Two SMA connectors are soldered, one in each transmission line, to provide connection with the VNA cables.

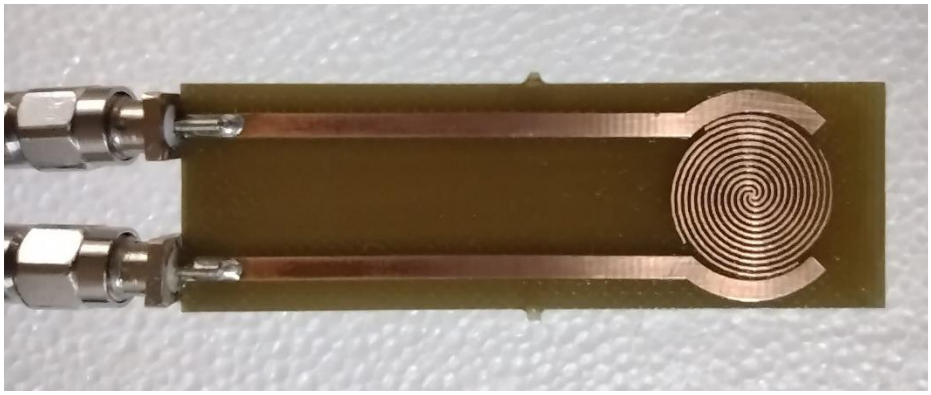

Source: [78].

The sensor's complex scattering parameters S_{11} and S_{21} are obtained by simulating the structure in the high-frequency structure finite element solver software ANSYS HFSS v2022 R2 [81]. The optimized geometrical parameters and their selected values are listed in **Table 4.2**, resulting from testing various combinations of all the structural parameters shown in **Figure 4.6** and **Figure 4.7** within the software environment to enhance the electromagnetic field around the resonator at its resonance frequency, while maintaining a reduced size and low resonance frequency. **Figure 4.9** illustrates some tested combinations of the resonator's structural parameters. It is noteworthy that the combination of parameters listed on **Table 4.2** may not produce the sharpest resonance; however, sharper resonances with higher Q were observed to have a lower signal level, which makes the sensor more susceptible to noise.

Table 4.2 – Proposed sensor's structural parameters optimized for field enhancement.

Parameter	Optimized value	Description
α	1.2 mm	Changes the effective length of spirals
β	2.95 mm	Changes the number of turns and effective length
n	1.05 mm	Changes the number of turns and effective length
slw	0.3 mm	Spiral line width
L	68.025 mm	Board length
W	22.05 mm	Board width
tl_L	49.17 mm	Transmission line length
tl_W	2.195 mm	Transmission line width
θ	90º	Circular transmission line angle
r	9 mm	Circular transmission line radius

Source: [78].

Figure 4.9 – Parametric sweep using all the values from **Table 4.2** but varying (a) α, (b) β, (c) n, and (d) slw.

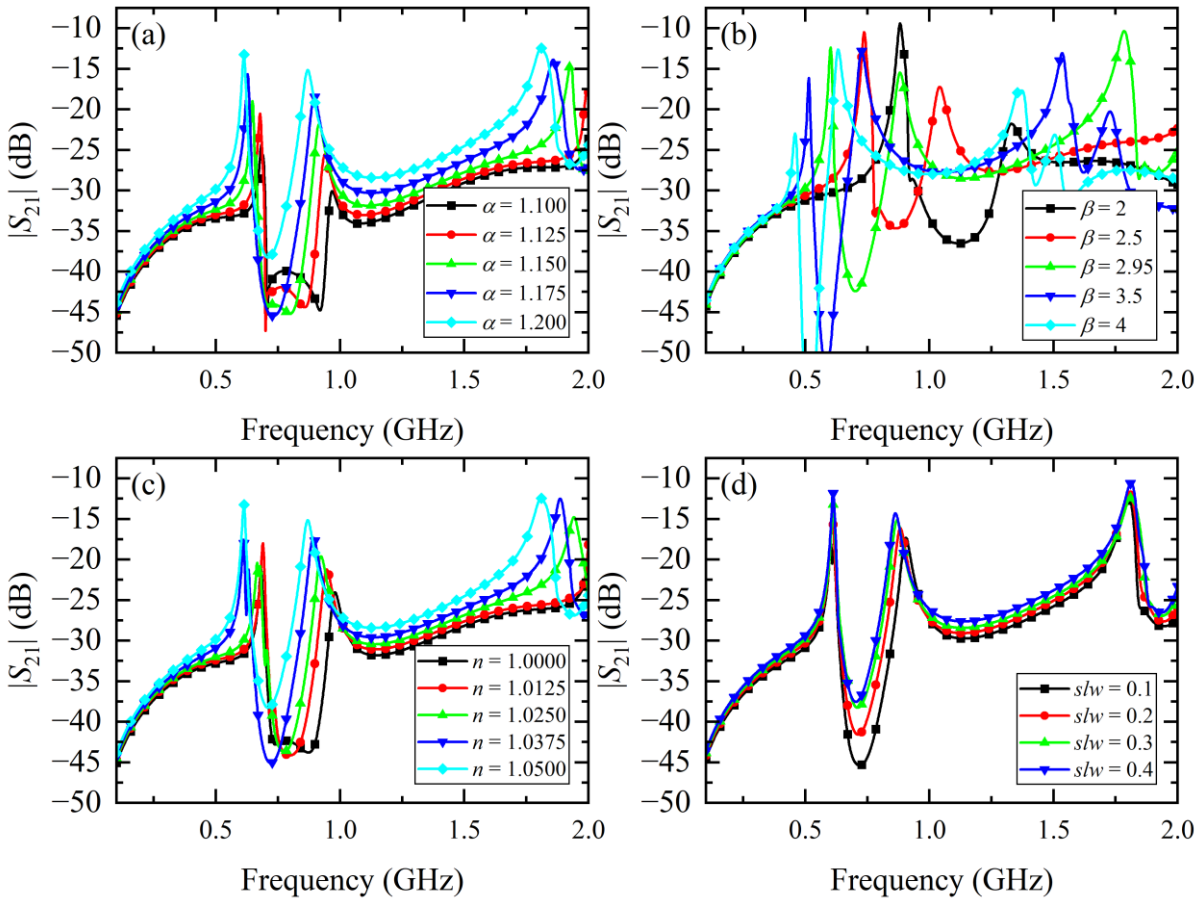

Source: Numerical simulations conducted by the author using HFSS.

The simulated $|S_{21}|$ of the structure with the parameters of **Table 4.2** is plotted in **Figure 4.10**, alongside the measured $|S_{21}|$ in situations with and without coating on the surface. It is noteworthy that the presence of a thin layer of coating barely alters the frequency response of the sensor, while providing additional protection. The considerable difference between the simulated and measured $|S_{21}|$ responses is mainly due to differences on the relative permittivity of the FR4 substrate, precision of the manufacturing process and soldering of the SMA connector. Additionally, we provide a measurement of a pure EVOO sample to illustrate the shift in the sensor's resonance frequency.

The simulated first resonance occurs at 601 MHz with a quality factor $Q \approx 48$, whereas the experimentally measured resonance for the sensor with coating occurs at 633 MHz with a quality factor $Q \approx 28$. The simulated electric field distribution at 601 MHz (the first resonance according to the simulated results) is shown in **Figure 4.10(b)**. The electric field is concentrated mainly in the spiral resonator region, which is a desirable outcome since the resonator will be

completely submerged in oil samples. With this field enhancement around the resonator, changes in the complex permittivity of the oil sample due to adulteration will cause variations in the sensor's complex S_{11} and S_{21} measured by the VNA, as well as alterations in the resonance frequency. Changes in the permittivity around the transmission lines have also been shown to contribute to the measurement of S_{11} and S_{21}. Our experimental setup is aimed at maintaining the oil level constant on the board to avoid errors introduced by different submersion levels at each measurement.

Figure 4.10 – Electromagnetic properties of the sensor with: (a) simulated and measured $|S_{21}|$ with slight differences between measured without coating and measured with coating, and measured EVOO. (b) simulated electric field distribution on the top surface of the sensor board without coating, at the simulated resonance frequency.

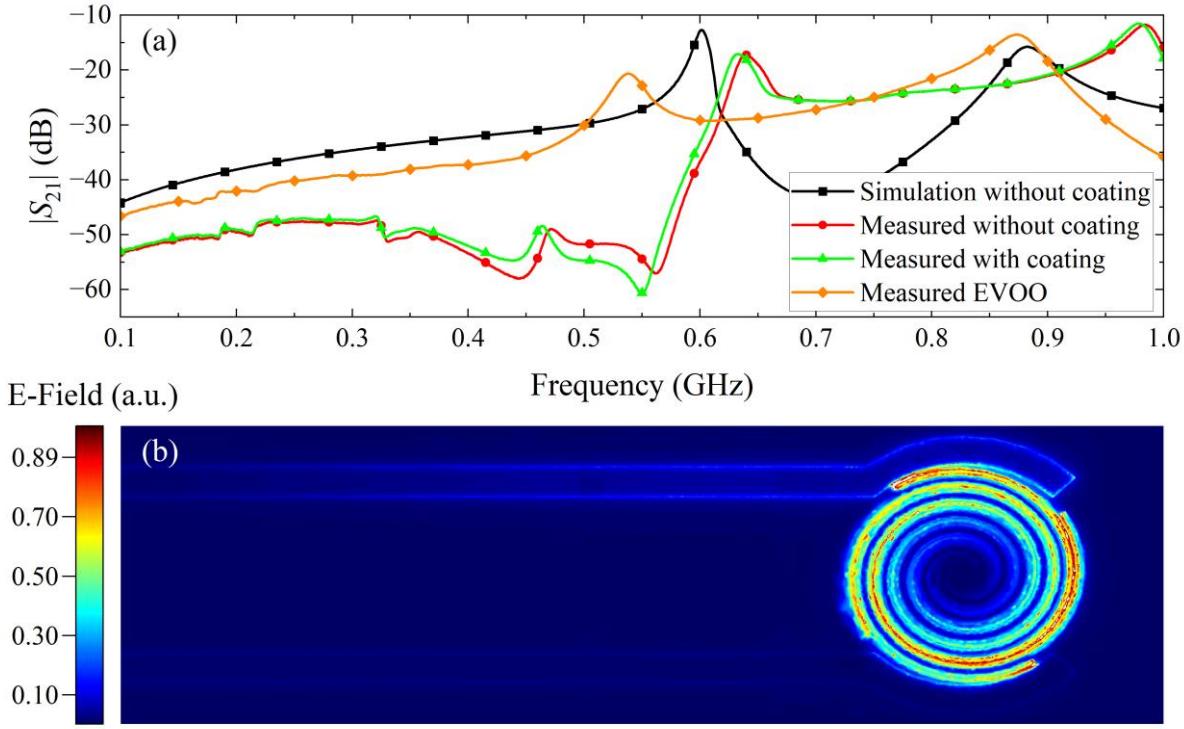

Source: [78].

4.3 EXPERIMENTAL DATA COLLECTION

The microwave sensor proposed in this work is designed to be immersed in a beaker containing 30 mL of oil sample. The measurement of the sensor's complex reflection coefficient (S_{11}) and transmission coefficient (S_{21}) is carried out using a VNA (Rohde&Schwarz, ZVA 40). To ensure accurate measurement of the sensor's scattering parameters, the VNA is calibrated using the two-port calibration kit ZV-Z54 (10 MHz to 40 GHz), spanning 201 frequency points from 520 MHz to 560 MHz. This frequency range encompasses the sensor's first resonance peak when it is submerged into a pure EVOO sample . The experimental setup is shown in **Figure 4.11**. A 3D-printed support is used to secure the sensor board and VNA cables, preventing interference caused by movement. Additionally, an adjustable-height metal platform is employed to precisely adjust the immersion of the resonator into the oil sample, ensuring that the oil level on the board is always the same for every measurement taken. A piece of foam is inserted between the platform and the beaker to create enough spacing and prevent any signal reflection on the platform surface.

Figure 4.11 – Experimental setup used to extract the sensor's complex S_{11} and S_{21} parameters under changes of the complex permittivity of oil samples due to adulteration.

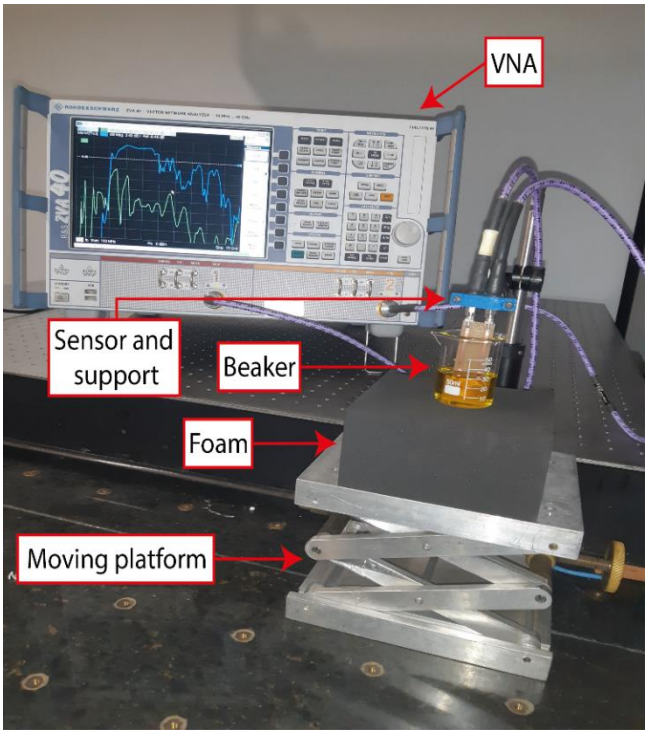

Source: [78].

In this study, we investigate the adulteration of EVOO with soybean oil (EVOO-SO), corn oil (EVOO-CO), sunflower oil (EVOO-SU) and canola oil (EVOO-CA). Adulterations ranging from 5% to 50% (mL/mL) with a 5% increment are prepared for each combination of EVOO-adulterant and measured five times to build a consistent database and ensure repeatability. For each adulterant, initially, 30 mL of pure EVOO is placed inside a beaker and measured five times with the sensor. Subsequently, a new adulteration is prepared within the same beaker. A volume V_r of sample is extracted from the beaker, and an equivalent volume of adulterant is added to increase the adulteration without altering the total volume of sample in the beaker. The volume V_r is calculated through:

$$V_r = \frac{(A_d - A_c) \cdot V}{1 - A_c}, \tag{4-9}$$

where A_d is the desired adulteration level, A_c is the current adulteration, and V is the volume of sample in the beaker. Additionally, we measure 5 times the sensor response to each pure adulterant. The resulting database consists of 5 measurements of four EVOO samples (all from the same bottle), and 5 measurements of each pure adulterant along with 50 measurements each of EVOO-SO, EVOO-CO, EVOO-SU, and EVOO-CA blends, totaling 240 measurements. The experimental procedures used for data collection are summarized in the flowchart of **Figure 4.12**. All measurements were conducted in a controlled environment with a temperature set at approximately 22° C, and a relative humidity maintained at around 40%. Moreover, the sensor was cleaned after each measurement using only water, soap, and a piece of tissue. Cleaning the sensor's surface with solvents such as isopropanol, removes the coating layer with the time.

The 240 measurements refer to the 12 adulteration levels (ranging from 0% to 100%) measured five times for each one of the four adulterants. **Figure 4.13** illustrates the measured $|S_{21}|$ curves for some adulteration levels of each adulterant incorporating error bars that are computed based on the five replicates of each adulteration level. The adulteration levels of 5%, 15%, 25%, 35% and 45% were omitted to maintain visual clarity in the figures. It is noteworthy that as the adulteration level of samples increase, the resonance frequency of the sensor decreases. Furthermore, the error bars do not overlap over a wide range of frequencies, which suggests the repeatability and reliability of the measurements performed by our sensor.

While many similar studies involving EVOO adulteration use multiple frequency components of the signal to detect adulteration, we demonstrate in this study that a single frequency component of the S_{21} signal provides us enough information to precisely detect adulterated EVOO samples. For that purpose, we define an alternative sensitivity metric to find the frequency at which the sensor is more sensitive to variations of adulteration level. The sensitivity S is defined as:

$$S(A_l) = \frac{d|S_{21}|}{dA_l}, \qquad 4\text{-}10$$

Figure 4.12 – Flowchart detailing every step of the experimental procedures used in the experimental data collection.

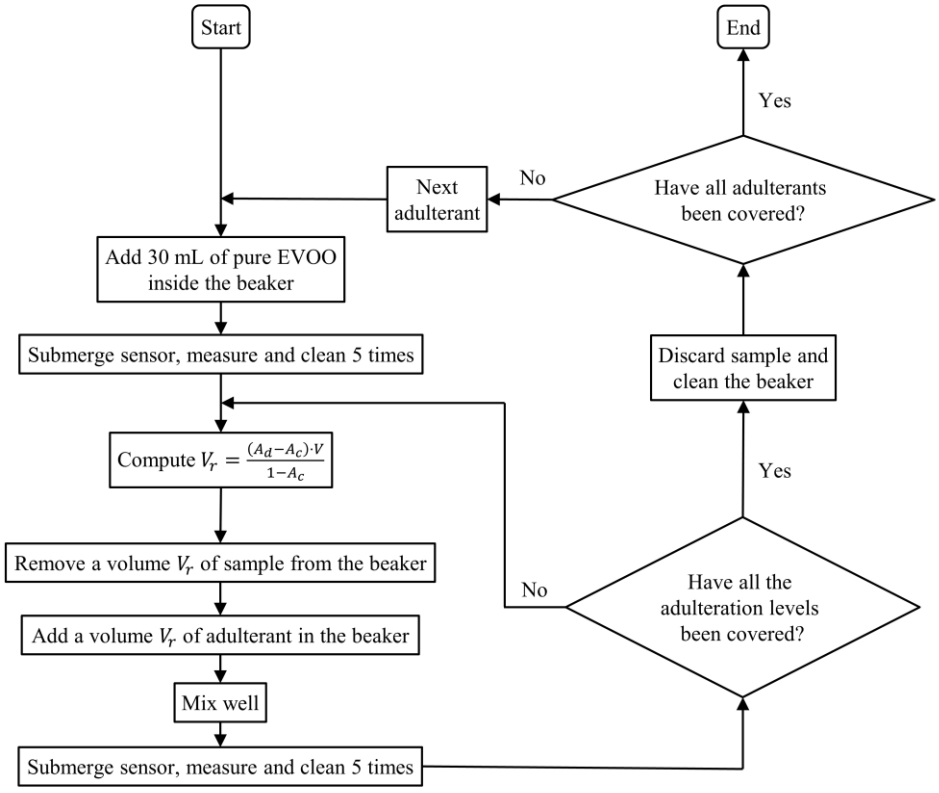

Source: Developed by the author.

where A_l is the percentile of adulteration (adulteration level). As the sensitivity is variable, we compute the mean value of it for each frequency point. The computed average sensitivity as function of the frequency is illustrated in **Figure 4.13** through the red dashed line for each

adulterant. The numerical values of sensitivity are represented in the red y-axis on the right side of each plot. From the sensitivity curves of **Figure 4.13**, we seek the frequency point with highest sensitivity where the error bars of the curves do not overlap. This point is illustrated in the figure by a green vertical dashed line at 546.8 MHz. Note from the figure that there are frequencies at which the sensitivity is higher, however the error bars at these frequencies do overlap for at least one adulterant. Therefore, we select the frequency of 546.8 MHz as the operating frequency of our sensor.

Figure 4.13 – Values of $|S_{21}|$ for some adulteration levels of each adulterant. The error bars suggest the high repeatability of the sensor. For every adulterant, the resonance frequency decreases as the adulteration level increases. The red dashed line is the sensor's average sensitivity, expressed in terms of dB/%adulteration, at each frequency. The sensitivity's axis in each plot is the red right y-axis.

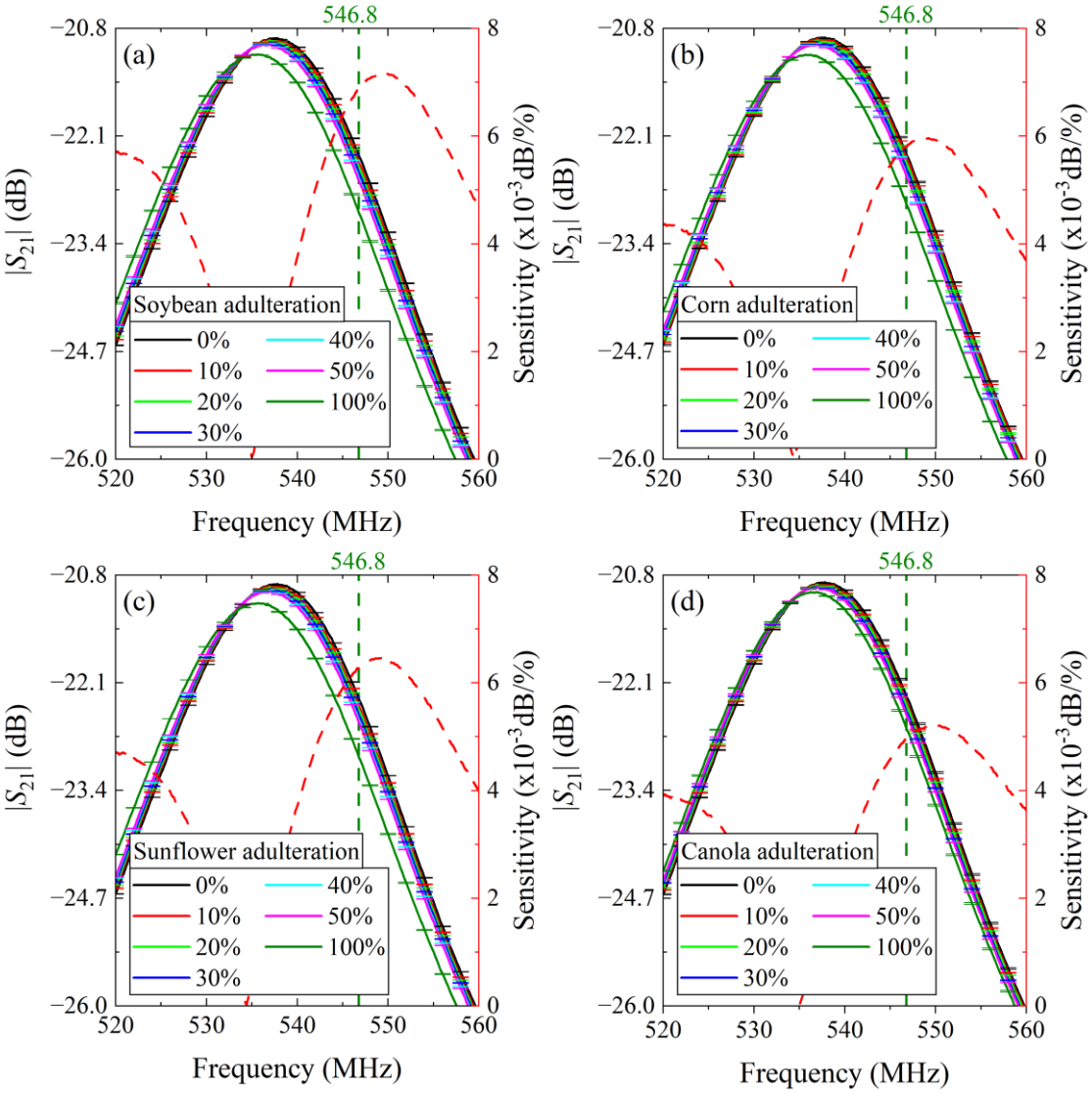

Source: [78].

After selecting the frequency of 546.8 MHz, we separate the 240 measurements at this frequency into five groups: EVOO, EVOO-SO, EVOO-CO, EVOO-SU and EVOO-CA. The measurements of pure adulterants are included in their respective EVOO-adulterant groups. Each measurement (observation/sample) has four real numbers (features), representing the real component of S_{11}, imaginary component of S_{11}, real component of S_{21} and imaginary component of S_{21}. Although two of the features represent imaginary components, they do not carry the imaginary unit j. With this dataset, the performance of two different feedforward neural networks acting as classifiers is evaluated and compared. The first neural network classifier uses only the real and imaginary components of the complex S_{21} as inputs, while the second neural network uses all four measured features. Additional machine learning techniques, such as z-score normalization, k-fold cross-validation, and dropout, are applied during the training of the models for performance improvement.

A linear relationship between the adulteration level and the quantity $|S_{21}|$ (in dB) is observed at 546.8 MHz for the four adulterants. Using this information, a distinct linear regression model is constructed for each adulterant through the partial least squares regression (PLSR) algorithm. This enables the quantification of the adulteration level immediately after identifying the specific adulterant in case the sample is adulterated. With the described methodology, it becomes feasible to identify adulterants in pure olive oil and quantify the adulteration using a low-cost microwave resonator-based sensor, simple neural network architectures, and straightforward mathematical models.

4.4 NEURAL NETWORK DESIGN AND TRAINING PROCEDURES

To assess the impact of the measured S_{11} data on classifying the samples, two ANNs are proposed as classifiers. The first classifier utilizes only the real and imaginary data of S_{21} (2 features), while the second classifier incorporates the real and imaginary data of both S_{11} and S_{21} (4 features). The goal of the classifiers is to categorize samples into the five previously mentioned groups: EVOO, EVOO-SO, EVOO-CO, EVOO-SU, and EVOO-CA.

Before training the classifiers, a simple data augmentation step is applied. Initially, the EVOO group had only 20 observations, while the other groups had 55 observations, resulting in an unbalanced dataset. The data augmentation step involves simply duplicating the

observations of EVOO to achieve 40 observations and, consequently, a more balanced dataset. Subsequently, a Z-score data normalization step is performed for the 4 features using **Equation 3-31**. Although simple, the implementation of these steps prior to training significantly improves the accuracy of both classifiers. The final dataset used for training the models consists of a total of 260 normalized observations and 4 features. The mean values and standard deviations obtained for the four features of all 260 observations are presented in **Table 4.3**.

Table 4.3 – Mean values and standard deviations for the four features, obtained from all 260 observations.

	Features			
	real(S_{11})	**imag(S_{11})**	**real(S_{21})**	**imag(S_{21})**
Mean value	-0.8327	-0.2495	-0.0656	0.0372
Standard deviation	0.0014	0.0026	0.0020	0.0005

Source: Developed by the author.

The neural network architectures used for the classifiers are illustrated in **Figure 4.14**. In **Figure 4.14(a)**, the first neural network utilizes only S_{21} data as inputs. It consists of 128 neurons ReLU activation function in the first layer (input) and a dropout rate $p = 0.5$, followed by another layer of 128 neurons with ReLU activation and a dropout rate $p = 0.5$, and finally, 5 neurons with softmax activation in the output layer. This network has a total of 17,541 trainable parameters, requiring a significant number of floating-point operations for predictions. In contrast, the model depicted in **Figure 4.14(b)** incorporates two additional inputs but features a considerably smaller number of neurons. It includes 32 input neurons with ReLU activation, a dropout layer with $p = 0.5$, and 5 output neurons with softmax activation, totaling only 325 trainable parameters and resulting in significantly fewer floating-point operations.

The softmax activation in the output layer provides a probability distribution over the five groups, ensuring that the sum of the outputs always equals 1. In this context, a higher output value of a neuron indicates a greater likelihood that the sample belongs to the group assigned to that neuron. Classification is performed based on the group assigned to the neuron with the highest output value. The use of dropout in layers with ReLU activation is a common regularization technique to prevent overfitting. During training, it randomly drops out (deactivates) some neurons of the layer with a probability p, known as dropout rate. During each iteration of training, the neurons with ReLU activation in our models have a probability

$p = 0.5$ of being deactivated in that specific iteration. This prevents the networks from becoming overly reliant on specific neurons. To train both models, we utilize the open-source deep learning framework Keras from the TensorFlow Python library [113]. The training process aims to minimize the sparse categorical cross-entropy loss between the true labels and the predicted probability distribution over the groups, while also enhancing the accuracy of the models.

Figure 4.14 – Architecture of the artificial neural network classifiers employed. (a) The 2-feature neural network, featuring an input layer with 128 ReLU neurons and dropout rate p = 0.5, an intermediate layer with 128 ReLU neurons and dropout rate p = 0.5, and an output layer with 5 softmax neurons. (b) The 4-feature neural network, featuring an input layer with 32 ReLU neurons and dropout rate p = 0.5, and an output layer with 5 softmax neurons.

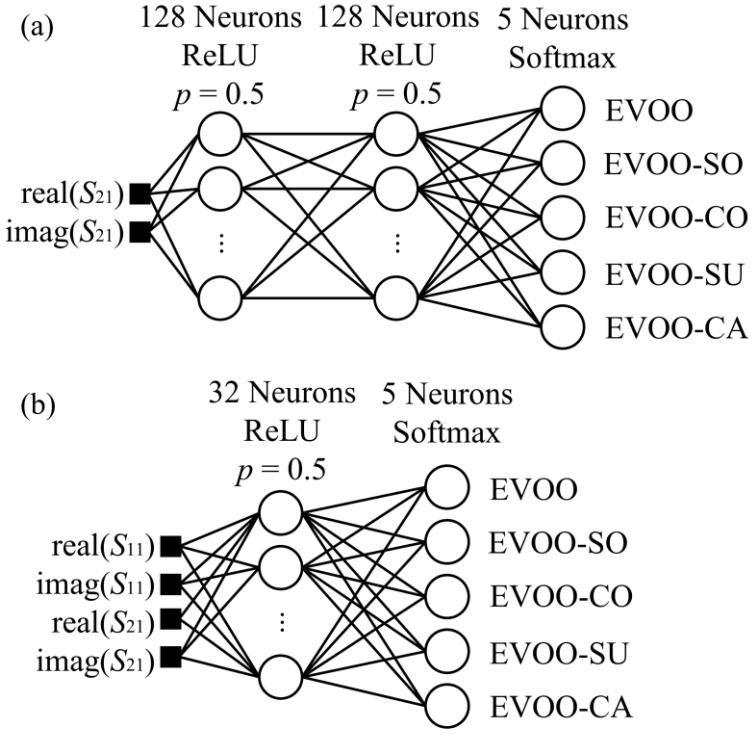

Source: [78].

During the training process, we employ the k-fold cross-validation technique with k = 5, dividing the final dataset into 5 non-overlapping subsets. Models are then trained and evaluated five times, with each iteration using a different subset for testing and the remaining four subsets for training. This application of k-fold cross-validation aims to assess the robustness and generalization performance of the models across different data subsets. Following each training iteration, a confusion matrix is constructed from the test subset

predictions. Ultimately, the mean confusion matrix is derived by averaging the confusion matrices from each fold. The same training procedures are applied to both the 2-feature and 4-feature models, using the same final dataset.

To choose the architecture of the models in **Figure 4.14**, we follow a simple procedure of testing different architectures. From the 260 normalized observations, we separate 156 (60%) for training and 104 (40%) for testing. We start training a network with a single neuron in the input layer for 100 epochs and evaluate its performance on the test samples using accuracy. If the accuracy is below 90%, we double the number of input neurons. This process is repeated until the test accuracy reaches 90% or the number of neurons reaches 1024. If 1024 neurons are reached without achieving 90% accuracy, we reset the number of input neurons to 1 and add a second hidden layer with 1 neuron. Each time the neuron count in layer n reaches 1024, we reset it to 1 and either double the neurons in layer $n + 1$ (if it exists) or create layer $n + 1$ with 1 neuron. **Table 4.4** summarizes this process by showing the number of neurons in each layer (except the output layer) for each iteration step. The 4-feature model achieves the 90% accuracy target at iteration 6, while the 2-feature model achieves it at iteration 96.

Table 4.4 – Number of neurons in each layer during each iteration step.

	Number of neurons	
Iteration	**Layer 1**	**Layer 2**
1	1	0
2	2	0
3	4	0
4	8	0
5	16	0
6	**32**	**0**
7	64	0
8	128	0
9	256	0
10	512	0
11	1024	0
12	1	1
13	2	1
14	4	1
...	...	...
22	1024	1
23	1	2
...	...	...
95	64	128
96	**128**	**128**

Source: [78].

Figure 4.15 illustrates the accuracy obtained for both models at each iteration until the 90% accuracy target is achieved. Please, note that this training procedure is only employed for selecting the model architecture (number of neurons and hidden layers). The selected architectures are then trained from scratch following the previously described training procedures.

Figure 4.15 – Test accuracy obtained by training models with different numbers of neurons and layers for 100 epochs. The 4-feature model achieves the 90% accuracy target at iteration 6, featuring an architecture with an input layer of 32 neurons and an output layer of 5 neurons. Conversely, the 2-feature model reaches the 90% accuracy target at iteration 96. Its architecture comprises an input layer with 128 neurons, a hidden layer with 128 neurons, and an output layer with 5 neurons.

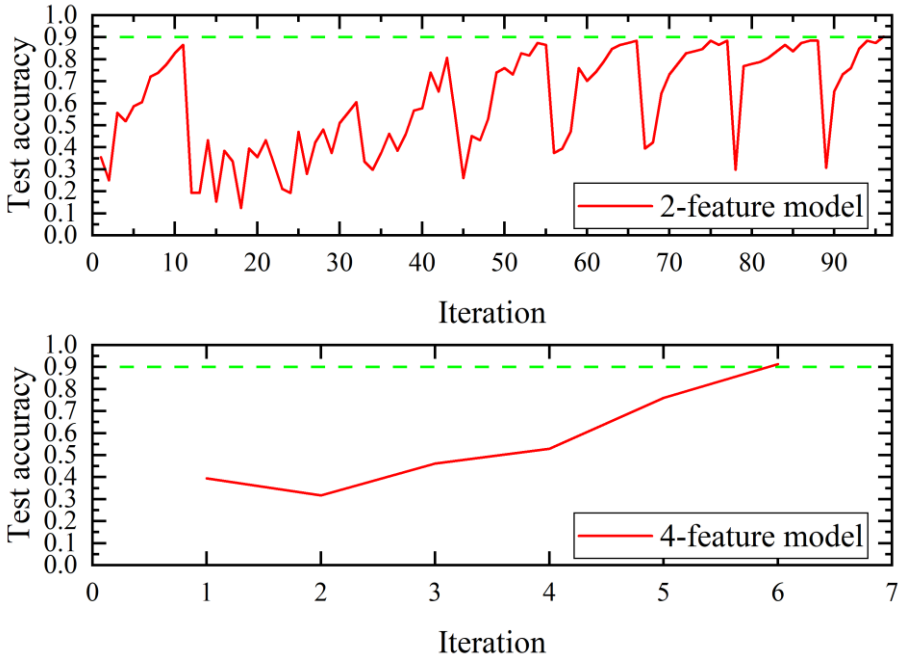

Source:[78]

5. RESULTS AND DISCUSSION

The sensor performance is evaluated at the operating frequency of 546.8 MHz. To illustrate how the sensor behaves at the operating frequency as the adulteration of a EVOO sample increase, consider the **Figure 5.1**. Note that the relationship between $|S_{21}|$ and the adulteration level is nearly linear for the four adulterants considered in this work. This is an important result, as the sensor's linearity at this frequency holds for the entire adulteration range, making it very easy to predict the adulteration levels based on the measured value of $|S_{21}|$. Also note that the error bars are very small and there is no ambiguity between different adulteration levels, which suggests once more that the proposed sensor has good repeatability.

Figure 5.1 – Experimental results obtained from measuring $|S_{21}|$ at 546.8 MHz, with a varying adulteration level, for all 4 adulterants studied in this work. Error bars are plotted considering the standard deviation between the five replicates of each adulteration level. A linear relationship between the adulteration level and $|S_{21}|$ is observed for all adulterants.

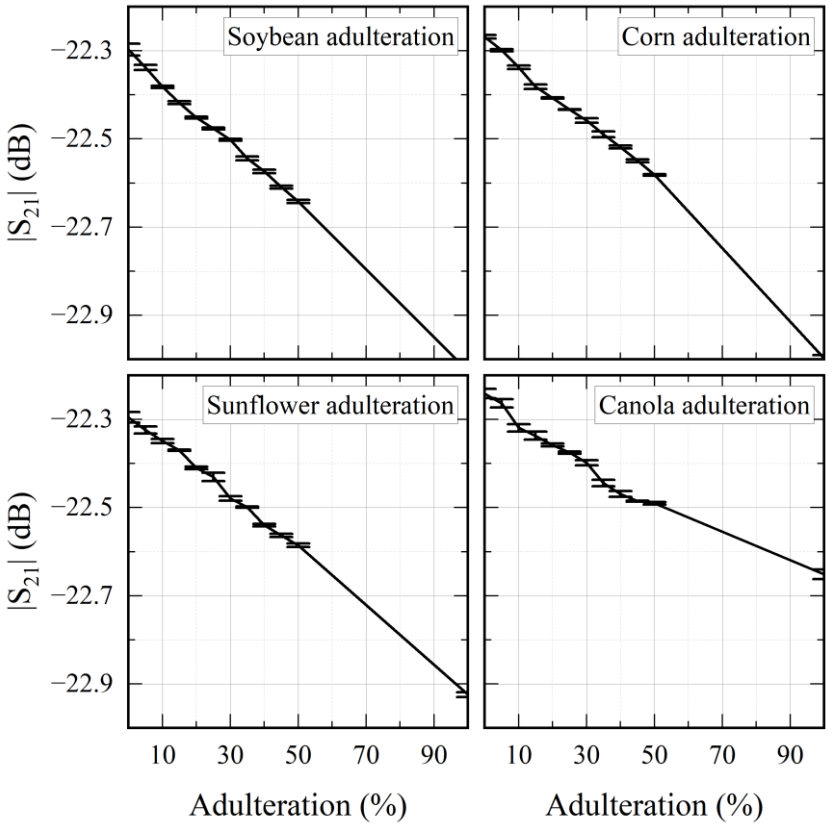

Source: [78].

The average sensitivity derived from **Figure 5.1**, expressed as dB per percentile of adulteration, for the adulterations with soybean, corn, sunflower and canola oils are respectively 0.007 dB/%, 0.0059 dB/%, 0.0065 dB/% and 0.0048 dB/%. These values are proportional to the slopes of the adulteration curves, which in turn are a direct consequence of the difference in relative permittivity between EVOO and the adulterated sample. It is crucial to note that a unique linear expression can correlate the adulteration level with $|S_{21}|$ for each known adulterant with reasonable precision. However, simply examining **Figure 5.1** based solely on the transmission coefficient module does not enable the identification of both the adulterant and the adulteration level.

Another method of visualizing the sensor-obtained data is through the group scatter plot shown in **Figure 5.2**. The 240 measurements are plotted and categorized into their respective adulterant groups using the data collected from the VNA without any preprocessing. In contrast to **Figure 5.1**, this alternative visualization provides more detailed information regarding group classification for the same data. The data points in the bottom-left corner correspond to pure olive oil or slightly adulterated samples. As the degree of adulteration increases, the data points gradually shift towards the top-right corner, each with different slopes for specific adulterants. From **Figure 5.2**, it is possible to delineate regions corresponding to specific adulterant groups, a task efficiently performed by training the 2-feature ANN classifier.

To visualize the high-dimensional data consisting of 240 observations and 4 features, we apply the Principal Component Analysis (PCA) algorithm. PCA applies a linear transformation on the data represented in an n-dimensional vector space to convert it into an n-dimensional orthogonal principal component space. In this new space, the first principal components capture the majority of the data's variation. This algorithm is useful because, in many cases, it is possible to represent the data adequately using only the first few principal components, often the first two, while ignoring the others. By projecting our four-dimensional data onto a set of two principal components (PCs), we capture and explain 97.68% of the total variance in our data. This dimensionality reduction provides a clear and concise representation of the data. The results of PCA are summarized in the biplot presented in **Figure 5.3**. In the referred figure, it is possible to identify slightly different patterns for each adulterant, but the groups overlap at some points, suggesting similarities between different adulteration levels across the groups. Despite these similarities, we show later that the 4-feature ANN classifier is capable of abstracting the four-dimensional data and efficiently distinguishing the groups. It is important to highlight that the PCA conducted herein is solely to provide an effective way of

visualizing the four-dimensional data collected. The principal components obtained are not used for training the ANN classifiers. With the data of **Figure 5.2** and **Figure 5.3** carrying the adulterant groups information and the data of **Figure 5.1** carrying the adulteration levels information, we construct the solution set for the problem of identifying and quantifying adulteration in EVOO.

Figure 5.2 – Group scatter plot of the 240 measurements taken at 546.8 MHz. Each data point on the plot represents a measurement. The x-axis corresponds to the real component of S_{21} extracted directly from the VNA without any preprocessing, while the y-axis corresponds to the imaginary part.

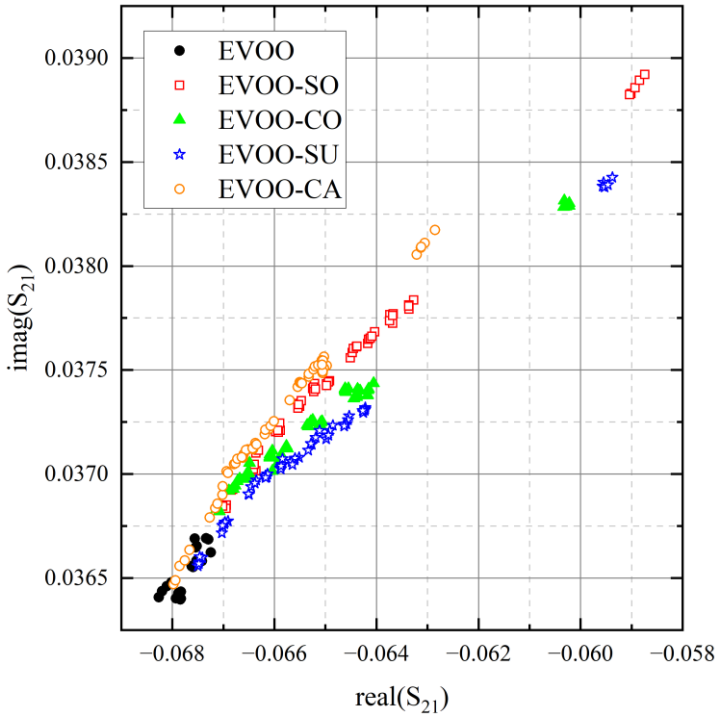

Source: [78].

Figure 5.3 – Results of the PCA conducted on the 240 four-dimensional observations. The first 2 principal components explain together 97.68% of the total variance in the data. No additional data pretreatment is applied before PCA. The vectors illustrate how the actual 4 variables correlate with the 2 principal components.

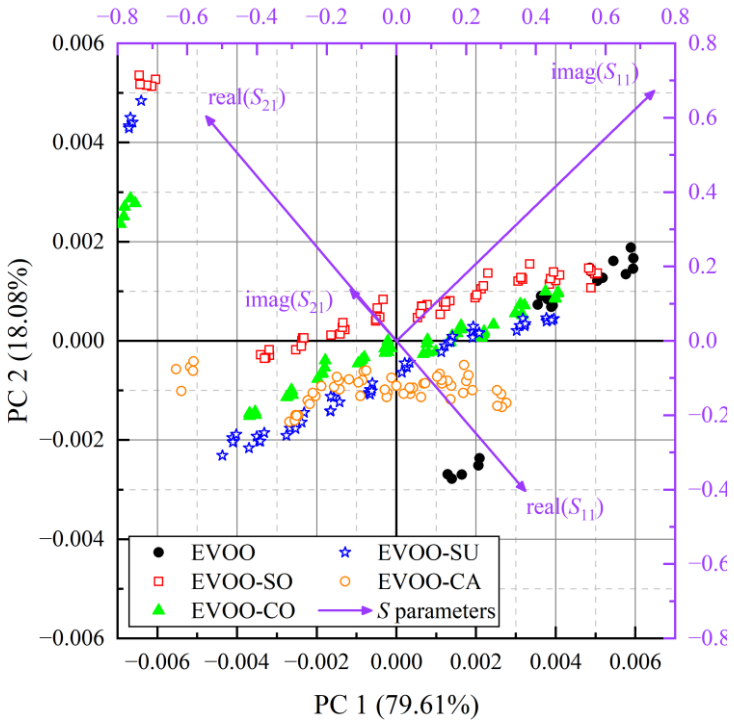

Source: [78].

5.1 PERFORMANCE OF THE 2-FEATURE ANN CLASSIFIER

The results of training the 2-feature ANN classifier are presented in **Figure 5.4** in terms of its average confusion matrix. Referring to the figure, the 2-feature model could predict correctly 89% of EVOO-CA samples, while 9% of samples were predicted as pure EVOO and 2% of samples were predicted as EVOO-CO. Furthermore, the model was able to classify correctly 92% of EVOO-SU samples, while the remaining were classified as EVOO (4%) and EVOO-CO (4%). In the case of the EVOO-CO group, 89% of the samples were correctly classified, with the remaining being misclassified as either EVOO-SO (7%) or EVOO-SU (4%). For the EVOO-SO group, 89% of the samples were correctly classified, while the remaining 11% were misclassified as EVOO-CO. Finally, the model was able to correctly classify 98% of the pure EVOO samples, while the remaining 2% were classified as EVOO-SU.

Figure 5.4 – Confusion matrix of the trained 2-feature model, obtained by averaging the confusion matrices of each test step of *k*-fold cross-validation. The areas highlighted with a blue diagonal pattern represent false-positives for adulteration, while the areas highlighted with a red squared pattern represent false-negatives.

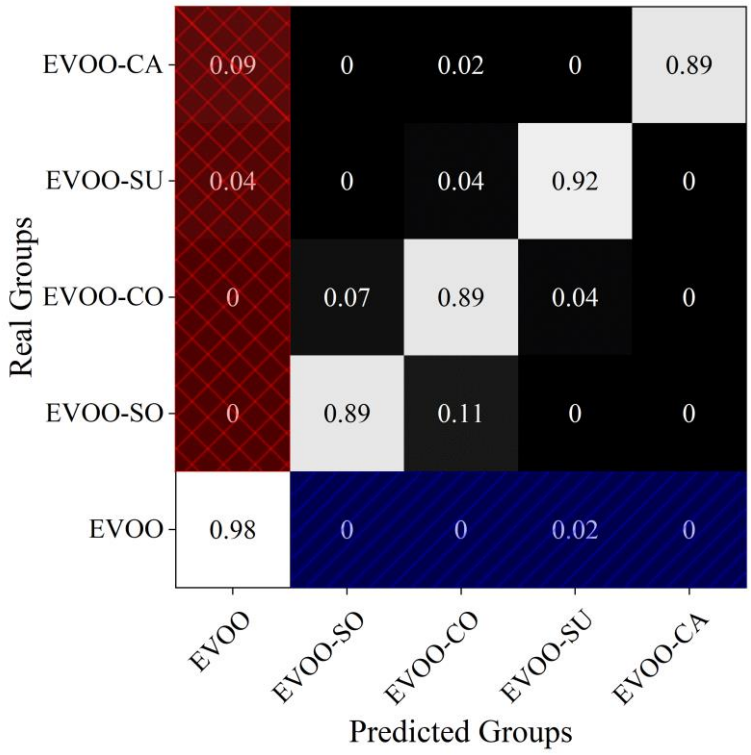

Source: Adapted from [78].

The overall accuracy of the 2-feature model was 91.4%, obtained by averaging the counter-diagonal of the matrix in **Figure 5.4**. While an overall accuracy of 91.4% indicates good predicting capabilities, the confusion matrix raises concerns about false-positives (with 2% of EVOO samples being misclassified as EVOO-SU) and false-negatives (with 9% of EVOO-CA and 4% of EVOO-SU samples being misclassified as EVOO) when dealing with binary classification, i.e., adulterated or not adulterated samples. In the matrix, the blue diagonal pattern refers to the false-positive results, while the red squared pattern refers to the false-negative results. Even though this model features a hidden layer, its architecture is rather simple, which makes it possible to implement it in microcontroller circuits to obtain real-time classification of oil samples. For instance, when implemented on a low-cost ESP32-S board, the 2-feature model takes approximately 124 ms to predict all 260 samples (an average of 477 µs per sample), requiring at least 68.52 kB of RAM (random access memory) to store the neurons' weights and biases as 4-byte floating-point values.

From the confusion matrix of the 2-feature ANN model, it is evident that the model indeed learned crucial patterns that help classifying the samples. This abstract pattern information is stored in the model's weights, which do not offer us a good visual representation of what the model actually learns. Therefore, for better illustrating what the model learned, we discretize the 2D space of **Figure 5.2** into 2835x2835 points, yielding 8,037,225 observations. We normalize these observations with the data of **Table 4.3** and predict all observations with the 2-feature model. The result is illustrated in **Figure 5.5**. This is an interesting approach to visualize the decision boundaries learned by the model.

Figure 5.5 – Pattern learned by the 2-feature ANN model. The nonlinear nature of the five decision boundaries is evident in the figure, however the model has a powerful capability of abstraction, and most of the samples are correctly classified.

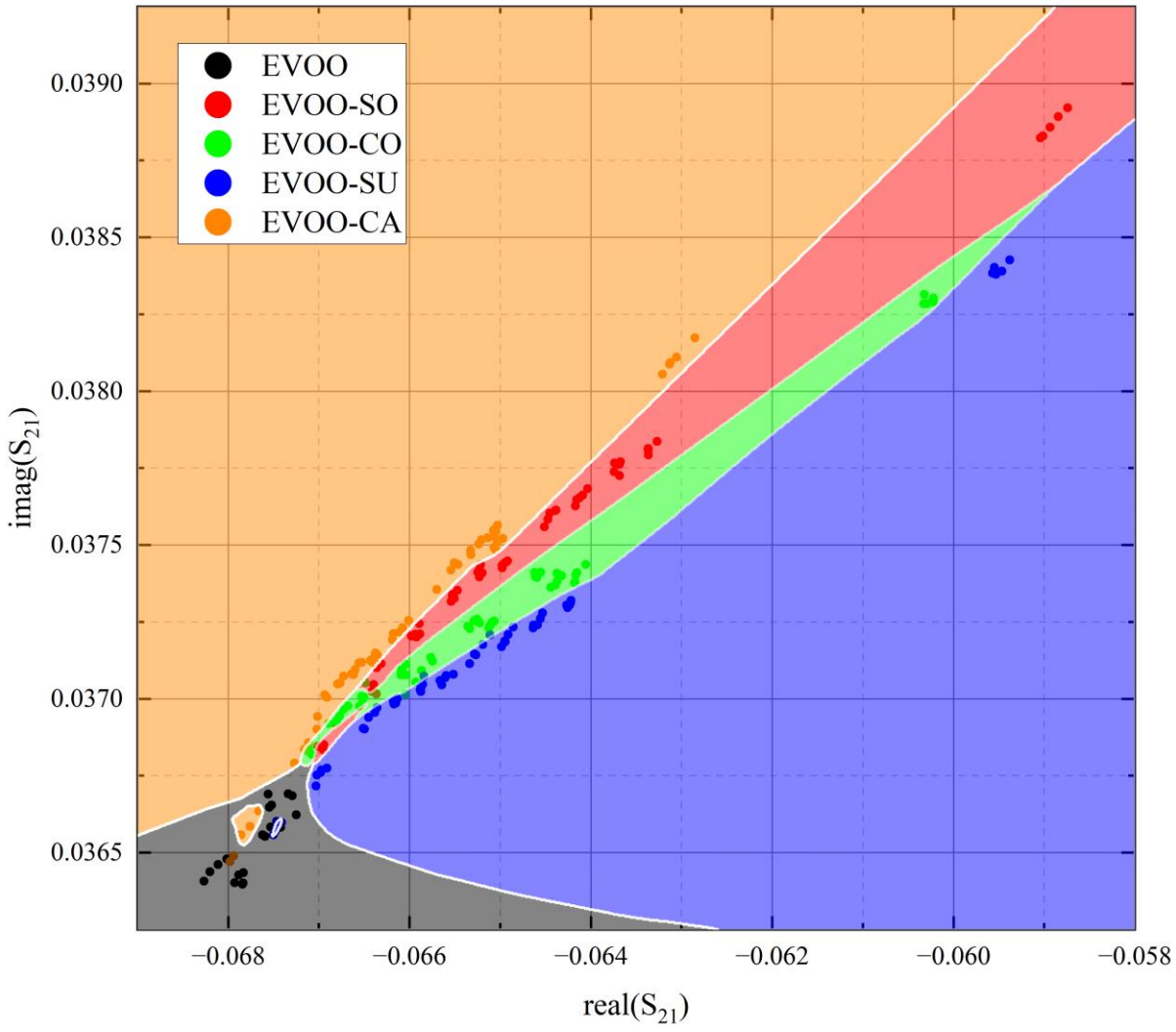

Source: Developed by the author.

5.2 PERFORMANCE OF THE 4-FEATURE ANN CLASSIFIER

The initial idea was to train a classifier using only the real and imaginary components of S_{21}. However, additional benefits are observed when incorporating the real and imaginary components of S_{11} as well. The first noticeable enhancement can be seen in **Figure 4.14**, where the number of neurons required for the 4-feature model significantly decreased compared to the 2-feature model, resulting in a simpler and faster model. This relative simplicity, however, does not imply a reduction in accuracy for the model. Note from the confusion matrix of **Figure 5.6** that the 4-feature model achieves 100% accuracy in predicting all the test samples for the EVOO-CA, EVOO-SO and EVOO groups. Meanwhile, 2% of the EVOO-SU samples were misclassified as EVOO-CO, and 2% of the EVOO-CO samples were misclassified as EVOO-SU. Despite this minor confusion, it is observed that the 4-feature model do not present any false-positive (refer to the blue diagonal pattern of the figure) or false-negative (refer to the red squared pattern of the figure) results, which suggests the suitability of the model for binary classification. The 4-feature model achieved an overall accuracy of 99.2% in predicting the test samples. Additionally, this model is faster than the 2-feature model, taking only 4.48 ms to predict all 260 samples (an average of 17 µs per sample), requiring at least 1.27 kB of RAM to store the neurons' weights and biases on the same low-cost ESP32-S board. On the other hand, electronic circuits capable of measuring the data required for this model (complex S_{11} and S_{21} at 546.8 MHz) will require additional components, which may increase the costs.

To visualize the decision boundaries learned by the 4-feature model, unfortunately there is no effective way. What can be done is discretize the 2D principal component space of **Figure 5.3** into 2835x2835 points, yielding 8,037,225 observations. Additionally, it is necessary to convert these 8,037,225 observations from the 2-PC space to the 4-feature space. This is accomplished by:

$$\boldsymbol{x}_{\mathbf{4FT}} = \boldsymbol{x}_{\mathbf{2PC}} \cdot \mathbf{M}^{\mathrm{T}} + \overline{\mathbf{X}}, \tag{5-1}$$

$$\mathbf{M} = \begin{bmatrix} 0.3698 & -0.4035 \\ 0.7398 & 0.6729 \\ -0.5464 & 0.6044 \\ -0.1322 & 0.1384 \end{bmatrix}, \tag{5-2}$$

$$\overline{\mathbf{X}} = [-0.8328 \quad -0.2498 \quad -0.0654 \quad 0.0372], \tag{5-3}$$

Figure 5.6 – Confusion matrix of the trained 4-feature model, obtained by averaging the confusion matrices of each test step of *k*-fold cross-validation. The areas highlighted with a blue diagonal pattern represent false-positives for adulteration, while the areas highlighted with a red squared pattern represent false-negatives.

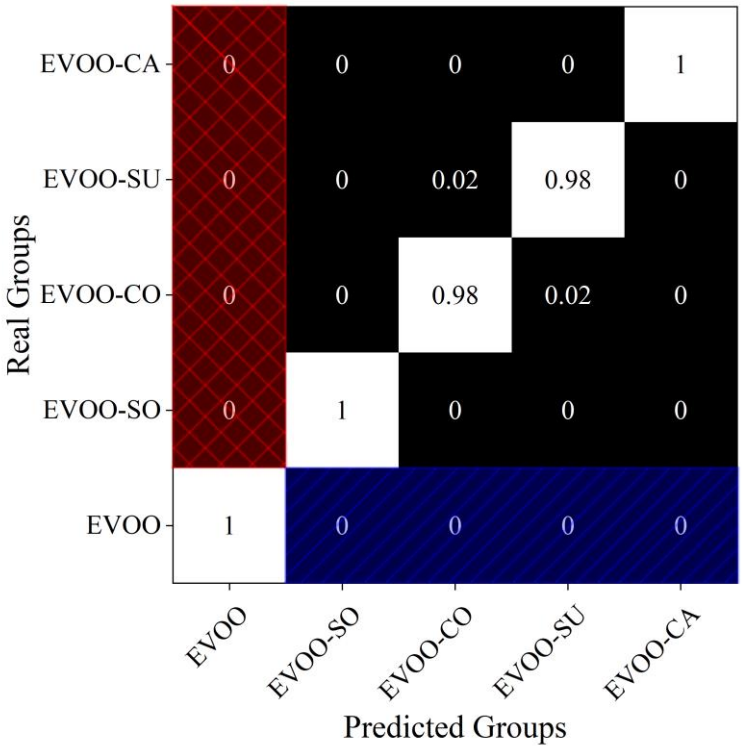

Source: Adapted from [78].

where $\boldsymbol{x_{4FT}}$ is the observation converted to the unnormalized 4-feature space, $\boldsymbol{x_{2PC}}$ is the observation in the 2-PC space, **M** is the transformation matrix carrying the proportion of the vectors in **Figure 5.3**, and $\overline{\mathbf{X}}$ is the vector containing the mean values of the 4-feature 240 observations. Matlab applies a normalization by the mean value to the data before actually executing the PCA, then the vector $\overline{\mathbf{X}}$ is included in **Equation 5-1** to execute the reverse process and denormalize the observation by the mean value. After applying **Equation 5-1** to every one of the 8,037,225 observations, they must be z-score normalized using **Table 4.3**. After normalization, the 4-feature model predicts all 8,037,225 instances, which results in **Figure 5.7**. As observed, this is not a very useful approach to visualize the learned decision boundaries for the 4-feature model, as the data of **Figure 5.7** don't match properly. This happens because **Equation 5-1** only consider the two first principal components and ignore the third and fourth PCs to reconstruct the four-dimensional data from the principal component space. Although the last two principal components have small relevance, they still impact the results of this approach to visualize the data. Despite the fact that we can't visualize properly what the 4-feature model

learned, we know from its confusion matrix in **Figure 5.6** that the model has an outstanding performance and generalization capability.

Figure 5.7 – Trial of visualizing the pattern learned by the 4-feature model by discretizing the 2 principal component space. Although the 2 PCs explain together 97.68%, the PC 3 and 4 (which were not considered) still plays an important role in explaining the data. This explains the error in trying to use PCA to also visualize the pattern learned.

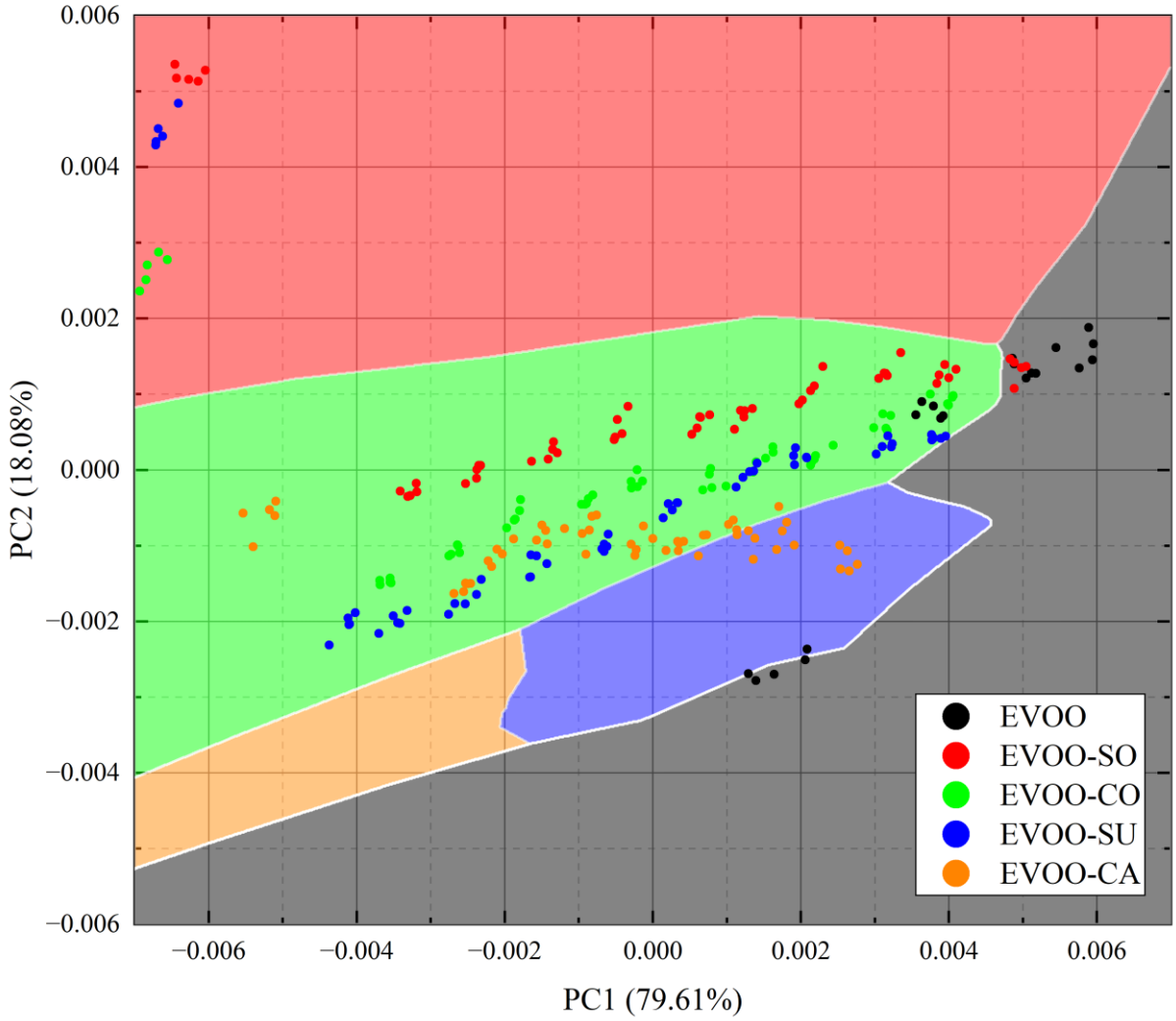

Source: Developed by the author.

5.3 PREDICTING THE ADULTERATION LEVELS

The last step of this work involves quantifying the adulteration through the linear relationship found between the adulteration level and the measured $|S_{21}|$. For this purpose, the PLSR algorithm is used on the data of each plot in **Figure 5.1** separately. Here, we assume $|S_{21}|$ as the only predictor variable x and the adulteration level as the only response variable y. By using the mean value between the five $|S_{21}|$ (in dB) replicates of each adulteration level, we construct a predictor vector X of shape 12x1, where the twelve rows refer to each adulteration level measured. Similarly, the response vector Y has a shape of 12x1. With the aid of the *plsregress* function in Matlab, we obtain a first-order polynomial that best explain the behavior of Y with the predictors in X, with the lowest root mean squared error (RMSE). This process is applied to each adulterant separately, which results in the following first-order polynomials to predict adulterations with soybean (A_{SO}), corn (A_{CO}), sunflower (A_{SU}), and canola (A_{CA}) oils:

$$A_{SO} = -140.0493 \cdot |S_{21}| - 3.1229 \times 10^3, \quad \text{5-4}$$

$$A_{CO} = -158.3388 \cdot |S_{21}| - 3.5283 \times 10^3, \quad \text{5-5}$$

$$A_{SU} = -139.8207 \cdot |S_{21}| - 3.1115 \times 10^3, \quad \text{5-6}$$

$$A_{CA} = -231.0639 \cdot |S_{21}| - 5.1452 \times 10^3, \quad \text{5-7}$$

where $|S_{21}|$ is measured in dB. The above equations already provide results in percentage (%) and are used to plot the dashed lines in **Figure 5.8**, illustrating the results of PLSR. As shown in the referred figure, the above equation set accurately describes the adulteration level (%) for all adulterants with very low RMSE (<5%), except for canola oil. Specifically for the canola oil, note that the error of the fitted curve increases as the adulteration level exceeds 50%. However, in the food industry, an adulteration exceeding 50% is impractical. Thus, we can further improve these results by considering, for all cases, an adulteration up to 50%. This is accomplished by removing the last row of both the predictor vector X and response vector Y, which refers to an adulteration level of 100%. Consequently, the fitted equation set for this new condition becomes:

$$A_{SO} = -148.6070 \cdot |S_{21}| - 3.3150 \times 10^3, \quad 5\text{-}8$$

$$A_{CO} = -165.5433 \cdot |S_{21}| - 3.6899 \times 10^3, \quad 5\text{-}9$$

$$A_{SU} = -162.1088 \cdot |S_{21}| - 3.6110 \times 10^3, \quad 5\text{-}10$$

$$A_{CA} = -190.1900 \cdot |S_{21}| - 4.2315 \times 10^3. \quad 5\text{-}11$$

Figure 5.8 – Fitted curves obtained from PLSR algorithm for the four tested adulterants. The solid lines indicate the mean value of the five replicates of each adulteration level, while the dashed lines represent the fitted curves. Additionally, the RMSE of each fitting is provided for performance comparison.

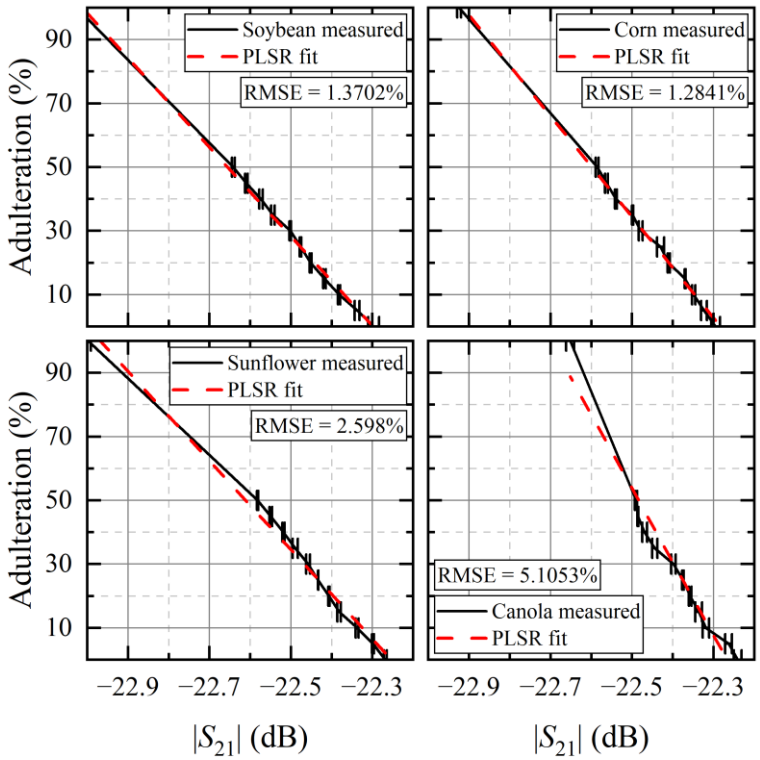

Source: [78].

We now use Equations **5-8** through **5-11** to generate the dashed lines in **Figure 5.9**, illustrating how well the curves fit the actual measurements. A significant improvement in the RMSE metric is observed, especially for the canola adulterant. By considering adulteration levels up to 50% instead of 100%, the RMSE for the fitted equation that predicts canola adulteration decreases from 5.1 % to 2.1 %. The results shown in **Figure 5.9** suggest that simple linear equations can accurately relate the adulteration level to the measurements performed by the proposed sensor, eliminating the need of more complex and sophisticated mathematical models to describe their relationship. Combining the results of **Figure 5.4**, **Figure 5.6** and **Figure 5.9** demonstrates that the approach presented in this paper with the proposed microwave

resonator-based sensor is suitable not only for identifying adulterants in EVOO but also for quantifying this adulteration. With this approach, it is possible to detect adulterations as low as 5% in EVOO using a low-cost and simple system.

Figure 5.9 – Results of PLSR improved, for all adulterants tested, by considering an adulteration level up to 50%. The dashed lines are the fitted curves, and the solid lines represent the mean value of the five measurements taken for each sample.

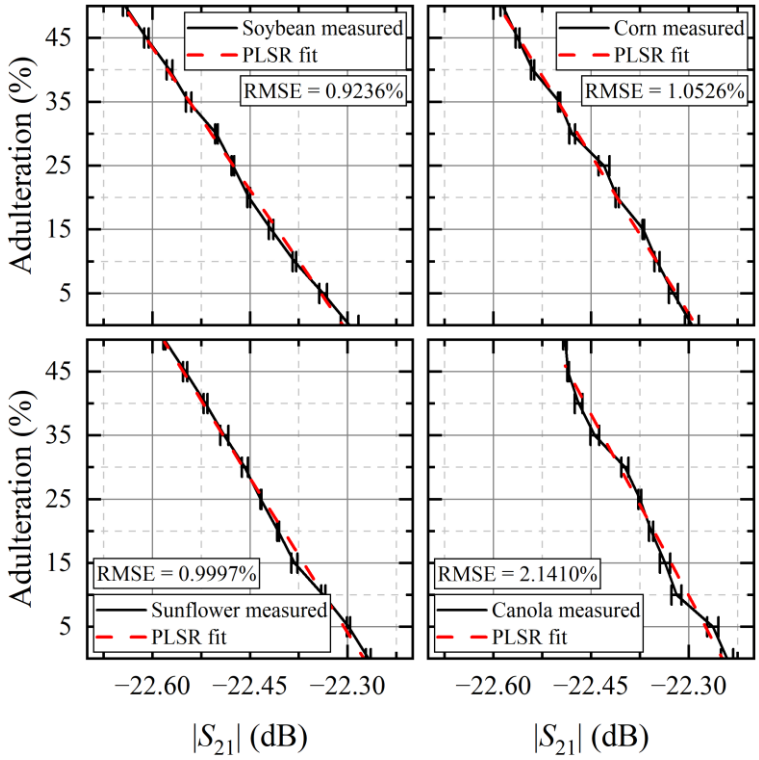

Source: [78].

The significance of this study lies in leveraging the disparity in complex permittivity between EVOO and adulterant oils. At the sensor's operational frequency of 546.8 MHz, EVOO exhibits the lowest relative permittivity among all investigated oils. Introducing any of the four adulterants into an EVOO sample increases the effective permittivity of the blend, thereby proportionally altering the scattering parameters of our sensor. While this study does not delve into the mixture of multiple adulterants in a single EVOO sample, it suggests that such mixtures could be discerned with minimal alterations in the output layer of the ANN classifiers. In this context, a binary classification approach to differentiate between adulterated and unadulterated samples becomes more practicable, reducing the output neurons from five to two. This feasibility arises from the fact that any combination of these adulterants invariably increases

the effective permittivity of the sample. However, detecting adulteration levels below 5%, particularly in cases dominated by canola oil, may not be assured. Furthermore, predicting the adulteration level of samples containing multiple adulterants, or estimating the quantity of each adulterant, might necessitate additional predictor variables. A single predictor variable, such as the $|S_{21}|$ utilized in this study, may not suffice to elucidate such complex relationships. Finally, by adapting the ANN models introduced in this study for binary classification, it becomes possible to investigate diverse types of adulterants beyond those explored herein, provided their complex permittivities at 546.8 MHz diverge from that of EVOO. However, it's noteworthy that reconfiguring the output architecture of the classifiers for binary classification mandates retraining from scratch, alongside considering distinct oil blends to enhance the models' generalizability.

5.4 SENSOR RESPONSE TO DIFFERENT BRANDS OF EVOO

In order to assess the influence of various brands of EVOO on the functionality of the proposed sensor, we measured the permittivity and sensor scattering parameters for four different brands of EVOO. Each EVOO brand, shown in **Figure 5.10**, has its dielectric parameters experimentally measured according to the methodology presented in the **Section 4.1**. The resulting relative permittivity and loss tangent values, along with fitted Cole-Cole models, are shown in **Figure 5.11(a)** and **(b)** for the real part of the relative permittivity, and **Figure 5.11(c)** and **(d)** for the loss tangent. The curves depicting the Cole-Cole are presented in **(b)** and **(d)**. The Cole-Cole model parameters for the four EVOO brands, their mean values, standard deviation, and fitting R^2 are listed in **Table 5.1**. Note that dielectric spectroscopy measurements result in very similar behavior for all EVOO brands, while they differ from the adulterants (see **Table 4.1**).

Figure 5.10 – Bottles of different tested EVOO brands.

Source: [78].

Figure 5.11 – (a) Experimentally measured relative permittivity and (c) loss tangent of four EVOOs from different brands. (b) Relative permittivity and (d) loss tangent obtained from the fitted Cole-Cole models. The similar permittivity and loss tangent profiles of the brands justify the sensor inability to distinguish between them.

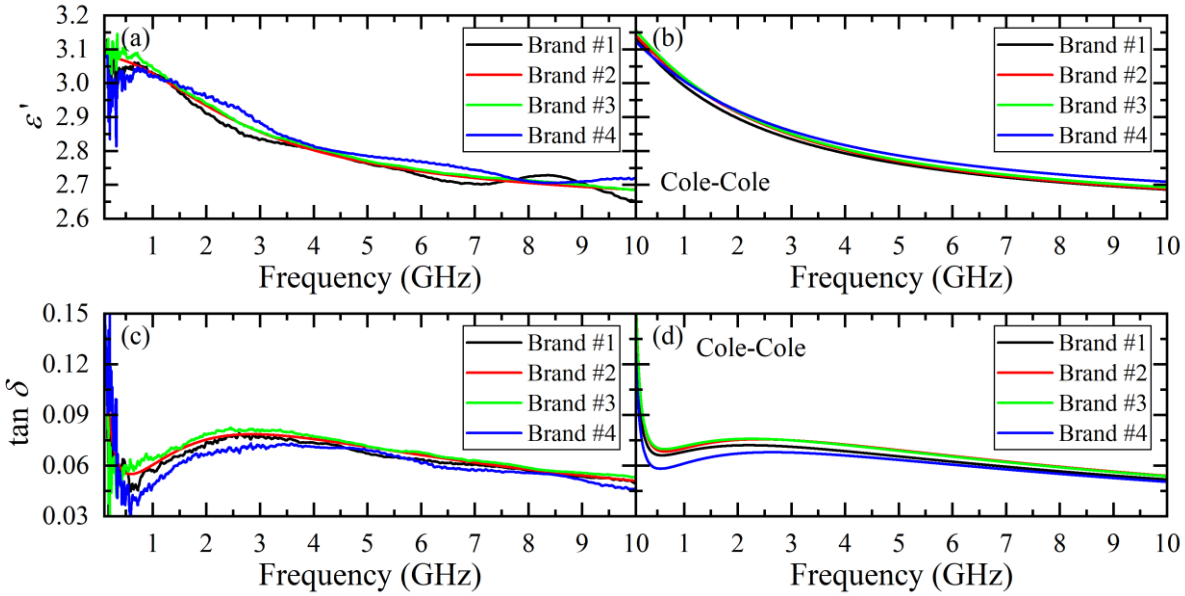

Source: [78].

To confirm that the sensor is not sensitive to EVOO brand changes, we conducted three separate measurements of the sensor scattering parameters for each EVOO brand. The average $|S_{11}|$ and $|S_{21}|$ curves, along with the error bars considering the three measurements, are depicted

in **Figure 5.12**. Note that the curves overlap, and the differences between each brand are smaller than the error bars, suggesting that any differences in the sensor response for the various EVOOs are beneath the adulterant limit of detection (LOD). Thus, the sensor is insensitive to the EVOO brand, while it can differentiate an adulterated EVOO sample from a pure EVOO sample. The EVOO brand used in the manuscript with multiple adulterants and adulteration levels was Brand #2.

Table 5.1 – Cole-Cole relaxation model fitting results for each EVOO brand.

	Brand #1	**Brand #2**	**Brand #3**	**Brand #4**	**Mean Values**	**Standard Deviation**
ε_∞	2.5707	2.5786	2.5807	2.6009	2.5827	0.0128
ε_s	3.1645	3.1615	3.1807	3.1416	3.1621	0.0160
τ (s)	6.57E-11	6.09E-11	6.39E-11	5.76E-11	6.20E-11	3.57E-12
α	0.2739	0.2377	0.2518	0.2455	0.2522	0.0156
σ_s **(S/m)**	2.16E-03	2.61E-03	2.56E-03	1.99E-03	2.33E-03	3.02E-04
R² real	0.9839	0.9965	0.9950	0.9770	-	-
R² imag	0.9348	0.9654	0.9290	0.9272	-	-

Source: [78].

Figure 5.12 – Sensor responses to four different brands of EVOO. The error bars overlap and no shift on the sensor resonance frequency is observed, signaling that all the four brands share a similar permittivity profile, and the proposed sensor will identify all four as EVOO.

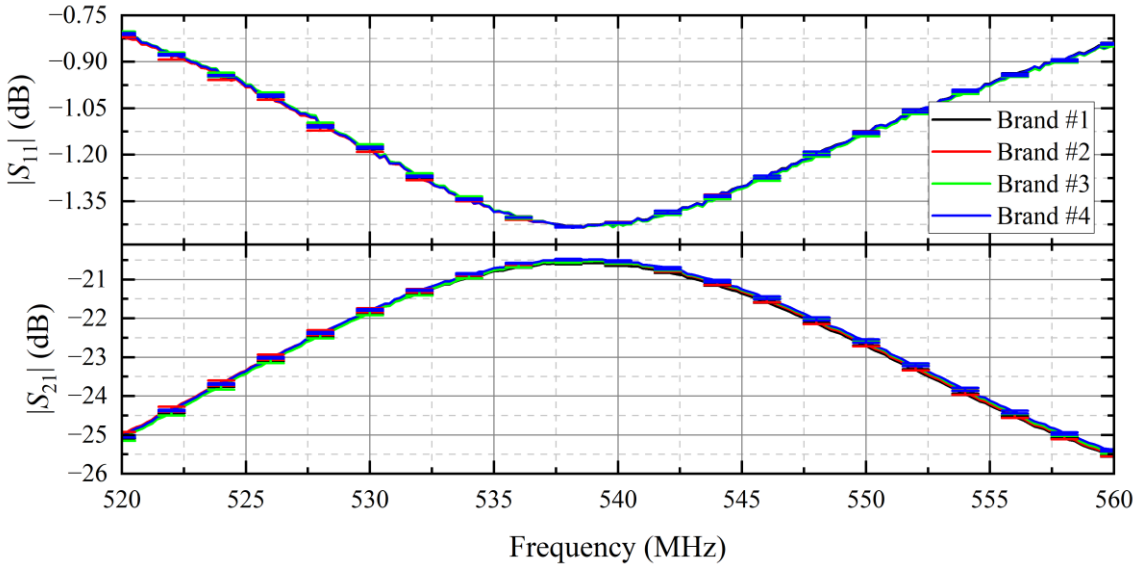

Source: [78].

6. CONCLUSIONS

In this work, we introduce a low-cost, simple, and robust system operating at a relatively low frequency (546.8 MHz), capable of identifying common adulterants in extra virgin olive oil and quantifying their levels. A microwave resonator-based sensor in the shape of a spiral is excited through transmission lines on an FR4 substrate with a ground plane to sense changes in the complex permittivity of oil samples inside a beaker. The complex scattering parameters S_{11} and S_{21} are extracted with the VNA, going through a Z-score normalization process and then input into a feedforward neural network classifier. We employ two neural network models to assess the impact of S_{11} data on classifying the adulterants. The 2-feature model, using only the complex S_{21}, achieves an overall accuracy of 91.4% in detecting the adulterant. In contrast, the 4-feature model, incorporating both S_{11} and S_{21} data, achieves an overall accuracy of 99.2%, thus completing the first step of the proposed approach: identifying the adulterant.

We also experimentally demonstrate the linear relationship between the measured $|S_{21}|$ in dB and the adulteration level of samples. Leveraging this linear behavior, we utilize the PLSR method to derive first-order polynomials that best fit the adulteration data. These polynomials can accurately explain the adulteration based on the quantity $|S_{21}|$, achieving a maximum RMSE of approximately 2%, thus concluding the second step of the work, namely, quantifying the adulterant. While other works make use of multiple spectral components to detect adulterations in EVOO, we experimentally demonstrate that single frequency component of the signals is totally capable of achieving the same results. Additionally, we suggest the use of the proposed ANN models as binary classifiers to account for other adulterants not studied in this work. Moreover, the reliability of both ANN classifiers is experimentally demonstrated by means of the confusion matrix of each model. The proposed methodology relies on dielectric spectroscopy characterization and employs machine learning techniques to detect adulteration in EVOO. The integration of these techniques offers a robust alternative to conventional methods, including chromatography and NMR. The low-cost, simplicity, and portability inherent in our approach enhance accessibility and practicality, making the entire system suitable for widespread use.

REFERENCES

[1] R. Sadigov, “Rapid Growth of the World Population and Its Socioeconomic Results,” *Scientific World Journal*, vol. 2022, 2022, doi: 10.1155/2022/8110229.

[2] I. G. J. Dawson and D. Zhang, “The 8 billion milestone: Risk perceptions of global population growth among UK and US residents,” *Risk Analysis*, vol. n/a, no. n/a, doi: https://doi.org/10.1111/risa.14272.

[3] D. Gu, K. Andreev, and M. E. Dupre, “Major trends in population growth around the world,” *China CDC Wkly*, vol. 3, no. 28, p. 604, 2021.

[4] E. B. Ntiamoah, A. A. Chandio, E. N. Yeboah, M. A. Twumasi, A. Siaw, and D. Li, “How do carbon emissions, economic growth, population growth, trade openness and employment influence food security? Recent evidence from the East Africa,” *Environmental Science and Pollution Research*, vol. 30, no. 18, pp. 51844–51860, Apr. 2023, doi: 10.1007/s11356-023-26031-3.

[5] J. Clapp, W. G. Moseley, B. Burlingame, and P. Termine, “Viewpoint: The case for a six-dimensional food security framework,” Jan. 01, 2022, *Elsevier Ltd*. doi: 10.1016/j.foodpol.2021.102164.

[6] S. Louie, Y. Shi, and M. Allman-Farinelli, “The effects of the COVID-19 pandemic on food security in Australia: A scoping review,” *Nutrition & Dietetics*, vol. 79, no. 1, pp. 28–47, 2022, doi: https://doi.org/10.1111/1747-0080.12720.

[7] FAO, IFAD, UNICEF, WFP, and WHO, “The State of Food Security and Nutrition in the World 2022. Repurposing food and agricultural policies to make healthy diets more affordable.,” Rome, 2022.

[8] R. Y. Zalia Powell Gerard Jefferies and C. Davis, “An Innovative Approach to Feeding the Hungry with Healthy Meals,” *Australian Social Work*, vol. 0, no. 0, pp. 1–9, 2024, doi: 10.1080/0312407X.2024.2303039.

[9] K. Pawlak and M. Kołodziejczak, “The Role of Agriculture in Ensuring Food Security in Developing Countries: Considerations in the Context of the Problem of Sustainable Food Production,” *Sustainability*, vol. 12, no. 13, 2020, doi: 10.3390/su12135488.

[10] P. Sundram and C. S. Brennan, “Triumphs, trials and tomorrow in food security: an ASEAN outlook,” *Int J Food Sci Technol*, vol. n/a, no. n/a, doi: https://doi.org/10.1111/ijfs.16899.

[11] N. and A. K. M. Telagam Nagarjuna and Kandasamy, “Review on Smart Farming and Smart Agriculture for Society: Post-pandemic Era,” in *Green Technological Innovation for Sustainable Smart Societies: Post Pandemic Era* , C. Chakraborty, Ed., Cham: Springer International Publishing, 2021, pp. 233–256. doi: 10.1007/978-3-030-73295-0_11.

[12] A. Sharma, A. Jain, P. Gupta, and V. Chowdary, “Machine Learning Applications for Precision Agriculture: A Comprehensive Review,” *IEEE Access*, vol. 9, pp. 4843–4873, 2021, doi: 10.1109/ACCESS.2020.3048415.

[13] Z. Gizaw, “Public health risks related to food safety issues in the food market: a systematic literature review,” *Environ Health Prev Med*, vol. 24, no. 1, p. 68, 2019, doi: 10.1186/s12199-019-0825-5.

[14] I. K. Karabagias, “Food authentication and adulteration control based on metrics data of foods and chemometrics,” *European Food Research and Technology*, 2024, doi: 10.1007/s00217-024-04477-0.

[15] J. Pages-Rebull, C. Pérez-Ràfols, N. Serrano, and J. M. Díaz-Cruz, “Analytical methods for cinnamon authentication,” *Trends Food Sci Technol*, vol. 146, p. 104388, 2024, doi: https://doi.org/10.1016/j.tifs.2024.104388.

[16] A. Castell, N. Arroyo-Manzanares, I. López-García, F. Zapata, and P. Viñas, “Authentication strategy for paprika analysis according to geographical origin and study of adulteration using near infrared spectroscopy and chemometric approaches,” *Food Control*, vol. 161, p. 110397, 2024, doi: https://doi.org/10.1016/j.foodcont.2024.110397.

[17] A. Negi, A. Pare, and R. Meenatchi, “Emerging techniques for adulterant authentication in spices and spice products,” *Food Control*, vol. 127, p. 108113, 2021, doi: https://doi.org/10.1016/j.foodcont.2021.108113.

[18] T. Tehrani, L. Pont, and F. Benavente, “Rapid detection and quantification of milk adulteration using MALDI-MS protein profiling and multivariate calibration,” *Journal of Food Composition and Analysis*, p. 106147, 2024, doi: https://doi.org/10.1016/j.jfca.2024.106147.

[19] Z. Ji *et al.*, “Identification of pasteurized mare milk and powder adulteration with bovine milk using quantitative proteomics and metabolomics approaches,” *Food Chem X*, p. 101265, 2024, doi: https://doi.org/10.1016/j.fochx.2024.101265.

[20] E. A. Zvereva, O. D. Hendrickson, B. B. Dzantiev, and A. V Zherdev, “Double lateral flow immunosensing of undeclared pork and chicken components of meat products,” *J Food Sci Technol*, 2024, doi: 10.1007/s13197-024-05944-y.

[21] Y.-C. Li *et al.*, “Comparative review and the recent progress in detection technologies of meat product adulteration,” *Compr Rev Food Sci Food Saf*, vol. 19, no. 4, pp. 2256–2296, 2020, doi: https://doi.org/10.1111/1541-4337.12579.

[22] E. Frankel, A. Bakhouche, J. Lozano-Sánchez, A. Segura-Carretero, and A. Fernández-Gutiérrez, “Literature Review on Production Process To Obtain Extra Virgin Olive Oil Enriched in Bioactive Compounds. Potential Use of Byproducts as Alternative Sources of Polyphenols,” *J Agric Food Chem*, vol. 61, no. 22, pp. 5179–5188, Jun. 2013, doi: 10.1021/jf400806z.

[23] D. Klisović, A. Novoselić, I. Lukić, and K. B. Bubola, “Extra virgin olive oil under simulated consumption conditions: Evaluation of quality, health, and flavour properties,” *Journal of Food Composition and Analysis*, vol. 110, Dec. 2022, doi: 10.1016/j.jfca.2022.104570.

[24] J. Lozano-Castellón *et al.*, “Extra virgin olive oil: A comprehensive review of efforts to ensure its authenticity, traceability, and safety,” *Compr Rev Food Sci Food Saf*, vol. 21, no. 3, pp. 2639–2664, 2022, doi: https://doi.org/10.1111/1541-4337.12949.

[25] IOC, “TRADE STANDARD APPLYING TO OLIVE OILS AND OLIVE POMACE OILS,” IOC COI/T.15/NC No 3/Rev. 19, 2022. [Online]. Available: http://www.internationaloliveoil.org/

[26] S. A. Ghreishi Rad, M. Jalili, F. Ansari, H. Rashidi Nodeh, and L. Rashidi, “Maturity impact on physicochemical composition and polyphenol properties of extra virgin olive oils obtained from Manzanilla, Arbequina, and Koroneiki varieties in Iran,” *Food Sci Nutr*, vol. 11, no. 9, pp. 5396–5408, 2023, doi: https://doi.org/10.1002/fsn3.3497.

[27] S. Tomé-Rodríguez, C. A. Ledesma-Escobar, H. Miho, C. Muñoz, and F. Priego-Capote, “Deciphering the influence of the cultivar on the phenolic content of virgin olive oil,”

Journal of Food Composition and Analysis, vol. 129, p. 106128, 2024, doi: https://doi.org/10.1016/j.jfca.2024.106128.

[28] C. Donat-Vargas, E. Lopez-Garcia, J. R. Banegas, M. Á. Martínez-González, F. Rodríguez-Artalejo, and P. Guallar-Castillón, "Only virgin type of olive oil consumption reduces the risk of mortality. Results from a Mediterranean population-based cohort," *Eur J Clin Nutr*, vol. 77, no. 2, pp. 226–234, 2023, doi: 10.1038/s41430-022-01221-3.

[29] M. Meenu, Q. Cai, and B. Xu, "A critical review on analytical techniques to detect adulteration of extra virgin olive oil," Dec. 2019, *Elsevier Ltd*. doi: 10.1016/j.tifs.2019.07.045.

[30] V. Maestrello, P. Solovyev, L. Bontempo, L. Mannina, and F. Camin, "Nuclear magnetic resonance spectroscopy in extra virgin olive oil authentication," *Compr Rev Food Sci Food Saf*, vol. 21, no. 5, pp. 4056–4075, 2022, doi: https://doi.org/10.1111/1541-4337.13005.

[31] Q. W. Yuandong Lin Ji Ma and D.-W. Sun, "Applications of machine learning techniques for enhancing nondestructive food quality and safety detection," *Crit Rev Food Sci Nutr*, vol. 63, no. 12, pp. 1649–1669, 2023, doi: 10.1080/10408398.2022.2131725.

[32] M. Khursheed, A. Ahmad, S. E. Noor, L. F. del Moral, and V. Martos Núñez, "Chromatographic Techniques for the Detection and Identification of Olive Oil Adulteration," Mar. 2024, *Universidad de Granada*. doi: 10.30827/Digibug.86578.

[33] IOC, "DETERMINATION OF THE CONTENT OF WAXES AND FATTY ACID ETHYL ESTERS BY CAPILLARY GAS CHROMATOGRAPHY," COI/T.20/Doc. no.28/Rev. 3/2022, Nov. 2022.

[34] IOC, "DETERMINATION OF PHENOLIC COMPOUNDS," COI/T.20/Doc. No 29/Rev.2/ 2022, Jun. 2022.

[35] R. Aparicio-Ruiz, I. Romero, D. L. García-González, C. Oliver-Pozo, and R. Aparicio, "Soft-deodorization of virgin olive oil: Study of the changes of quality and chemical composition," *Food Chem*, vol. 220, pp. 42–50, 2017, doi: https://doi.org/10.1016/j.foodchem.2016.09.176.

[36] M. de Person, S. Heron, K. Ben Arfa, M. Abderrabba, A. Tchapla, and F. Moussa, "Direct and rapid profiling of triacylglycerols in extra virgin olive oil using UHPLC-MS/MS,"

Food Control, vol. 158, p. 110266, 2024, doi: https://doi.org/10.1016/j.foodcont.2023.110266.

[37] H. S. Green *et al.*, "A rapid method for the detection of extra virgin olive oil adulteration using UHPLC-CAD profiling of triacylglycerols and PCA," *Food Control*, vol. 107, 2020, doi: 10.1016/j.foodcont.2019.106773.

[38] E. Hatzakis, "Nuclear Magnetic Resonance (NMR) Spectroscopy in Food Science: A Comprehensive Review," *Compr Rev Food Sci Food Saf*, vol. 18, no. 1, pp. 189–220, 2019, doi: https://doi.org/10.1111/1541-4337.12408.

[39] M. C. Ezeanaka, J. Nsor-Atindana, and M. Zhang, "Online Low-field Nuclear Magnetic Resonance (LF-NMR) and Magnetic Resonance Imaging (MRI) for Food Quality Optimization in Food Processing," *Food Bioproc Tech*, vol. 12, no. 9, pp. 1435–1451, 2019, doi: 10.1007/s11947-019-02296-w.

[40] R. Cao *et al.*, "Applications of nuclear magnetic resonance spectroscopy to the evaluation of complex food constituents," *Food Chem*, vol. 342, p. 128258, 2021, doi: https://doi.org/10.1016/j.foodchem.2020.128258.

[41] J. and R. M. and E. R. and F. S. and T. M. Zeindl Ricarda and Unterhauser, "Structural Characterization of Food Allergens by Nuclear Magnetic Resonance Spectroscopy," in *Food Allergens: Methods and Protocols* , B. Cabanillas, Ed., New York, NY: Springer US, 2024, pp. 159–173. doi: 10.1007/978-1-0716-3453-0_10.

[42] C. F. Balthazar *et al.*, "Nuclear magnetic resonance as an analytical tool for monitoring the quality and authenticity of dairy foods," *Trends Food Sci Technol*, vol. 108, pp. 84–91, 2021, doi: https://doi.org/10.1016/j.tifs.2020.12.011.

[43] C. Schmitt, T. Bastek, A. Stelzer, T. Schneider, M. Fischer, and T. Hackl, "Detection of Peanut Adulteration in Food Samples by Nuclear Magnetic Resonance Spectroscopy," *J Agric Food Chem*, vol. 68, no. 49, pp. 14364–14373, Dec. 2020, doi: 10.1021/acs.jafc.0c01999.

[44] D. Zou *et al.*, "Rapid detection of Salmonella in milk by biofunctionalised magnetic nanoparticle cluster sensor based on nuclear magnetic resonance," *Int Dairy J*, vol. 91, pp. 82–88, 2019, doi: https://doi.org/10.1016/j.idairyj.2018.11.011.

[45] A. O. Okaru *et al.*, “Validation of a Quantitative Proton Nuclear Magnetic Resonance Spectroscopic Screening Method for Coffee Quality and Authenticity (NMR Coffee Screener),” *Foods*, vol. 9, no. 1, 2020, doi: 10.3390/foods9010047.

[46] S. Wang *et al.*, “Rapid Detection of Adulteration in Extra Virgin Olive Oil by Low-Field Nuclear Magnetic Resonance Combined with Pattern Recognition,” 1973, doi: 10.1007/s12161-021-01973-x/Published.

[47] D. Ancora *et al.*, “Sensitivity of Proton NMR Relaxation and Proton NMR Diffusion Measurements to Olive Oil Adulterations with Vegetable Oils,” *J Agric Food Chem*, vol. 69, no. 41, pp. 12081–12088, Dec. 2021, doi: 10.1021/acs.jafc.1c00914.

[48] X. Wang, G. Wang, X. Hou, and S. Nie, “A Rapid Screening Approach for Authentication of Olive Oil and Classification of Binary Blends of Olive Oils Using Low-Field Nuclear Magnetic Resonance Spectra and Support Vector Machine,” *Food Anal Methods*, vol. 13, no. 10, pp. 1894–1905, Dec. 2020, doi: 10.1007/s12161-020-01799-z.

[49] C. R. Baiz *et al.*, “Vibrational Spectroscopic Map, Vibrational Spectroscopy, and Intermolecular Interaction,” *Chem Rev*, vol. 120, no. 15, pp. 7152–7218, Aug. 2020, doi: 10.1021/acs.chemrev.9b00813.

[50] A. M. Teixeira and C. Sousa, “A review on the application of vibrational spectroscopy to the chemistry of nuts,” *Food Chem*, vol. 277, pp. 713–724, 2019, doi: https://doi.org/10.1016/j.foodchem.2018.11.030.

[51] L. B. Leal, M. S. Nogueira, R. A. Canevari, and L. F. C. S. Carvalho, “Vibration spectroscopy and body biofluids: Literature review for clinical applications,” *Photodiagnosis Photodyn Ther*, vol. 24, pp. 237–244, 2018, doi: https://doi.org/10.1016/j.pdpdt.2018.09.008.

[52] S. J. Parikh, K. W. Goyne, A. J. Margenot, F. N. D. Mukome, and F. J. Calderón, “Chapter One - Soil Chemical Insights Provided through Vibrational Spectroscopy,” vol. 126, D. L. Sparks, Ed., in Advances in Agronomy, vol. 126. , Academic Press, 2014, pp. 1–148. doi: https://doi.org/10.1016/B978-0-12-800132-5.00001-8.

[53] H. J. Bakker and J. L. Skinner, “Vibrational Spectroscopy as a Probe of Structure and Dynamics in Liquid Water,” *Chem Rev*, vol. 110, no. 3, pp. 1498–1517, Mar. 2010, doi: 10.1021/cr9001879.

[54] S. Lohumi, S. Lee, H. Lee, and B.-K. Cho, “A review of vibrational spectroscopic techniques for the detection of food authenticity and adulteration,” *Trends Food Sci Technol*, vol. 46, no. 1, pp. 85–98, 2015, doi: https://doi.org/10.1016/j.tifs.2015.08.003.

[55] F. Kwofie, B. K. Lavine, J. Ottaway, and K. Booksh, “Differentiation of Edible Oils by Type Using Raman Spectroscopy and Pattern Recognition Methods,” *Appl Spectrosc*, vol. 74, no. 6, pp. 645–654, 2020, doi: 10.1177/0003702819888220.

[56] I. H. A. S. Barros, L. S. Paixão, M. H. C. Nascimento, V. Lacerda, P. R. Filgueiras, and W. Romão, “Use of portable Raman spectroscopy in the quality control of extra virgin olive oil and adulterated compound oils,” *Vib Spectrosc*, vol. 116, Dec. 2021, doi: 10.1016/j.vibspec.2021.103299.

[57] S. Duraipandian, J. C. Petersen, and M. Lassen, “Authenticity and concentration analysis of extra virgin olive oil using spontaneous raman spectroscopy and multivariate data analysis,” *Applied Sciences (Switzerland)*, vol. 9, no. 12, Dec. 2019, doi: 10.3390/app9122433.

[58] T. K. de Lima, M. Musso, and D. B. Menezes, “Using Raman spectroscopy and an exponential equation approach to detect adulteration of olive oil with rapeseed and corn oil,” *Food Chem*, vol. 333, Dec. 2020, doi: 10.1016/j.foodchem.2020.127454.

[59] F. T. Borghi *et al.*, “Quantification and classification of vegetable oils in extra virgin olive oil samples using a portable near-infrared spectrometer associated with chemometrics,” *Microchemical Journal*, vol. 159, Dec. 2020, doi: 10.1016/j.microc.2020.105544.

[60] X. Meng *et al.*, “Rapid detection of adulteration of olive oil with soybean oil combined with chemometrics by Fourier transform infrared, visible-near-infrared and excitation-emission matrix fluorescence spectroscopy: A comparative study,” *Food Chem*, vol. 405, p. 134828, Mar. 2023, doi: 10.1016/j.foodchem.2022.134828.

[61] H. Zaroual, E. M. El Hadrami, and R. Karoui, “Preliminary study on the potential application of Fourier-transform mid-infrared for the evaluation of overall quality and authenticity of Moroccan virgin olive oil,” *J Sci Food Agric*, vol. 101, no. 7, pp. 2901–2911, 2021, doi: https://doi.org/10.1002/jsfa.10922.

[62] C. Gertz, B. Matthäus, and I. Willenberg, “Detection of Soft-Deodorized Olive Oil and Refined Vegetable Oils in Virgin Olive Oil Using Near Infrared Spectroscopy and

Traditional Analytical Parameters," *European Journal of Lipid Science and Technology*, vol. 122, no. 6, p. 1900355, 2020, doi: https://doi.org/10.1002/ejlt.201900355.

[63] W. Sohng, Y. Park, D. Jang, K. Cha, Y. M. Jung, and H. Chung, "Incorporation of two-dimensional correlation analysis into discriminant analysis as a potential tool for improving discrimination accuracy: Near-infrared spectroscopic discrimination of adulterated olive oils," *Talanta*, vol. 212, p. 120748, May 2020, doi: 10.1016/j.talanta.2020.120748.

[64] S. Rubalya Valantina, "Measurement of dielectric constant: A recent trend in quality analysis of vegetable oil - A review," *Trends Food Sci Technol*, vol. 113, pp. 1–11, 2021, doi: https://doi.org/10.1016/j.tifs.2021.04.026.

[65] Z. Li, A. Haigh, P. Wang, C. Soutis, and A. Gibson, "Dielectric spectroscopy of Baijiu over 2–20 GHz using an open-ended coaxial probe," *J Food Sci*, vol. 86, no. 6, pp. 2513–2524, 2021, doi: https://doi.org/10.1111/1750-3841.15738.

[66] M. Soltani Firouz, M. Rashvand, and M. Omid, "Rapid identification and quantification of sesame oils adulteration using low frequency dielectric spectroscopy combined with chemometrics," *LWT*, vol. 140, p. 110736, 2021, doi: https://doi.org/10.1016/j.lwt.2020.110736.

[67] M. Soltani Firouz, M. Omid, M. Babaei, and M. Rashvand, "Dielectric spectroscopy coupled with artificial neural network for classification and quantification of sesame oil adulteration," *Information Processing in Agriculture*, vol. 9, no. 2, pp. 233–242, 2022, doi: https://doi.org/10.1016/j.inpa.2021.05.001.

[68] D. Fang, K. Yang, J. Zhu, C. An, W. Guo, and X. Zhu, "Hydration dominates dielectric spectroscopy-based high accuracy quantification of lactose content in cow's milk," *J Sci Food Agric*, vol. 103, no. 12, pp. 5873–5882, 2023, doi: https://doi.org/10.1002/jsfa.12658.

[69] C. E. Meng *et al.*, "Mineral composition, crystallinity and dielectric evaluation of Bamboo Salt, Himalaya Salt, and Ba'kelalan salt content," *Heliyon*, vol. 10, no. 1, p. e23847, 2024, doi: https://doi.org/10.1016/j.heliyon.2023.e23847.

[70] M. R. Islam *et al.*, "Metamaterial sensor based on rectangular enclosed adjacent triple circle split ring resonator with good quality factor for microwave sensing application," *Sci Rep*, vol. 12, no. 1, Dec. 2022, doi: 10.1038/s41598-022-10729-4.

[71] R. Peñaloza-Delgado, J. L. Olvera-Cervantes, M. E. Sosa-Morales, T. K. Kataria, and A. Corona-Chávez, “Dielectric characterization of vegetable oils during a heating cycle,” *J Food Sci Technol*, vol. 58, no. 4, pp. 1480–1487, Dec. 2021, doi: 10.1007/s13197-020-04660-7.

[72] M. H. Bhatti, M. A. Jabbar, M. A. Khan, and Y. Massoud, “Low-Cost Microwave Sensor for Characterization and Adulteration Detection in Edible Oil,” *Applied Sciences (Switzerland)*, vol. 12, no. 17, Sep. 2022, doi: 10.3390/app12178665.

[73] N. K. Tiwari, S. P. Singh, and M. J. Akhtar, “Novel Improved sensitivity planar microwave probe for adulteration detection in edible oils,” *IEEE Microwave and Wireless Components Letters*, vol. 29, no. 2, pp. 164–166, Dec. 2019, doi: 10.1109/LMWC.2018.2886062.

[74] M. S. ur Rahman, M. A. Abou-Khousa, and K. M. Donnell, “In-Situ permittivity measurement of liquids using immersible planar resonator,” *Measurement (Lond)*, vol. 198, Dec. 2022, doi: 10.1016/j.measurement.2022.111447.

[75] E. L. Chuma and T. Rasmussen, “Metamaterial-Based Sensor Integrating Microwave Dielectric and Near-Infrared Spectroscopy Techniques for Substance Evaluation,” *IEEE Sens J*, vol. 22, no. 20, pp. 19308–19314, Dec. 2022, doi: 10.1109/JSEN.2022.3202708.

[76] A. C. Patil, A. F. la Villa, A. K. Mugilvannan, and U. Elejalde, “Electrochemical investigation of edible oils: Experimentation, electrical signatures, and a supervised learning–case study of adulterated peanut oils,” *Food Chem*, vol. 402, Dec. 2023, doi: 10.1016/j.foodchem.2022.134143.

[77] H. K. S. V. Mohan, P. P. Aung, C. F. Ng, Z. Z. Wong, and A. A. Malcolm, “Rapid Non-Invasive Capacitive Assessment of Extra Virgin Olive Oil Authenticity,” *Electronics (Switzerland)*, vol. 12, no. 2, Dec. 2023, doi: 10.3390/electronics12020359.

[78] J. C. P. Alarcon, M. I. O. Souza, V. M. Pepino, and B.-H. V. Borges, “Identification and Quantification of Common Adulterants in Extra Virgin Olive Oil Using Microwave Dielectric Spectroscopy Aided by Artificial Neural Network Classifiers,” *IEEE Sensors*, Aug. 2024, doi: 10.1109/JSEN.2024.3448221.

[79] David M. Pozar, *Microwave Engineering*, 4th ed. John Wiley & Sons, Inc., 2012.

[80] J. Muñoz-Enano, P. Vélez, M. Gil, and F. Martín, “Planar Microwave Resonant Sensors: A Review and Recent Developments,” *Applied Sciences*, vol. 10, no. 7, 2020, doi: 10.3390/app10072615.

[81] ANSYS, “HFSS: High Frequency Structure Simulator,” Jan. 2024, *Canonsburg, PA, USA. [Online]. Available: https://www.ansys.com/*.

[82] M. Abdolrazzaghi, V. Nayyeri, and F. Martin, “Techniques to Improve the Performance of Planar Microwave Sensors: A Review and Recent Developments,” *Sensors*, vol. 22, no. 18, 2022, doi: 10.3390/s22186946.

[83] M. Durán-Sindreu, J. Naqui, F. Paredes, J. Bonache, and F. Martín, “Electrically Small Resonators for Planar Metamaterial, Microwave Circuit and Antenna Design: A Comparative Analysis,” *Applied Sciences*, vol. 2, no. 2, pp. 375–395, 2012, doi: 10.3390/app2020375.

[84] R. Marques, F. Mesa, J. Martel, and F. Medina, “Comparative analysis of edge- and broadside- coupled split ring resonators for metamaterial design - theory and experiments,” *IEEE Trans Antennas Propag*, vol. 51, no. 10, pp. 2572–2581, 2003, doi: 10.1109/TAP.2003.817562.

[85] Y. Zhu, J. Wang, J. Hong, J.-X. Chen, and W. Wu, “Two- and Three-Way Filtering Power Dividers With Harmonic Suppression Using Triangle Patch Resonator,” *IEEE Transactions on Circuits and Systems I: Regular Papers*, vol. 68, no. 12, pp. 5007–5017, 2021, doi: 10.1109/TCSI.2021.3112748.

[86] Q. Zhang, G. Zhang, Z. Liu, W. Chen, and W. Tang, “Dual-Band Filtering Power Divider Based on a Single Circular Patch Resonator With Improved Bandwidths and Good Isolation,” *IEEE Transactions on Circuits and Systems II: Express Briefs*, vol. 68, no. 11, pp. 3411–3415, 2021, doi: 10.1109/TCSII.2021.3081266.

[87] Q. Liu, D. Zhou, X. Wang, M. Tang, D. Zhang, and Y. Zhang, “High-Selective Bandpass Filters Based on New Dual-Mode Rectangular Strip Patch Resonators,” *IEEE Microwave and Wireless Components Letters*, vol. 31, no. 10, pp. 1123–1126, 2021, doi: 10.1109/LMWC.2021.3106128.

[88] R. A. Alahnomi *et al.*, “Review of Recent Microwave Planar Resonator-Based Sensors: Techniques of Complex Permittivity Extraction, Applications, Open Challenges and Future Research Directions,” *Sensors*, vol. 21, no. 7, 2021, doi: 10.3390/s21072267.

[89] W. H. H. Woodward, “Broadband Dielectric Spectroscopy—A Practical Guide,” in *Broadband Dielectric Spectroscopy: A Modern Analytical Technique*, vol. 1375, in ACS Symposium Series, vol. 1375. , American Chemical Society, 2021, ch. 1, pp. 3–59. doi: doi:10.1021/bk-2021-1375.ch001.

[90] P. K. Varshney and M. J. Akhtar, “Permittivity Estimation of Dielectric Substrate Materials via Enhanced SIW Sensor,” *IEEE Sens J*, vol. 21, no. 10, pp. 12104–12112, 2021, doi: 10.1109/JSEN.2021.3064923.

[91] A. Raveendran and S. Raman, “Complex Permittivity Extraction of Planar Dielectrics Using a Noninvasive Microwave Transmission Line Resonant Technique,” *IEEE Trans Instrum Meas*, vol. 70, pp. 1–8, 2021, doi: 10.1109/TIM.2021.3070614.

[92] S. Kr. Singh, T. Sharan, and A. Kr. Singh, “A comparative performance analysis of various shapes and substrate materials loaded coplanar waveguide-fed antennas,” *Mater Today Proc*, vol. 34, pp. 643–648, 2021, doi: https://doi.org/10.1016/j.matpr.2020.03.133.

[93] L. Wang, G. Xia, and H. Yu, “A Method to Determine Dielectric Model Parameters for Broadband Permittivity Characterization of Thin Film Substrates,” *IEEE Trans Electromagn Compat*, vol. 63, no. 1, pp. 229–236, 2021, doi: 10.1109/TEMC.2020.2989227.

[94] Constantine A. Balanis, *Advanced Engineering Electromagnetics*, 2nd ed. John Wiley & Sons, Inc, 2012.

[95] H. R. Kaupp, “Characteristics of Microstrip Transmission Lines,” *IEEE Transactions on Electronic Computers*, vol. EC-16, no. 2, pp. 185–193, 1967, doi: 10.1109/PGEC.1967.264815.

[96] X. Zhang, W. Y. Cui, Y. Lei, X. Zheng, J. Zhang, and T. J. Cui, “Spoof Localized Surface Plasmons for Sensing Applications,” *Adv Mater Technol*, vol. 6, no. 4, p. 2000863, 2021, doi: https://doi.org/10.1002/admt.202000863.

[97] A. Ebrahimi, J. Scott, and K. Ghorbani, “Ultrahigh-Sensitivity Microwave Sensor for Microfluidic Complex Permittivity Measurement,” *IEEE Trans Microw Theory Tech*, vol. 67, no. 10, pp. 4269–4277, 2019, doi: 10.1109/TMTT.2019.2932737.

[98] M. Abdolrazzaghi and M. Daneshmand, “A Phase-Noise Reduced Microwave Oscillator Sensor With Enhanced Limit of Detection Using Active Filter,” *IEEE Microwave and Wireless Components Letters*, vol. 28, no. 9, pp. 837–839, 2018, doi: 10.1109/LMWC.2018.2850283.

[99] N. Hosseini, M. Baghelani, and M. Daneshmand, “Selective Volume Fraction Sensing Using Resonant- Based Microwave Sensor and its Harmonics,” *IEEE Trans Microw Theory Tech*, vol. 68, no. 9, pp. 3958–3968, 2020, doi: 10.1109/TMTT.2020.2990139.

[100] N. Chudpooti *et al.*, “In-Situ Self-Aligned NaCl-Solution Fluidic-Integrated Microwave Sensors for Industrial and Biomedical Applications,” *IEEE Access*, vol. 8, pp. 188897–188907, 2020, doi: 10.1109/ACCESS.2020.3031864.

[101] A. K. Jha, A. Lamecki, M. Mrozowski, and M. Bozzi, “A Microwave Sensor With Operating Band Selection to Detect Rotation and Proximity in the Rapid Prototyping Industry,” *IEEE Transactions on Industrial Electronics*, vol. 68, no. 1, pp. 683–693, 2021, doi: 10.1109/TIE.2020.2965464.

[102] A. Pors, E. Moreno, L. Martin-Moreno, J. B. Pendry, and F. J. Garcia-Vidal, “Localized Spoof Plasmons Arise while Texturing Closed Surfaces,” *Phys Rev Lett*, vol. 108, no. 22, p. 223905, May 2012, doi: 10.1103/PhysRevLett.108.223905.

[103] X. Shen and T. J. Cui, “Ultrathin plasmonic metamaterial for spoof localized surface plasmons,” *Laser Photon Rev*, vol. 8, no. 1, pp. 137–145, 2014, doi: https://doi.org/10.1002/lpor.201300144.

[104] P. A. Huidobro *et al.*, “Magnetic Localized Surface Plasmons,” *Phys Rev X*, vol. 4, no. 2, p. 21003, Apr. 2014, doi: 10.1103/PhysRevX.4.021003.

[105] J. Wang, J. Zhang, H. Gao, X. Fu, D. Bao, and T. J. Cui, “Mixed-Resolution High-Q Sensor Based on Hybridized Spoof Localized Surface Plasmons,” *Front Phys*, vol. 10, 2022, doi: 10.3389/fphy.2022.850186.

[106] Y. Kim, A. Salim, and S. Lim, “Millimeter-Wave-Based Spoof Localized Surface Plasmonic Resonator for Sensing Glucose Concentration,” *Biosensors (Basel)*, vol. 11, no. 10, 2021, doi: 10.3390/bios11100358.

[107] J. Cai, Y. J. Zhou, Y. Zhang, and Q. Y. Li, “Gain-assisted ultra-high-Q spoof plasmonic resonator for the sensing of polar liquids,” *Opt. Express*, vol. 26, no. 19, pp. 25460–25470, Sep. 2018, doi: 10.1364/OE.26.025460.

[108] Z. Gao, L. Wu, F. Gao, Y. Luo, and B. Zhang, “Spoof Plasmonics: From Metamaterial Concept to Topological Description,” *Advanced Materials*, vol. 30, no. 31, p. 1706683, 2018, doi: https://doi.org/10.1002/adma.201706683.

[109] Ivan Nunes da Silva, Danilo Hernane Spatti, and Rogério Andrade Flauzino, *Redes Neurais Artificiais Para Engenharia e Ciências Aplicadas*, 2nd ed. São Paulo, 2016.

[110] Marvin Minsky and Seymour Papert, *Perceptrons: An Introduction to Computational Geometry*, 1st ed. 1969.

[111] Rafael C. Gonzalez and Richard E. Woods, *Digital Image Processing*, 4th ed., vol. 1. Pearson, 2017.

[112] Y. Li, Y. Xiong, and S. Min, “Data fusion strategy in quantitative analysis of spectroscopy relevant to olive oil adulteration,” *Vib Spectrosc*, vol. 101, pp. 20–27, Dec. 2019, doi: 10.1016/j.vibspec.2018.12.009.

[113] F. Chollet and others, “Keras,” 2015.

[114] A.-B. Al-Ghamdi, S. Kamel, and M. Khayyat, “Evaluation of Artificial Neural Networks Performance Using Various Normalization Methods for Water Demand Forecasting,” in *2021 National Computing Colleges Conference (NCCC)*, 2021, pp. 1–6. doi: 10.1109/NCCC49330.2021.9428856.

[115] R. Moradi, R. Berangi, and B. Minaei, “A survey of regularization strategies for deep models,” *Artif Intell Rev*, vol. 53, no. 6, pp. 3947–3986, 2020, doi: 10.1007/s10462-019-09784-7.

[116] T.-T. Wong and P.-Y. Yeh, “Reliable Accuracy Estimates from k-Fold Cross Validation,” *IEEE Trans Knowl Data Eng*, vol. 32, no. 8, pp. 1586–1594, 2020, doi: 10.1109/TKDE.2019.2912815.

[117] J. S. Bobowski and T. Johnson, “PERMITTIVITY MEASUREMENTS OF BIOLOGICAL SAMPLES BY AN OPEN-ENDED COAXIAL LINE,” 2012.

[118] R. Dima, G. Buonanno, S. Costanzo, and R. Solimene, “Robustness for the Starting Point of Two Iterative Methods for Fitting Debye or Cole–Cole Models to a Dielectric Permittivity Spectrum,” *Applied Sciences*, vol. 12, no. 11, 2022, doi: 10.3390/app12115698.

[119] The MathWorks Inc. (2022), “MATLAB version: 9.13.0 (R2022b),” *[Online]. Available: https://www.mathworks.com*.

A. MICROWAVE TECHNIQUES AND THEORIES

A.1 SCATTERING PARAMETERS OF MICROWAVE NETWORKS

In practice, there is a problem when trying to measure voltages and currents at microwave frequencies because direct measurements involve the magnitude and phase of a wave traveling in a given direction. A more practical representation deals only with incident, reflected and transmitted waves and is given by the scattering matrix. The scattering matrix relates the voltage waves incident on the ports to the voltage waves reflected from the ports [79]. In **Figure A.1**, a 2-port microwave network is depicted with the incident and reflected voltages V_1^+ and V_1^- on port 1, and the incident and reflected voltages V_2^+ and V_2^- on port 2.

Figure A.1 – Two-port microwave network model with incident and reflected voltages V_1^+ and V_1^- on port 1, and incident and reflected voltages V_2^+ and V_2^- on port 2.

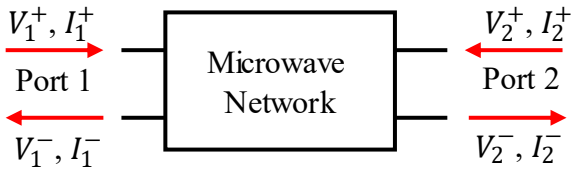

Source: Adapted from [79].

For the 2-port microwave network of **Figure A.1**, the scattering matrix is defined as follows:

$$[V^-] = [S][V^+],$$
$$\begin{bmatrix} V_1^- \\ V_2^- \end{bmatrix} = \begin{bmatrix} S_{11} & S_{12} \\ S_{21} & S_{22} \end{bmatrix} \begin{bmatrix} V_1^+ \\ V_2^+ \end{bmatrix}, \quad \text{A-1}$$

where the scattering parameter S_{ij} is defined as:

$$S_{ij} = \left.\frac{V_i^-}{V_j^+}\right|_{V_k^+=0 \text{ for } k\neq j}. \quad \text{A-2}$$

The scattering parameter S_{ij} is obtained by driving the port j with an incident voltage V_j^+ and measuring the reflected wave amplitude V_i^- on port i, with all other ports terminated in matched loads to avoid reflections on these ports. Therefore, S_{ii} is the reflection coefficient seen when looking into port i with all other ports terminated in matched loads, and S_{ij} is the transmission coefficient from port j to port i when all other ports are terminated in matched loads. Simple microwave networks will have a single port or two ports depending on the application. Since the scattering parameters carry information of both magnitude and phase, they are complex quantities. The VNA is a two-channel (or four-channel) microwave receiver designed to sample magnitude and phase of transmitted and reflected waves from the network, being capable of measuring each S parameter and building the scattering matrix. Parameters that can be derived from the S-parameters, such as standing wave ratio, return loss, group delay and impedance, can also be measured by the VNA [79].

A.2 CAVITY PERTURBATION THEORY

Consider the arbitrary closed surface S of **Figure A.2**. The surface encloses a volume v, where a resonant cavity is positioned. In (a), the environment around the cavity has a permittivity of ε and a permeability of μ, the angular resonance frequency of the cavity under these conditions is ω_0 and the fields are $\mathbf{E_0}$ and $\mathbf{H_0}$. In (b), the environment suffers a material perturbation causing increments of $\Delta\varepsilon$ in the permittivity and $\Delta\mu$ in the permeability, thus changing the resonance angular frequency of the cavity to ω and the fields to **E** and **H**. For both cases, the Maxwell's curl equations in the phasor form can be written as [79]

$$\nabla \times \mathbf{E_0} = -j\omega_0\mu\mathbf{H_0}, \quad \text{A-3}$$

$$\nabla \times \mathbf{H_0} = j\omega_0 \varepsilon \mathbf{E_0}, \quad \text{A-4}$$

$$\nabla \times \mathbf{E} = -j\omega(\mu + \Delta\mu)\mathbf{H}, \quad \text{A-5}$$

$$\nabla \times \mathbf{H} = j\omega(\varepsilon + \Delta\varepsilon)\mathbf{E}. \quad \text{A-6}$$

Figure A.2 – Arbitrary surface S enclosing a volume v where a resonant cavity is positioned. (a) the material has permittivity ε and permeability μ, the fields in the proximity of the cavity is $\mathbf{E_0}$ and $\mathbf{H_0}$. (b) a material perturbation on the environment around the cavity causes an increment of $\Delta\varepsilon$ in the permittivity and $\Delta\mu$ in the permeability, changing the fields to **E** and **H**.

Source: Adapted from [79].

Multiplying the conjugate of Equation A-3 by H and multiplying Equation A-6 by ${E_0}^*$, we obtain

$$\mathrm{H} \cdot \nabla \times \mathrm{E_0}^* = \mathrm{j}\omega_0 \mu \mathrm{H} \cdot \mathrm{H_0}^*, \quad \text{A-7}$$

$${E_0}^* \cdot \nabla \times H = j\omega(\varepsilon + \Delta\varepsilon){E_0}^* \cdot E. \quad \text{A-8}$$

Subtracting Equations A-7 and A-8, and applying the vector identity $\nabla \cdot (A \times B) = B \cdot \nabla \times A - A \cdot \nabla \times B$ will result in

$$\nabla \cdot ({E_0}^* \times H) = j\omega_0 \mu H \cdot {H_0}^* - j\omega(\varepsilon + \Delta\varepsilon){E_0}^* \cdot E. \quad \text{A-9}$$

Similarly, multiplying the conjugate of Equation A-4 by E, and multiplying Equation A-5 by ${H_0}^*$, yields

$$E \cdot \nabla \times H_0{}^* = -j\omega_0 \varepsilon E_0{}^* \cdot E, \qquad \text{A-10}$$

$$H_0{}^* \cdot \nabla \times E = -j\omega(\mu + \Delta\mu) H_0{}^* \cdot H. \qquad \text{A-11}$$

Subtracting Equations A-10 and A-11, and applying the same vector identity applied above results in

$$\nabla \cdot (E \times H_0{}^*) = -j\omega(\mu + \Delta\mu) H_0{}^* \cdot H + j\omega_0 \varepsilon E_0{}^* \cdot E. \qquad \text{A-12}$$

Adding Equations A-9 and A-12, integrating over the volume v and using the divergence theorem to make it an integral over the surface S

$$\int_v \nabla \cdot (E_0{}^* \times H + E \times H_0{}^*) dv = \oint_S \nabla \cdot (E_0{}^* \times H + E \times H_0{}^*) ds = 0, \qquad \text{A-13}$$

where the result equals zero because on the surface S, $\hat{\boldsymbol{n}} \times E = 0$, which makes the surface integral zero. Expanding the left side of the Equation A-13 results in

$$j \int_v \{[\omega_0 \varepsilon - \omega(\varepsilon + \Delta\varepsilon)] E_0{}^* \cdot E + [\omega_0 \mu - \omega(\mu + \Delta\mu)] H_0{}^* \cdot H\} \, dv = 0. \qquad \text{A-14}$$

Finally, rewriting Equation A-14 yields

$$\frac{\omega - \omega_0}{\omega} = \frac{-\int_v (\Delta\varepsilon E \cdot E_0{}^* + \Delta\mu H \cdot H_0{}^*) \, dv}{\int_v (\varepsilon E \cdot E_0{}^* + \mu H \cdot H_0{}^*) \, dv}. \qquad \text{A-15}$$

The fields in the perturbed cavity are usually not known, therefore Equation A-15 is not very suitable to use. However, if the material perturbation is considered to be minimal ($\Delta\varepsilon$ and $\Delta\mu$ are small), then the perturbed fields E and H can be approximated to those of the unperturbed

cavity, i.e., E_0 and H_0. Furthermore the ω in the denominator of Equation A-15 can be approximated to ω_0. Making these changes and rewriting the equation results in

$$\Delta\omega \approx \omega_0 \frac{-\int_v (\Delta\varepsilon|\mathbf{E_0}|^2 + \Delta\mu|\mathbf{H_0}|^2)\, dv}{\int_v (\varepsilon|\mathbf{E_0}|^2 + \mu|\mathbf{H_0}|^2)\, dv}. \qquad \text{A-16}$$

Now, Equation A-16 is more meaningful and suggests that an increase in ε or μ at any point in the cavity will cause the resonance angular frequency to decrease. This result is coherent with the experimental results obtained in this work. Moreover, the equation above is also related to the energy stored in a cavity, which means that a decrease in the resonance frequency can be related to an increase in the stored energy.

B. PERMISSION FOR REUSE OF PUBLISHED MATERIAL

IEEE Requesting permission to reuse content from an IEEE publication

Identification and Quantification of Common Adulterants in Extra Virgin Olive Oil Using Microwave Dielectric Spectroscopy Aided by Feedforward Neural Networks

Author: Júlio C.P. Alarcon
Publication: IEEE Sensors Journal
Publisher: IEEE
Date: 28 August 2024

Thesis / Dissertation Reuse

The IEEE does not require individuals working on a thesis to obtain a formal reuse license, however, you may print out this statement to be used as a permission grant:

Requirements to be followed when using any portion (e.g., figure, graph, table, or textual material) of an IEEE copyrighted paper in a thesis:

1) In the case of textual material (e.g., using short quotes or referring to the work within these papers) users must give full credit to the original source (author, paper, publication) followed by the IEEE copyright line © 2011 IEEE.
2) In the case of illustrations or tabular material, we require that the copyright line © [Year of original publication] IEEE appear prominently with each reprinted figure and/or table.
3) If a substantial portion of the original paper is to be used, and if you are not the senior author, also obtain the senior author's approval.

Requirements to be followed when using an entire IEEE copyrighted paper in a thesis:

1) The following IEEE copyright/ credit notice should be placed prominently in the references: © [year of original publication] IEEE. Reprinted, with permission, from [author names, paper title, IEEE publication title, and month/year of publication]
2) Only the accepted version of an IEEE copyrighted paper can be used when posting the paper or your thesis on-line.
3) In placing the thesis on the author's university website, please display the following message in a prominent place on the website: In reference to IEEE copyrighted material which is used with permission in this thesis, the IEEE does not endorse any of [university/educational entity's name goes here]'s products or services. Internal or personal use of this material is permitted. If interested in reprinting/republishing IEEE copyrighted material for advertising or promotional purposes or for creating new collective works for resale or redistribution, please go to http://www.ieee.org/publications_standards/publications/rights/rights_link.html to learn how to obtain a License from RightsLink.

If applicable, University Microfilms and/or ProQuest Library, or the Archives of Canada may supply single copies of the dissertation.

BACK CLOSE WINDOW


EESC • USP